







## ACKNOWLEDGEMENTS

First and foremost, I would like to express my sincere gratitude to my advisor, Dr. Rob Walker, for all of his support and guidance throughout my graduate career. You have continually provided me with invaluable opportunities for professional development and enlightening discussions about current and future research. Thank you Walker research group members, both past and present, for the wonderful scientific discussions and fun times both in and out of the lab. I would also like to thank Dr. Hugo Schmidt in the Physics Department for introducing me to the electrifying field of electrochemistry as an undergraduate.

I would like to express my sincere appreciation to all who contributed to the works in this dissertation. To our collaborators up north: Dr. Josephine Hill, Dr. Anand Singh, and Dr. Shamiul Islam. To our collaborators overseas: Dr. Marie Traulsen, Kion Norrman, Simone Sanna, and Dr. Mogens Mogensen. To our collaborator next door: David Driscoll and Dr. Stephen Sofie.

Finally, I would like to thank my committee members for helping to guide me through this journey.













## LIST OF FIGURES

Figure	Page
1.1. Schematic of Electrolyte- and Anode-Supported SOFCs .....	4
1.2. Schematic of the Ni-YSZ Three-Phase Boundary .....	7
1.3. Schematic of Metal Sintering Mechanisms .....	8
1.4. Raman Spectra from Ni-YSZ at 20 °C and 725 °C .....	11
1.5. Examples of LSV and EIS Data .....	13
1.6. The High Temperature Raman Spectroscopy System .....	15
2.1. <i>In Situ</i> Raman Spectra Collected during CO/H <sub>2</sub> Exposure at 675 °C .....	25
2.2. LSV and EIS Data with CO/H <sub>2</sub> at 675 °C .....	26
2.3. <i>In Operando</i> Raman Spectra from CO/H <sub>2</sub> Trials at 675 °C .....	28
2.4. G Peak Kinetics from CO/H <sub>2</sub> Trials at 675 °C .....	30
2.5. Chronopotentiometry Data from CO/H <sub>2</sub> Trials at 675 °C .....	31
3.1. Schematic of a CO/H <sub>2</sub> Test Cycle .....	42
3.2. Benchmark LSV and EIS Data with H <sub>2</sub> at 700 °C .....	45
3.3. <i>In Situ</i> Raman Spectra from CO/H <sub>2</sub> Trials at 675-800 °C .....	47
3.4. G Peak Kinetics from CO/H <sub>2</sub> Trials at 675-800 °C .....	48
3.5. LSV and EIS Data from CO/H <sub>2</sub> Trials at 700 °C .....	50
3.6. G Peak Kinetics and Chronopotentiometry Data from CO/H <sub>2</sub> Trials at 675-725 °C .....	53
3.7. Chronopotentiometry Data from SCP Tests with CO/H <sub>2</sub> 800 °C .....	55





## NOMENCLATURE

<u>Abbreviation</u>	<u>Definition</u>
A	Ampere
AC	Alternating Current
ASC	Anode-Supported Cell
C <sub>(s)</sub>	Adsorbed, elemental carbon
CA	Chronoamperometry
CCD	Charge Coupled Device
CGO	Gadolinium-Doped Ceria (or GDC)
CHP	Combined Heating and Power
CP	Chronopotentiometry
DeNO <sub>x</sub>	Selective Catalytic Reduction of NO <sub>x</sub> Gases
E <sub>a</sub>	Activation Energy
E <sub>o</sub>	Incident Energy (from laser)
E <sub>s</sub>	Scattered Energy (from Raman scattering)
EIS	Electrochemical Impedance Spectroscopy
FEM	Field Emission Microscopy
FTIR	Fourier Transform Infrared
ΔG°	Standard Gibbs Free Energy
GDC	Gadolinium-Doped Ceria (or CGO)
<i>I</i>	Current
<i>I</i> <sub>max</sub>	Maximum Current (measured at 0 V)
IR	Infrared
LSC	Lanthanum Strontium Cobalt
LSGM	Lanthanum Strontium Gallium Magnesium Oxide
LSM	Lanthanum Strontium Manganite
LSV	Linear Sweep Voltammetry
MEA	Membrane Electrode Assembly
MIEC	Mixed Ion-Electron Conductor
NIR	Near-Infrared
NO <sub>x</sub>	NO and NO <sub>2</sub> Gases
OCV	Open Circuit Voltage (measured at 0 A)
<i>P</i>	Power
<i>P</i> <sub>max</sub>	Maximum Power
<i>P</i> <sub>CO</sub>	Partial Pressure of CO
<i>P</i> <sub>CO2</sub>	Partial Pressure of CO <sub>2</sub>
<i>P</i> <sub>H2</sub>	Partial Pressure of H <sub>2</sub>
<i>P</i> <sub>H2O</sub>	Partial Pressure of H <sub>2</sub> O
<i>P</i> <sub>O2</sub>	Partial Pressure of O <sub>2</sub>
PEMFC	Polymer Electrolyte Membrane Fuel Cell
PLD	Pulsed Laser Deposition
<i>R</i>	Resistance

## NOMENCLATURE– CONTINUED

<u>Abbreviation</u>	<u>Definition</u>
$R_B$ .....	Bulk Resistance (x-intercept in EIS Nyquist plot)
$R_P$ .....	Polarization Resistance (EIS arc width in Nyquist plot)
$R_S$ .....	Series Resistance (x-intercept in EIS Nyquist plot)
RC.....	Resistor-Capacitor Circuit
RE.....	Rare Earth Element
SCP.....	Spectrochronopotentiometry
ScSZ.....	Scandia-Stabilized Zirconia
SDC.....	Samarium-Doped Ceria
SEM.....	Scanning Electron Microscopy
SOEC.....	Solid Oxide Electrolysis Cell
SOFC.....	Solid Oxide Fuel Cell
SO <sub>x</sub> .....	SO <sub>2</sub> and SO <sub>3</sub> Gases
ToF-SIMS.....	Time-of-Flight Secondary Ion Mass Spectroscopy
TPB.....	Three-Phase Boundary
TPO.....	Temperature Programmed Oxidation
UV.....	Ultraviolet
V.....	Volt or Potential
XPS.....	X-ray Photoelectron Spectroscopy
XRD.....	X-ray Diffraction
YSZ.....	Yttrium-Stabilized Zirconia
$Z_{imag}$ .....	Imaginary Impedance (capacitive response)
$Z_{real}$ .....	Real Impedance (pure resistance)

## ABSTRACT

Solid-state electrochemical cells are efficient energy conversion devices that can be used for clean energy production or for removing air pollutants from exhaust gas emitted by combustion processes. For example, solid oxide fuel cells generate electricity with low emissions from a variety of fuel sources; solid oxide electrolysis cells produce zero-emission  $\text{H}_2$  fuel; and solid-state DeNO<sub>x</sub> cells remove NO<sub>x</sub> gases from diesel exhaust. In order to maintain high conversion efficiencies, these systems typically operate at temperatures  $\geq 500^\circ\text{C}$ . The high operating temperatures, however, accelerate chemical and mechanical cell degradation. To improve device durability, a mechanistic understanding of the surface chemistry occurring at the cell electrodes (anode and cathode) is critical in terms of refining cell design, material selection and operation protocols. The studies presented herein utilized *in operando* Raman spectroscopy coupled with electrochemical measurements to directly correlate molecular/material changes with device performance in solid oxide cells under various operating conditions. Because excessive carbon accumulation with carbon-based fuels destroys anodes, the first three studies investigated strategies for mitigating carbon accumulation on Ni cermet anodes. Results from the first two studies showed that low amounts of solid carbon stabilized the electrical output and improved performance of solid oxide fuel cells operating with *syn-gas* ( $\text{H}_2/\text{CO}$  fuel mixture). The third study revealed that infiltrating anodes with Sn or BaO suppressed carbon accumulation with  $\text{CH}_4$  fuel and that  $\text{H}_2\text{O}$  was the most effective reforming agent facilitating carbon removal. The last two studies explored how secondary phases formed in traditional solid oxide cell materials doped with metal oxides improve electrochemical performance. Results from the fourth study suggest that the mixed ion-electron conducting  $\text{Zr}_5\text{Ti}_7\text{O}_{24}$  secondary phase can expand the electrochemically active region and increase electrochemical activity in cermet electrodes. The final study of lanthanum strontium manganite cathodes infiltrated with BaO revealed the reversible decomposition/formation of a  $\text{Ba}_3\text{Mn}_2\text{O}_8$  secondary phase under applied potentials and proposed mechanisms for the enhanced electrocatalytic oxygen reduction associated with this compound under polarizing conditions. Collectively, these studies demonstrate that mechanistic information obtained from molecular/material specific techniques coupled with electrochemical measurements can be used to help optimize materials and operating conditions in solid-state electrochemical cells.

## CHAPTER ONE

## INTRODUCTION

Motivation

Establishing environmentally sustainable power production infrastructures is one of the major challenges we face moving forward in the 21<sup>th</sup> century as the global population increases and electricity usage expands in underdeveloped regions around the world.<sup>[1]</sup> Fuel cells stand out as an attractive source of clean electrical power and are well suited to serve as stand-alone units, making these devices a practical solution in regions lacking established electrical power infrastructure.<sup>[2,3]</sup> Because they produce electricity electrochemically, fuel cells benefit from much higher conversion efficiencies than traditional combustion-based methods and, subsequently, require less fuel to generate electricity.<sup>[4,5]</sup> In particular, solid oxide fuel cells (SOFCs) are capable of reaching efficiencies greater than 70% in combined heating and power applications and have lower levels of regulated pollutants in their exhaust.<sup>[2,4]</sup> SOFCs can also be run in reverse as a solid oxide electrolysis cells (SOECs) to produce H<sub>2</sub> and/or CO fuels from the electrochemical reduction of H<sub>2</sub>O and/or CO<sub>2</sub>, respectively.<sup>[6-8]</sup> SOECs can, therefore, supply fuel to SOFCs (and vice versa) creating a reversible solid oxide system with effectively zero-emissions.<sup>[9]</sup>

Fuel cells have an important role to play in terms of environmental stewardship. Because the power sector is the largest contributor to air pollution and greenhouse gas emissions, the transition to renewable energy production is essential for meeting criteria



established to improve air quality and mitigate contributions to climate change.<sup>[10-12]</sup> For example, the Clean Power Plan proposed by the United States' government in 2015 calls for state-by-state emission standards designed to decrease CO<sub>2</sub> emissions from the power sector to 32% below 2005 levels by 2030.<sup>[13]</sup> In October 2016 members of the United Nations Framework Convention on Climate Change ratified the Paris Agreement and pledged to reduce greenhouse emissions in order to keep the rise in global temperature < 2 °C above preindustrial levels (with the ideal target < 1.5 °C).<sup>[14,15]</sup> In order to meet the goals set forth by the Clean Power Plan and the Paris Agreement, current fossil fuel-based combustion methods must be phased out and replaced with renewable power sources that have little to no emissions. SOFCs are poised to play a role in this transition since they can generate electricity from a variety of fuel sources and, because of their high efficiencies and low fuel rates (defined as the amount of fuel required to generate 1 kWh of electricity<sup>[16]</sup>), produce less CO<sub>2</sub> and H<sub>2</sub>O emissions than traditional combustion sources. Furthermore, electrochemical oxidation of fuels also generates negligible amounts of noxious compounds including NO<sub>x</sub>, SO<sub>x</sub>, O<sub>3</sub>, and Pb.

A small number of companies have already begun selling and/or field testing SOFC units; however, several challenges must be overcome before SOFCs can be mass produced on a global scale.<sup>[17,18]</sup> For example, chemical and mechanical cell degradation are common problems that plague SOFC components due to the high temperatures ( $\geq 600$  °C) required for device operation.<sup>[3,4,19]</sup> Temperature induced cell degradation can result from mechanical stresses due to adjacent materials with different thermal expansion coefficients, chemical decomposition of materials, formation of electronically

and/or ionically insulating phases, and corrosion of materials due to unintended reactions between the SOFC components and gas phase species.<sup>[19,20]</sup> All of these occurrences disrupt electrochemical processes within the cell resulting in lower output power and decreased device performance.

The next section describes the electrochemical processes that occur in SOFCs and highlights several challenges associated with traditional SOFC materials. Strategies designed to overcome these challenges are discussed in more detail in the following chapters and focus primarily on adding small quantities of metal or metal oxides (or doping) to traditional SOFC materials. Afterwards, a brief overview of the experimental techniques used in this work is presented. Lastly, a synopsis of the high temperature spectroscopic studies in the following chapters is presented.

### Solid Oxide Fuel Cells

A SOFC is comprised of two porous, electron conducting electrodes separated by a dense, oxide ion conducting electrolyte. Under normal operating conditions, an oxidant, typically air, is supplied to the oxygen electrode (cathode) while fuel is delivered to the fuel electrode (anode). Electrochemical reactions begin at the cathode where molecular oxygen is reduced producing oxide ions ( $O^{2-}$ ). These oxide ions diffuse through the electrolyte to the anode where they oxidize fuel (i.e.  $H_2$ ,  $CO$ ,  $CH_4$ ) generating electrons and gaseous products (i.e.  $H_2O$ ,  $CO_2$ ). The electrons are then conducted from the anode through an external circuit back (or load) back to the cathode. (Fig. 1.1)

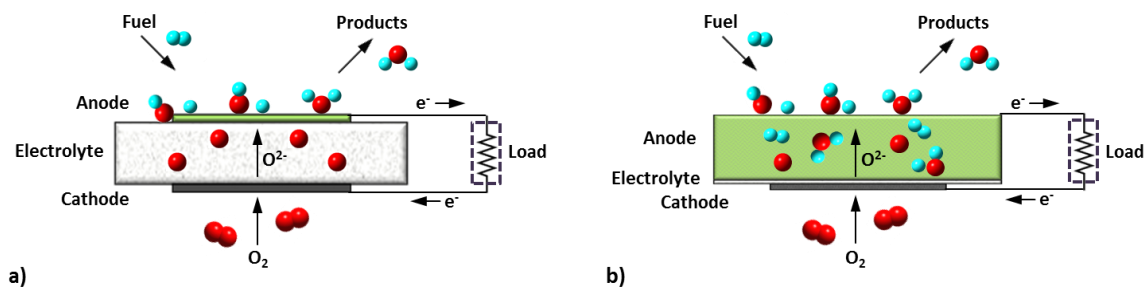


Figure 1.1. Schematics of (a) electrolyte-supported and (b) anode-supported SOFCs operating with  $\text{H}_2$  fuel to produce  $\text{H}_2\text{O}$  and electricity.

The simple, mechanically static design of SOFCs makes them well suited for both stationary and portable power applications with power requirements up to 250 kW.<sup>[3,18]</sup> Because they are comprised entirely of solid-state components, SOFCs can be utilized in a variety of applications ranging from commercial and residential buildings to ships and aircraft.<sup>[18,21,22]</sup> SOFCs also have the additional advantage of being less susceptible to poisoning from fuel contaminants due to the high operating temperatures, allowing for better fuel flexibility than lower temperature fuel cells.<sup>[20,23]</sup>

### Yttria-Stabilized Zirconia Electrolytes

SOFC operating temperatures are restricted primarily by the electrolyte material's ionic conductivity and chemical compatibility with the electrodes.<sup>[19,20]</sup> One of the most common SOFC electrolyte materials is yttria-stabilized zirconia (YSZ) because of its low cost and well-established processing methods.<sup>[24-26]</sup> The ionic conductivity of YSZ arises from mobile  $\text{O}^{2-}$  vacancies in the oxygen sub-lattice that form due to the charge compensation associated with the substitution of  $\text{Zr}^{4+}$  with  $\text{Y}^{3+}$  cations in the  $\text{ZrO}_2$  lattice.<sup>[25,27]</sup> Furthermore, doping zirconia with > 2 mol% yttria stabilizes the tetragonal

(~2-2.5 mol% yttria) and cubic ( $\geq 8$  mol% yttria) phases and prevents the non-ionic conducting monoclinic phase from forming  $< 1000$  °C.<sup>[25,28]</sup> In SOFCs, YSZ electrolytes are typically comprised of the 8 mol%  $Y_2O_3$  doped  $ZrO_2$  composition (8YSZ) since this material has the highest ionic conductivity and is chemically and mechanically stable over a wide range of temperatures and oxygen partial pressures.<sup>[3,20,25]</sup> However, the activation energy for oxide ion diffusion in YSZ (~100 kJ/mol) requires operating temperatures  $\geq 800$  °C in order to produce sufficient oxide ion diffusion necessary for generating acceptable current densities.<sup>[29,30]</sup> This temperature constraint limits anode and cathode materials to those having similar thermal expansion coefficients to YSZ ( $\sim 10 \times 10^{-6}$  K<sup>-1</sup> up to 1000 °C) and chemical stability at high temperatures.<sup>[31]</sup>

One strategy to lower operating temperature without modifying the electrolyte's composition is to fabricate SOFCs with thinner electrolytes (~10  $\mu$ m minimum thickness).<sup>[3,20]</sup> This approach requires cell architectures with either a thicker anode (anode-supported SOFC) or cathode (cathode-supported SOFC) in order to maintain structural integrity of the cell. This electrode-supported design works well at lower temperatures; however, electrolyte-supported cells are still required for SOFCs operating  $> 900$  °C.<sup>[32]</sup> Schematics of electrolyte-supported and anode-supported are shown in Figure 1.1a and Figure 1.1b, respectively. Experiments described in this thesis used both electrolyte- and anode-supported SOFCs.

### Lanthanum Strontium Manganite Cathodes

In addition to temperature restrictions associated with the electrolyte material, the activation energy associated with the oxygen reduction reactions at the cathode can also

limit operating temperature ranges. Lanthanum strontium manganite (LSM) is a traditional cathode material used in SOFCs with YSZ electrolytes that benefits from high operating temperatures due its high activation energy for oxygen reduction reactions ( $\sim 200$  kJ/mol at 700-900 °C).<sup>[20,31,33]</sup> The electrochemical and physical properties of LSM depend on Sr content in the LSM perovskite structure ( $\text{La}_{1-x}\text{Sr}_x\text{MnO}_3$ ) as well as cathode operating conditions. LSM cathodes typically have Sr concentrations ranging from  $x = 0.1$ - $0.2$  to maintain chemical and physical compatibility with YSZ.<sup>[31]</sup> Although these compositions are optimized for SOFCs with YSZ electrolytes, the mismatch in thermal expansion coefficients between LSM ( $\sim 11$ - $12 \times 10^{-6} \text{ K}^{-1}$  at 800 °C) and YSZ causes mechanical stresses that can lead to delamination of the LSM cathode from the YSZ electrolyte.<sup>[20,31,34]</sup>

In order to alleviate mechanical incompatibilities, composites of LSM and an ion conducting ceramic (typically the electrolyte material) are commonly used for SOFC cathodes.<sup>[20,31,34,35]</sup> These composites typically increase the ionic conductivity and improve the electrochemical performance of the cathode.<sup>[34]</sup> For example, LSM-YSZ composites with 50-70 wt.% YSZ have lower activation energies for oxygen reduction reactions (100-200 kJ/mol) and higher ionic conductivities than pure LSM.<sup>[31,35]</sup> These composites do, however, exhibit problems associated with the formation of electronically insulating phases ( $\text{La}_2\text{Zr}_2\text{O}$  and  $\text{SrZrO}_3$ ) and the segregation of Sr to the cathode surface; both of which have negative effects on the electrochemical processes within the cathode.<sup>[20,31]</sup> Although the formation of  $\text{La}_2\text{Zr}_2\text{O}$  and  $\text{SrZrO}_3$  can be avoided by keeping cell fabrication temperatures  $< 1300$  °C, preventing surface enrichment of Sr is more

difficult and requires operating SOFCs at lower temperatures, higher oxygen partial pressures at the cathode, and/or doping LSM cathodes with metal oxides.<sup>[31,36]</sup> Chapter 7 explores how infiltrating LSM cathodes with BaO inhibits Sr segregation and improves LSM's electrocatalytic properties at lower temperatures.

### Nickel Cermet Anodes

In order to minimize mechanical degradation of the anode due to thermal expansion, cermets are employed by mixing an ion conducting ceramic (typically the electrolyte material) with an electron conducting metal catalyst.<sup>[19]</sup> Ni-YSZ cermets are frequently used as SOFC anodes due to Ni's affordability, high electrical conductivity, and high catalytic activity relative to other anode cermets.<sup>[37]</sup> The electrochemical reactions in Ni-YSZ cermets are restricted to the three-phase boundary (TPB) where the ion conducting YSZ, the electron conducting Ni and the gas phase meet (Fig. 1.2). Therefore, the overall TPB length within the anode must be maintained and free of contaminants so that cell performance can proceed unhindered.

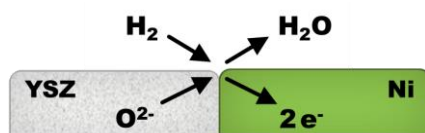


Figure 1.2. Schematic of the three-phase boundary (TPB) where electrochemical reactions occur in a Ni-YSZ cermet anode.

The high catalytic activity of Ni leaves Ni-YSZ anodes susceptible to carbon accumulation (or coking) from carbon containing fuels.<sup>[37-41]</sup> Excessive carbon accumulation can cause cell degradation and device failure via several mechanisms

including blockage of catalytic sites, obstruction of the anode pores impeding mass transport and carbon induced corrosion of the Ni catalyst (or metal dusting).<sup>[37,39,42-44]</sup> Several strategies for suppressing carbon accumulation on the anodes include polarizing cells at higher current densities, operating SOFCs at higher temperatures, and doping Ni-YSZ anodes with metals or metal oxides.<sup>[4,20,45-48]</sup> Chapters 2-3 explore how operational temperature and polarization conditions affect carbon accumulation on Ni-YSZ anodes exposed to *syn-gas*. Chapter 4 investigates how Ni-YSZ anodes infiltrated with Sn or BaO minimize carbon accumulation as well as the ability of H<sub>2</sub>O, CO<sub>2</sub>, and O<sub>2</sub> reforming agents to remove carbon on these anodes.

In addition to carbon formation, Ni-YSZ cermets can mechanically degrade due to anode oxidation. Because the molar volume of NiO is ~1.66 times larger than the molar volume of Ni, oxidation resulting from reduction/oxidation cycling can lead to fractures and/or delamination of the anode from the electrolyte.<sup>[49-51]</sup> Minimizing mechanical stresses caused by Ni/NiO transformations requires that anodes be reduced and oxidized at relatively slow rates as well as limiting the amount of times the anode is reduction/oxidation cycled.



Figure 1.3. Schematics of two possible mechanisms corresponding to metal sintering

Another challenge with Ni-YSZ anodes is associated thermal coarsening of Ni particles (or metal sintering) at high temperatures.<sup>[20,52]</sup> Studies indicate that thermal

coarsening of Ni is responsible for long-term degradation and decreased power efficiencies that arise from a loss of TPBs as the Ni particles merge.<sup>[52-54]</sup> Metal sintering is a consequence of the high surface free energy intrinsic to small particles and can occur via Ostwald ripening and/or Ni particle coalescence (Fig. 1.3).<sup>[55]</sup> The former describes atomic scale masses being transferred from smaller particles to larger particles, while the latter involves particles migrating towards each other. This agglomeration process causes irreversible mechanical deterioration of the anode and also affects other high temperature catalyst systems such as steam reforming reactors and catalytic converters.<sup>[56-58]</sup> Lower SOFC operating temperatures can be employed to slow thermal coarsening of the Ni particle.<sup>[49]</sup> Another strategy commonly used to reduce metal sintering is doping Ni-YSZ with metals or metal oxides.<sup>[59-61]</sup> Doping Ni-YSZ anodes with TiO<sub>2</sub> reduces thermal coarsening of Ni and chapter 5 explores how the formation of zirconium titanium oxide phases may contribute to the improve anode performance in these SOFCs.

### Experimental Methods

At typical SOFC operational temperatures blackbody radiation is prominent, rendering most optical measurement methods incapable of distinguishing relevant signals from a strong, non-resonant background. Raman spectroscopy performed with shorter wavelength light is less sensitive to blackbody background interference making this technique an ideal method for direct observation of the surface chemistry occurring in SOFCs.<sup>[62,63]</sup> Experiments presented in this work utilize *in situ/in operando* Raman spectroscopy to directly observe compositional and structural changes in SOFC materials under various thermal, atmospheric and polarization conditions. (*In situ* defines test



conditions where one or two of these operating conditions are similar to conditions in functional SOFCs while *in operando* denotes test conditions where all three operating conditions are representative of conditions in functional SOFCs.) Research described in the following chapters focus primarily on correlating *in situ/in operando* Raman spectroscopy with voltammetry and electrochemical impedance measurements. These techniques are briefly discussed below.

### Vibrational Raman Spectroscopy

Raman spectroscopy is a molecular/material specific technique that detects vibrational modes that can be used to monitor structural and compositional changes on the surface or within the bulk of a material.<sup>[62-64]</sup> Experiments are performed by irradiating the sample with monochromatic light from a laser in the visible or ultraviolet (UV), visible, or near infrared (NIR) region of the electromagnetic spectrum. Light can be scattered off of the sample by elastic (Rayleigh scattering) and inelastic (Raman scattering) processes. Rayleigh scattering is the strongest and occurs when the energy of the photon is preserved. Raman scattered radiation is produced when the incident, oscillating electromagnetic field induces a time dependent polarization providing a pathway for energy to be transferred between the incident photon ( $E_o$ ) and vibrational state of the sample. Stokes Raman scattering corresponds to scattered photons having lower energy ( $E_s < E_o$ ) as a result of an increase in vibrational state, while anti-Stokes Raman scattering corresponds to higher energy photons ( $E_s > E_o$ ) resulting from vibrational relaxation.

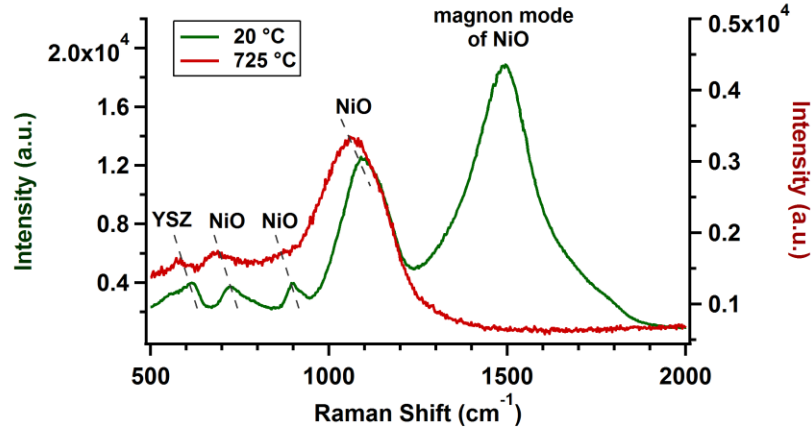


Figure 1.4. Representative Raman spectra acquired on a Ni-YSZ cermet anode at 20 °C (green) and 725 °C (red). The vibrational modes of NiO and 8YSZ broaden and shift to lower wavenumbers at the elevated temperature. The room temperature magnon mode of NiO at 1490  $\text{cm}^{-1}$  is only visible at temperatures  $< 500$  °C.

A Raman spectrum plots the intensity of the scattered light as a function of Raman shift energy (the energy difference between the incident and scattered photon,  $\Delta E = E_s - E_o$ ), where zero Raman shift energy corresponds to Rayleigh scattering. Since every material has a distinct phonon structure, Raman spectroscopy can be used to identify different chemical species and structures in Raman active materials at different temperatures, pressures and atmospheric environments.<sup>[65]</sup> For example, at room temperature, the Raman spectrum of nickel oxide is characterized by a strong feature at  $\sim 1090 \text{ cm}^{-1}$  whereas 8YSZ has a more complicated, low-frequency phonon structure dominated by a vibrational mode  $\sim 615 \text{ cm}^{-1}$ .<sup>[38,66]</sup> At elevated temperatures, the vibrational modes exhibit anharmonic broadening and shift to lower wavenumbers due to expansion of the crystalline lattices.<sup>[67]</sup> (Figure 1.4) In this thesis, all of the spectra come from Stokes Raman scattering and are plotted with the magnitude of the Raman shift energy.

### Electrochemical Diagnostics

Electrochemical measurements are acquired throughout the course of an experiment and provide real-time, quantitative information about cell condition and performance. Data from voltammetry and impedance measurements are used to construct equivalent circuit models and detailed kinetic mechanisms that attempt to quantify and predict the chemical processes responsible for electrochemical reduction/oxidation reactions, cell degradation, and enhanced device performance. For example, equivalent circuit models of data from impedance spectroscopy experiments are often used to identify individual contributions to the overall reactions and processes occurring in the electrolyte, the cathode, the anode, and gas phase.<sup>[68]</sup> In order to validate these models, techniques capable of directly identifying chemical species should be performed simultaneously with electrochemical measurements.

Voltammetry. Linear sweep voltammetry (LSV) is a technique commonly used to quantify and monitor cell performance. During a LSV experiment, a forward current ( $I$ ) is measured at the anode as an applied voltage, or overpotential ( $V$ ), is varied linearly across the cell. The data are then used to calculate the cell power ( $P = I \cdot V$ ) as a function of current. Typically, both voltage vs. current ( $V$ - $I$  trace) and power vs. current data ( $P$ - $I$  trace) are plotted on the same graph (Figure 1.5a). The slope of the  $V$ - $I$  trace plot corresponds to the total resistance and is inversely related to the maximum power ( $P_{\max}$ ) the cell can produce. For experiments presented in this work, LSV data were recorded starting at open circuit voltage (OCV) and ending at short circuit voltage at 0.0 V (corresponding to the maximum cell current,  $I_{\max}$ ) with a scan rate of 0.1 V/s. In the

following chapters, LSV measurements were performed to quantify how cell performance evolved throughout each experiment.

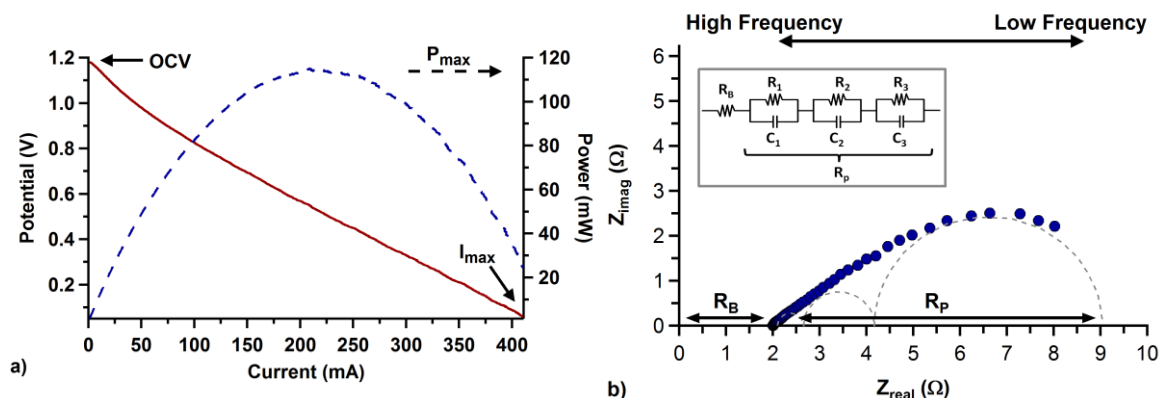


Figure 1.5. (a) LSV plot with  $V$ - $I$  (line) and  $P$ - $I$  (dashes) traces. (b) Nyquist plot of the EIS data showing the bulk and polarization resistances,  $R_B$  and  $R_P$ , with an inset of an example equivalent circuit used for modeling (dashes). Data were acquired at 700 °C from a Ni-YSZ anode-supported SOFC with a YSZ electrolyte and LSM cathode. Gas flows were 200 ml/min 50%  $H_2$ :50% Ar at the anode and 85 ml/min air at the cathode.

Electrochemical Impedance Spectroscopy. The condition of the cell and information pertaining to reaction rates can be inferred from electrochemical impedance spectroscopy (EIS) measurements.<sup>[68]</sup> In a potentiostatic EIS experiment, an alternating potential is applied to the cathode and the resulting AC current is measured at the anode. By comparing how the amplitude and phase differ between the input and output AC signals, one can calculate the real (or ohmic) and imaginary (or capacitive) contributions to the overall device impedance.<sup>[69]</sup> The ohmic and capacitive components dominate at low and high frequencies, respectively; consequently, tests must be conducted over a large frequency range. Attenuation of the output wave's amplitude is related to the sample's resistance ( $Z_{real}$ ) and reflects contributions from ohmic resistances of both the electrolyte and electrodes. The capacitive element ( $Z_{imag}$ ) is typically assigned to the two

electrolyte-electrode interfaces and will induce a phase shift in the output wave. Figure 1.5b shows a Nyquist plot of the EIS data and illustrates how data can be modeled with an equivalent circuit (i.e. an R-RC-RC-RC circuit). In this plot (Fig. 1.5b), the bulk resistance ( $R_B$ ) is the resistance related to oxide diffusion through the electrolyte while the polarization resistance ( $R_P$ ) is associated with anodic and cathodic processes such as charge transfer and fuel activation (in the middle region of the plot), and mass transport through the porous electrodes (corresponding to low frequencies).<sup>[68]</sup> Modeling EIS data with equivalent circuits is commonly used to evaluate the condition of the cell as the experiment progresses.<sup>[68-71]</sup> In the following chapters, impedance models from literature were used to evaluate EIS data collected throughout each experiment and assign any changes to processes occurring at the SOFC electrodes and/or electrolyte.

### High Temperature Experimental Assembly

The high temperature Raman spectroscopic studies presented in this work were performed using an experimental assembly shown in Figure 1.6. This assembly allows for control over sample temperature ( $\leq 900$  °C), gas composition delivered to each electrode, and polarization conditions. All of these experimental parameters are necessary to perform *in operando* Raman spectroscopic tests that identify directly how specific material changes affect SOFC performance and durability.

This system is well-designed for testing SOFC button cells with ~2.54 cm diameter. For electrochemical measurements and polarization control, metal mesh current collectors with Au wires are attached to the cell's electrodes with metal paste. The current collector area is typically smaller than the electrode surface area to allow

Raman spectra to be acquired from on the electrode. The cell is secured to an alumina tube with alumina paste (Ceramabond 522-VFG, Aremco), creating a gas-tight barrier between each electrode's gas atmosphere, and gas inlet tubes are positioned to flow fuel/oxidant gas across each of the electrodes (as indicated by the red and blue arrows in Fig. 1.6a). This assembly is encapsulated with a quartz tube and sealed at the bottom with a silicone stopper through which the current connector leads and gas delivery tubes run. The quartz tube allows optical access to SOFC. The assembly is then positioned in the tube furnace and heated slowly to the desired test temperature at a heating rate of  $\leq 1\text{ }^{\circ}\text{C}/\text{min}$  to minimize mechanical stresses between the cell and the alumina paste during heating.

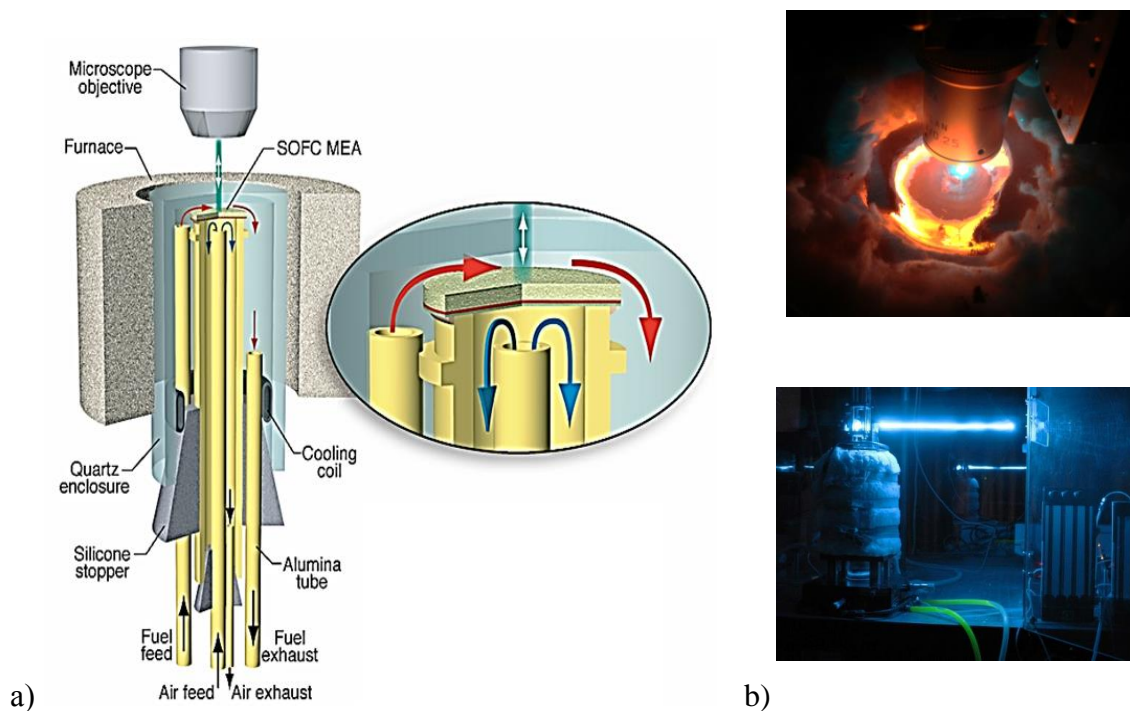


Figure 1.6. (a) Schematic\* and (b) pictures of the high experimental assembly used to acquire *in situ/in operando* Raman spectra with a 488 nm laser.

\*Courtesy of Dr. Robert Kee, Department of Mechanical Engineering, Colorado School of Mines

Experiments are conducted by focusing a continuous wave 488 nm laser (Lexel 85-SHG Ar-ion laser) onto the sample and collecting the scattered light with a Renishaw inVia Raman microscopy system equipped with a long pass edge filter assembly ( $\sim 150\text{ cm}^{-1}$  Stokes scattered light cutoff) and a Pelletier CCD detector. Since the setup is capable of measuring changes in surface polarizability with a temporal resolution of  $\geq 2$  seconds and a spatial resolution of  $\sim 2\text{ }\mu\text{m}$  (with 10x microscope objective), the structural transformations and formation of new species can be observed in real-time. This rapid identification of molecular species coupled with electrochemical measurements is crucial for evaluating reaction kinetics and reduction/oxidation mechanisms occurring at high temperatures. In the following chapters, this high temperature experimental assembly was employed to identify compositional and structural changes in SOFC materials *in operando* with the goal of determining the chemical mechanisms responsible for improved catalytic performance.

### Synopsis of High Temperature Studies

The collective work presented in following chapters demonstrate how Raman spectroscopy coupled with electrochemical measurements is an effective technique to gain mechanistic insight into strategies designed to improve the durability and stability of SOFCs. Chapters 2-3 focus on strategies for reducing carbon accumulation on SOFC anodes operating with *syn-gas*, a mixture of  $\text{H}_2$  and CO typically produced from reforming higher molecular weight hydrocarbon fuels or coal gasification. Specifically in Chapters 2 and 3, the effectiveness of operating temperature and polarization conditions to minimize carbon accumulation are investigated for Ni-YSZ anode-supported SOFCs.

The work presented in Chapter 4 examines how well Ni-YSZ anodes infiltrated with Sn or BaO suppress carbon accumulation with CH<sub>4</sub> fuel and the ability of reforming agents (H<sub>2</sub>O, CO and O<sub>2</sub>) to remove any carbon that does accumulate on the anode. Chapters 5-6 explore how the formation of secondary phases in modified SOFC materials affects cell performance. The work in Chapter 5 explores how the formation of the mixed ion-electron conducting Zr<sub>5</sub>Ti<sub>7</sub>O<sub>24</sub> secondary phase in ZrO<sub>2</sub>-TiO<sub>2</sub> systems may help to enhance cell performance by expanding the TPB in SOFC Ni-YSZ anodes doped with TiO<sub>2</sub>. The work presented in Chapter 6 identifies the formation of a Ba<sub>3</sub>Mn<sub>2</sub>O<sub>8</sub> secondary phase in BaO infiltrated LSM materials and discusses how oxygen reduction reactions are improved when this phase is present. Finally, the importance of *in situ/in operando* spectroscopy measurements in understanding the complex mechanisms of high temperature catalysts is discussed in Chapter 7.



## CHAPTER TWO

*IN SITU* SPECTROSCOPIC STUDIES OF CARBON FORMATION IN SOFCS  
OPERATING WITH SYN-GASContribution of Authors and Co-Authors

Manuscript in Chapter 2

Author: Melissa D. McIntyre

Contributions: Prepared samples and performed high temperature Raman spectroscopy and electrochemical measurements on anode-supported solid oxide fuel cell samples. Analyzed data, generated figures, and composed the manuscript in preparation for publication.

Co-Author: John D. Kirtley

Contributions: Aided in the acquisition of *in situ* Raman spectra and electrochemical measurements on the anode-supported solid oxide fuel cell samples.

Co-Author: David M. Halat

Contributions: Aided in the acquisition of *in situ* Raman spectra and electrochemical measurements on the anode-supported solid oxide fuel cell samples.

Co-Author: Kyle W. Reeping

Contributions: Aided in the preparation of samples for high temperature measurements.

Co-Author: Robert A. Walker

Contributions: Provided important insight into performing experiments and interpreting results. Aided in the preparation of the manuscript and figures.

Manuscript Information Page

Melissa D. McIntyre, John D. Kirtley, David M. Halat, Kyle W. Reeping, Robert A. Walker

Electrochemical Society Transactions

Status of Manuscript:

☐ Prepared for submission to a peer-reviewed journal

☐ Officially submitted to a peer-review journal

☐ Accepted by a peer-reviewed journal

☒ Published in a peer-reviewed journal

Published by the Electrochemical Society

In Volume 57, Issue 1, 1267-1275 (2013)

Reproduced by permission of ECS – The Electrochemical Society.

*IN SITU* SPECTROSCOPIC STUDIES OF CARBON FORMATION IN SOFCS  
OPERATING WITH SYN-GAS

M. D. McIntyre, J. D. Kirtley, D. M. Halat, K. W. Reeping, R. A. Walker

Department of Chemistry and Biochemistry, Montana State University, Bozeman,  
Montana 59717, USA

Abstract

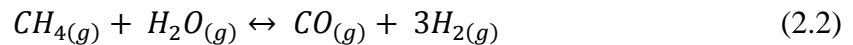
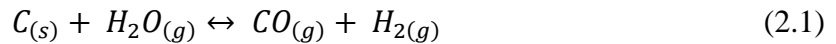
Vibrational Raman spectroscopy has been used to measure the rate and extent of carbon formation in SOFCs operating with CO/H<sub>2</sub> mixtures at 675 °C. The SOFCs consist of commercial Ni-YSZ anode-supported assemblies. Raman data show that carbon forms readily on anodes held at OCV and that the carbon deposits consist of highly ordered graphite as evidenced by a single band at 1561 cm<sup>-1</sup>. Polarizing the SOFC limits the amount of carbon that forms. At currents approaching 75% I<sub>max</sub>, where I<sub>max</sub> corresponds to a 0.0 V potential difference between the cathode and anode, observed carbon formation is completely suppressed. Interestingly, voltammetry data from these anode-supported assemblies are unstable until small amounts of carbon form. This correlation between carbon formation observed *in situ* and electrochemical performance raises interesting questions about the role played by carbon in charge transfer processes and current collection in functioning devices.

Introduction

The continued abundance of coal and emergence of new sources of natural gas (CH<sub>4</sub>) have renewed interest in energy conversion strategies that use carbon-based fuels

to produce electrical power cleanly and efficiently. Solid oxide fuel cells (SOFCs) are ideally suited to meet these challenges. SOFCs are electrochemical devices that convert fuel directly to electricity and products including CO<sub>2</sub> and H<sub>2</sub>O. Consequently, SOFCs operate with virtually no NO<sub>x</sub> or SO<sub>x</sub> emissions, and SOFC efficiency can be as high as 70% in combined heating and power applications.<sup>[2,5,20,72]</sup> Unlike other types of fuel cells such as polymer electrolyte membrane (PEMFC) devices, SOFCs are fuel flexible and can operate with a wide variety of feeds including H<sub>2</sub>, CH<sub>4</sub>, CO, higher molecular weight alkanes, and mixtures.<sup>[39,43,73,74]</sup>

One gas mixture that is an attractive fuel for SOFCs is *syn-gas*, a mixture of CO and H<sub>2</sub>.<sup>[74,75]</sup> From a *syn-gas* feed SOFCs can electrochemically oxidize CO and H<sub>2</sub> to CO<sub>2</sub> and H<sub>2</sub>O, respectively. Furthermore, *syn-gas* can be created from a variety of sources including coal through coal gasification (Eq. 2.1) and CH<sub>4</sub> through the water gas shift reaction (Eq. 2.2).<sup>[74-77]</sup>



*Syn-gas*, however, can also form carbon deposits on SOFC anodes either through the reverse reaction responsible for coal gasification (Eq. 2.1) or through reverse Boudouard chemistry (Eq. 2.3):<sup>[78]</sup>



Carbon formation – or “coking” – is one of the primary causes of SOFC anode degradation. Carbon formation impedes gas transport through porous anode structures and blocks electrocatalytic sites leading to diminished SOFC performance.<sup>[76,77,79]</sup> In

extreme cases, excessive carbon formation can force the SOFC anode to delaminate from the electrolyte causing irreversible device failure.<sup>[39,80]</sup>

Numerous models have been developed to parameterize conditions that lead to carbon formation from *syn-gas* and other carbon containing fuels on SOFC anodes.<sup>[81-84]</sup> Unfortunately, predictions from these models are difficult to validate in functioning SOFCs. High activation energies necessary to dissociate molecular oxygen at the SOFC cathode and to transport  $O^{2-}$  through the solid oxide electrolyte require that SOFCs typically operate at temperatures  $\geq 650$  °C.<sup>[85]</sup> Furthermore, conditions in SOFCs are either strongly reducing (cathode) or oxidizing (anode) and far from equilibrium when the cell is polarized. These conditions limit the experimental methods capable of measuring with material/molecular specificity the chemistry occurring on SOFC electrodes. Electrochemical methods can monitor overall device efficiency, and models can be constructed to *infer* details about chemical changes that occur during operation. *Ex situ* techniques such as X-ray photoelectron spectroscopy (XPS), scanning electron microscopy (SEM), and temperature programmed oxidation (TPO) can provide detailed descriptions of the carbon that forms on SOFC anodes but such experiments cannot monitor carbon formation directly.<sup>[76,80,86,87]</sup> Testing proposed mechanisms of carbon formation and the effects that deposited carbon has on SOFC operation requires direct, *in situ* measurements capable of identifying species present on these reactive, high temperature surfaces as a function of temperature, fuel feed conditions and device loading.

Experiments described below use vibrational Raman scattering coupled with linear sweep voltammetry (LSV) and electrochemical impedance spectroscopy (EIS) to examine the properties of SOFC anodes in devices operating with a *syn-gas* surrogate (50% CO/50% H<sub>2</sub> in Ar) at 675 °C. Data show that *syn-gas* forms carbon deposits quickly on anode-supported electrode assemblies (ASEs) but that the extent of carbon formation can be mitigated by polarizing the device to draw current. Of particular interest is how the extent of carbon formation affects overall SOFC performance. Electrochemical data show that prior to observable carbon formation, electrical power production is unstable with variation of ~50 mV in the voltage required to provide a constant current. This variation drops to < 1 mV once small amounts of observable carbon accumulate on the anode. Such observations raise interesting questions about the role of carbon in SOFC operation and suggest that small amounts of carbon within the anode microstructure may, in fact, improve SOFC stability.<sup>[88]</sup>

## Experimental Methods

### Sample Preparation and Experimental Assembly

ASEs used in these experiments were purchased from Materials and Systems Research, Inc. (Salt Lake City, UT) and measure 2.74 cm in diameter. The ASEs consist of a 0.8 mm thick Ni-YSZ cermet anode, with a 12 µm functional layer, and a 50 µm thick lanthanum strontium manganite (LSM) –YSZ cermet cathode, with a 15 µm functional layer. The anode and cathode are separated by a 10 µm thick dense YSZ electrolyte. Gold wire connected to a 25 mm<sup>2</sup> square of silver mesh was attached to the

anode with gold paste and served as the current collector. Similarly, a platinum mesh and platinum paste were used on the cathode. A spot of alumina paste was applied to the corners of the metal mesh to further secure the current collector to the electrode during heat up and at operating temperature. The cell was then fixed to a 2.5 cm diameter alumina tube with alumina paste and placed inside of a quartz tube. This assembly was positioned within a tube furnace and heated at  $\sim 1$  °C/min with the cathode under air and the anode under Ar gas. Once the sample temperature stabilized at  $675 \pm 5$  °C, the incident laser light was focused on the anode surface using a custom designed optical system.<sup>[79,89]</sup> The anode was then reduced under 100 mL/min H<sub>2</sub> with a 100 mL/min Ar carrier gas (benchmark flow rates), and 85 mL/min of air was flown over the cathode. Anode reduction was judged to be completed when the open circuit voltage (OCV) reached an asymptotic limit. For ASEs tested, this asymptotic OCV was  $1.18 \pm 0.02$  V at 675 °C. Anode reduction at this temperature typically required up to 5 hours.

### Vibrational Raman Spectroscopy

The vibrational excitation source was a CW 488 nm Ar-ion laser (35 mW) that was focused on the sample surface by a 10x long-working distance objective. The backscattered light was collected by the objective and then directed through an edge filter that filtered out light at the excitation wavelength and allowed only Stokes-scattered radiation to reach a CCD detector (Renishaw InVia Spectrometer). All vibrational Raman spectra were acquired with a single accumulation for a 10 second exposure time. Figure 2.1 shows representative spectra for carbon deposited on a Ni-YSZ anode with a mixture of H<sub>2</sub> and CO as the fuel. The prominent peaks at 595 cm<sup>-1</sup> and 1561 cm<sup>-1</sup> are

assigned to vibrational modes of YSZ and ordered graphite, respectively.<sup>[38,90]</sup> The initial scan at 0 seconds was collected before the cell was exposed to *syn-gas*.

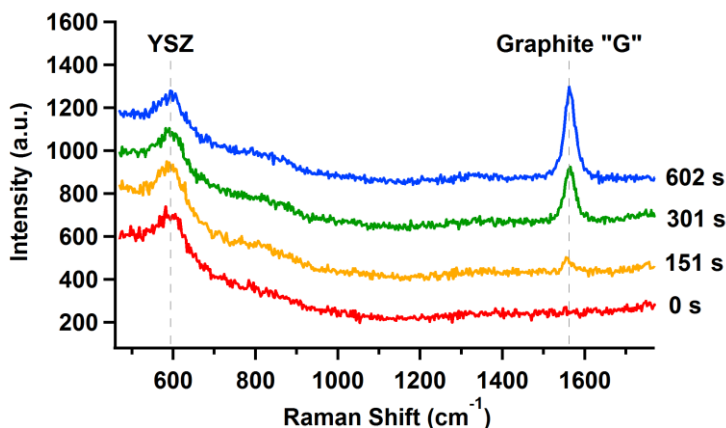


Figure 2.1. Raman spectra acquired every 10 seconds from an un-polarized (OCV) SOFC Ni-YSZ anode at  $675 \pm 5$  °C exposed to CO/H<sub>2</sub> for 10 minutes. The intensity of the ordered graphite structure, corresponding to the “G” peak ( $1561 \text{ cm}^{-1}$ ), shows that carbon is being formed on the anode. The YSZ signal ( $595 \text{ cm}^{-1}$ ) is also observed.

The formation and disappearance of carbon was monitored by continuously collecting Raman spectra from a single location on the ASE surface. The kinetics associated with the G peak growth were acquired in 10 second durations for CO/H<sub>2</sub> exposures up to 9 minutes. During the last minute of *syn-gas* exposure, an extended scan with a 10 second exposure time was acquired. The extended scan acquires data across the full frequency window available to the Raman spectrometer and shows several additional features that are not monitored during the kinetic scans.

### Electrochemical Measurements

To characterize how the *syn-gas* surrogate affects the electrochemistry of the device, LSV and EIS measurements were performed regularly for a given ASE (Fig. 2.2).



The power curve was calculated using the corresponding voltammetry data. EIS measurements were performed by applying an AC voltage of  $\pm 10$  mV to the cathode over a frequency range from 100,000-0.03 Hz.

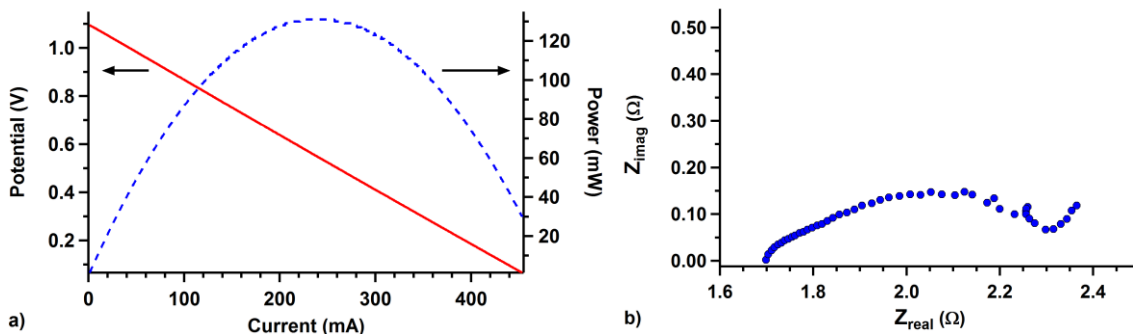


Figure 2.2. (a) Linear sweep voltammetry and (b) electrochemical impedance spectroscopy plots taken during *syn-gas* exposure. The solid line shows the potential (V) as a function of current (mA), and the dashed line corresponds to the power (mW).

LSV and EIS data were acquired with a Princeton Applied Research VersaStat MC prior to and post each *syn-gas* exposure. These measurements were performed to evaluate cell performance and condition throughout the course of the experiment. Over the course of a one day experiment consisting of multiple trials with *syn-gas*, cell performance diminished by up to 40%.

### Experimental Protocol

An experiment is defined as a sequence of trials, where a trial consisted of first exposing the anode to a mixture of 20 mL/min  $H_2$  and 20 mL/min CO with 100 mL/min Ar for 10 minutes under a constant current load (OCV, 25% $I_{max}$ , 50% $I_{max}$ , or 75% $I_{max}$  where  $I_{max}$  was measured by LSV during the first *syn-gas* exposure). During this time, Raman spectra were acquired at 10 second intervals to monitor the growth of carbon.

Following exposure to the *syn-gas* mixture, the anode chamber was purged for 4 minutes with humidified Ar (~2% H<sub>2</sub>O by mole fraction) to remove any residual carbon. The ASE was then reduced under the benchmark flow rates (described above). Once the OCV stabilized ( $1.18 \pm 0.02$  V), diagnostic measurements were performed to assess possible cell degradation. The H<sub>2</sub> gas flow was decreased to 20 mL/min following the benchmark diagnostics in order to minimize shocking the cell when the fuel was switched to *syn-gas* at the beginning of the next trial. The potential across the cell was monitored throughout the duration of each trial.

During the initial OCV trial, LSV and EIS data were acquired with the anode under *syn-gas*. The maximum current obtained from the LSV measurement was used to calculate the current loads for the proceeding trials (Table 2.1). The order in which a given current was drawn was randomly selected. For trial 6, the LSV and EIS were acquired during *syn-gas* exposure (Fig. 2.2) to examine how repeated cycling affected electrochemical performance.

## Results and Discussion

### Carbon Formation under *Syn-gas*

The extended Raman spectra (Fig. 2.3) taken at the end of the 10 minute *syn-gas* exposure reveal that carbon was present for all trials. The deposited carbon produced two distinct features corresponding to the "G" and "2D" vibrational modes at 1561 cm<sup>-1</sup> and 2699 cm<sup>-1</sup>, respectively. The G peak is associated with vibrations in highly ordered graphite.<sup>[91]</sup> The 2D signal is an overtone of the "D" vibrational mode and is associated

with electron-phonon coupling from the breathing modes of the  $sp^2$  carbon rings.<sup>[92]</sup> The broad double peak of the 2D feature can be attributed to the formation of multiple graphite layers.<sup>[93]</sup>

Table 2.1. The sequence of trials for an ASE experiment where  $I_{\max} = 429$  mA.

Trial	Current (mA)	G Peak Intensity* (arb. units)
1	OCV	442
2	OCV	429
3	214	130
4	322	40
5	107	324
6	OCV	379
7	214	88
8	107	219
9	322	24

\*Raman intensity of the G peak ( $1561\text{ cm}^{-1}$ ) at the end of the 10 minute *syn-gas* exposure.

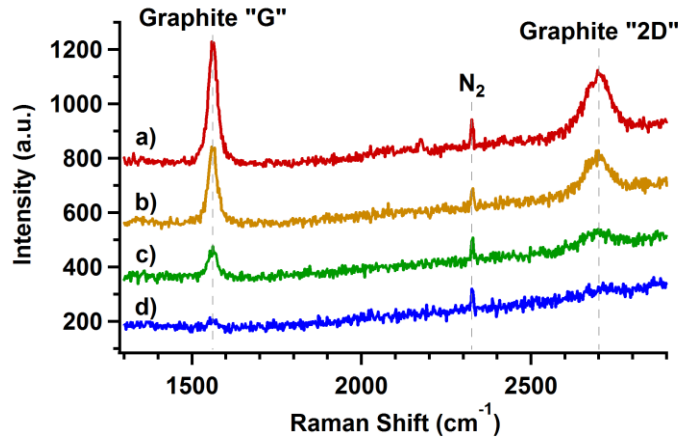


Figure 2.3. Raman spectra collected at the end of a 10 minute *syn-gas* exposure with the cell under various current loads: a) at open circuit voltage (OCV), b)  $25\%I_{\max} = 107$  mA, c)  $50\%I_{\max} = 214$  mA, and d)  $75\%I_{\max} = 322$  mA. The  $N_2$  peak results from air between the quartz tube and CCD detector and is not related to the SOFC.

The representative Raman spectra in Figure 2.3 show that significantly less graphite forms when the cell operates at higher currents. The decrease in signal is

attributed to an increase in the number of oxide anions diffusing through the electrolyte and oxidizing carbon at the anode.<sup>[74,90,94]</sup>

#### Electrochemical Data Corresponding to Presence of Carbon

The kinetics of carbon formation on Ni-YSZ anodes was explored by monitoring G peak growth as a function of cell polarization. Data showing G peak intensity versus time (Fig. 2.4) emphasize that the rate of carbon formation was highly sensitive to the amount of current being drawn with the onset of the graphite peak intensity occurring at later times with higher currents. The observed time delay and lower intensity when the device is under polarization results from rapid carbon oxidation at the Ni/YSZ/gas three-phase boundary (TPB) due to an increase in oxide anion flux through the electrolyte. In principle, carbon can also form on Ni surfaces and can contribute to the electrochemistry occurring at the ASE TPB via secondary mechanisms including Eq. 2.2. We believe that this carbon leads to a weak but observable signal even when the device operates at 75%  $I_{\max}$ .

Data in Figure 2.4 show a linear rate of carbon formation for trials with polarized cells, suggesting that carbon formation follows zeroth order reaction kinetics. Although the Raman data in Figure 2.4 show only intermittent spectroscopic evidence of graphite for the 75% $I_{\max}$  trial, voltammetry data shown below imply that carbon formed on the anode consistently. We speculate that carbon formation at these high currents occurred within the active layer of the ASE anode, a region that was inaccessible to the Raman scattering experiments. For trials at OCV, the curvature in the carbon formation rate

might imply a different growth mechanism, but more studies are needed to evaluate more accurately the microscopic details of anode coking.

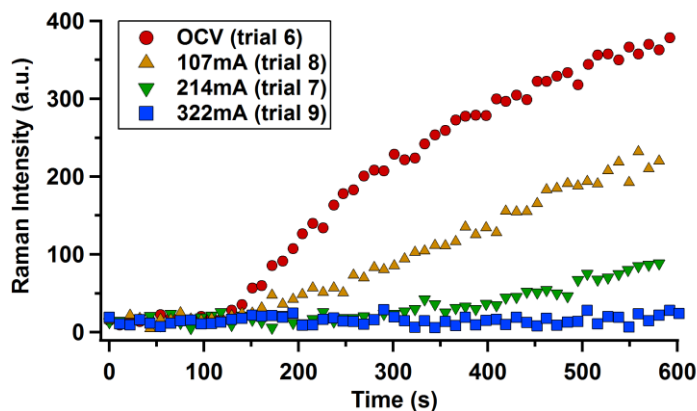


Figure 2.4. Kinetics plot of the G peak intensity for each of the trials shown in Figure 2.3. The *syn-gas* was turned on at 20 seconds and after 120 seconds the graphite began to form on the surface of the anode. The data show an inverse relationship between initial time of and extent of carbon deposition versus current load.

Carbon formation had an unusual and unexpected effect on the operating condition of the cell. Figure 2.5 shows the potential required to maintain a constant current for the kinetic traces shown in Figure 2.4. Specifically, fluctuations in the cell voltage are much more pronounced when Raman spectra show no observable carbon on the SOFC anode. During the initial period of *syn-gas* exposure, high frequency fluctuations of the cell potential occurred for all of the trials except when the cell was held at OCV. The appearance of the G peak coincided with a stabilization of the measured potential. Based on these results, we speculate that carbon deposited throughout the porous anode structure provides a conducting network for electrons to quickly reach the current collector. This response becomes important when monitoring the potential of devices under lean fuel conditions. If the potential becomes unstable,

introducing a carbon containing fuel to the system may help improve power efficiencies by promoting electron transfer from the anode to an outside load and back to the cathode. Further studies into how the presence of carbon affects the voltage and device performance at various currents are needed.

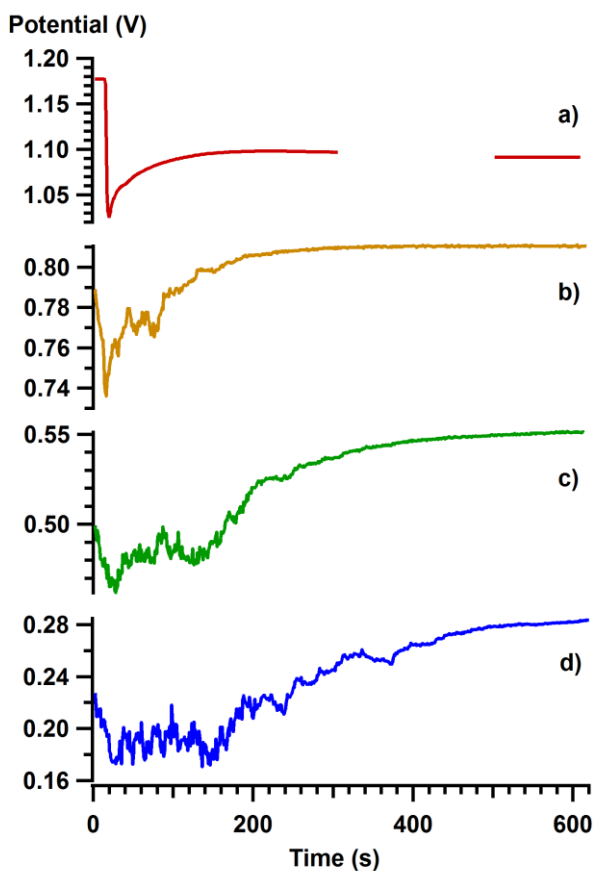


Figure 2.5. Plot of the cell potential as a function of time for the cell at: a) open circuit voltage (OCV), b)  $25\%I_{\max} = 107 \text{ mA}$ , c)  $50\%I_{\max} = 214 \text{ mA}$ , and d)  $75\%I_{\max} = 322 \text{ mA}$ . The time required for the potential to stabilize is inversely proportional to the current being drawn. In this plot, the *syn-gas* was introduced at 10 seconds. The voltammetry data shown here correspond to the spectroscopic data shown in Figure 2.4. We note that the measurement for a) was stopped after 300 seconds to acquire LSV and EIS data (Fig. 2.2) and was then restarted at 500 seconds to verify that the potential remained unchanged.

### Conclusions

The vibrational Raman spectroscopy data show that at 675 °C the formation of graphite on ASE assemblies under *syn-gas* is strongly dependent on polarization conditions and can help stabilize cell potential. The rate of graphite growth is inversely related to the current load and can be inferred from electrochemical measurements. The presence of carbon can increase electronic conductivity throughout the anode structure corresponding to a stable voltage with a variance of < 1 mV. Experiments are currently being conducted to determine the relationship between carbon formation and cell potential as a function of temperature.

### Acknowledgements

This work was supported by the Office of Naval Research (N00014-10-WX-1-0954). The authors gratefully acknowledge helpful discussions with Dr. Jeffrey Owrutsky and Dr. Michael Pomfret (both at U.S. Naval Research Laboratory). JDK gratefully acknowledges support from the Office of Naval Research through the University Laboratory Initiative (ULI, N00014-12-1-0199). DMH acknowledges support from Montana State University's Undergraduate Scholars Program and the Montana Space Grant Consortium.

## CHAPTER THREE

*IN OPERANDO* RAMAN SPECTROSCOPY STUDIES OF TEMPERATURE  
DEPENDENT CARBON ACCUMULATION ON SOFCS OPERATING WITH  
*SYN-GAS*

Contribution of Authors and Co-Authors

Manuscript in Chapter 3

Author: Melissa D. McIntyre

Contributions: Prepared samples and performed high temperature Raman spectroscopy and electrochemical measurements on anode-supported solid oxide fuel cell samples. Analyzed data, generated figures, and wrote the manuscript in preparation for publication.

Co-Author: Daniel M. Neuburger

Contributions: Aided in the acquisition of high temperature Raman spectra and electrochemical measurements on the anode-supported solid oxide fuel cell samples.

Co-Author: Robert A. Walker

Contributions: Provided important insight into performing experiments and interpreting results. Aided in the preparation of the manuscript and figures.



Manuscript Information Page

Melissa D. McIntyre, Daniel M. Neuburger, Robert A. Walker

The Journal of the Electrochemical Society

Status of Manuscript:

☐ Prepared for submission to a peer-reviewed journal

☒ Officially submitted to a peer-review journal

☐ Accepted by a peer-reviewed journal

☐ Published in a peer-reviewed journal

Publication anticipated by the Electrochemical Society

Submitted October 2016

*IN OPERANDO* RAMAN SPECTROSCOPY STUDIES OF TEMPERATURE  
DEPENDENT CARBON ACCUMULATION ON SOFCS OPERATING WITH  
*SYN-GAS*

M. D. McIntyre, D. M. Neuburger, R. A. Walker

Department of Chemistry and Biochemistry, Montana State University, Bozeman,  
Montana 59717, USA

Abstract

Carbon accumulation on Ni-YSZ anodes was investigated in anode-supported SOFCs operating with a 50/50 CO/H<sub>2</sub> *syn-gas* surrogate at temperatures ranging from 675-800 °C and under different polarization conditions. *In operando* Raman spectroscopy measurements showed suppressed carbon accumulation at elevated temperatures and under polarization conditions with high currents. The observed carbon deposits formed highly ordered graphite at temperatures  $\leq 750$  °C while no carbon was directly observed at 800 °C. Chronopotentiometry measurements, however, indicated that carbon was present at 800 °C and that polarizing at a constant current during CO/H<sub>2</sub> exposure limited carbon accumulation. At the lower temperatures, the appearance of graphite with CO/H<sub>2</sub> correlated with an OCV approaching 1.10 V and a stabilization of the cell potential during polarization. *In operando* Raman spectroscopy and electrochemical results suggest that low levels of carbon within Ni-YSZ anodes actually improve electrical conductivity throughout the anode microstructure.

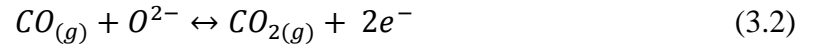
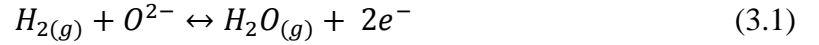
### Introduction

One strategy for reducing gas phase carbon emissions requires improving the conversion efficiency of systems that produce electricity from abundant fuel sources such as natural gas, coal, and biomass. In this context, solid oxide fuel cells (SOFCs) are attractive devices, capable of electrochemically oxidizing a wide variety of fuels with much higher efficiencies than conventional combustion methods.<sup>[95,96]</sup> However, the high activation energies for oxygen dissociation at the cathode and  $O^{2-}$  diffusion through the solid oxide electrolyte require SOFCs to operate at temperatures  $\geq 600$  °C.<sup>[31,97]</sup> These high operating temperatures permit SOFCs to utilize conventional fuels including natural gas as well as volatile biofuels (such as methanol and ethanol) and gas mixtures produced from coal gasification and anaerobic digestion of biomass (e.g. biogas).<sup>[98-102]</sup> Furthermore, high operating temperatures enable SOFCs to achieve conversions efficiencies  $\geq 70\%$  in combined heating and power applications.<sup>[102-104]</sup> This combination of fuel flexibility and high conversion efficiency makes SOFC technology a viable solution to energy demands by balancing electricity production from conventional fuel sources and providing a pathway for future alternative fuel production schemes.

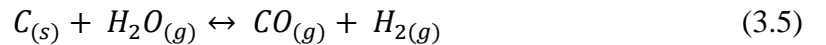
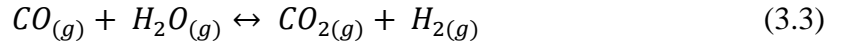
Fuel reforming is a common technique employed in SOFCs systems operating with carbon-based fuel sources in order to improve efficiency by converting the initial fuel into a  $H_2$ -rich gas mixture.<sup>[4,105-109]</sup> Fuel reforming systems typically add gas phase oxidants ( $H_2O$ ,  $CO_2$  and/or  $O_2$ ) to fuel sources to produce *syn-gas*, a gas mixture primarily comprised of  $H_2$  and  $CO$  with varying levels of  $CO_2$ ,  $H_2O$ , hydrocarbons, and trace contaminants (such as S, Cl, P and Sb complexes). *Syn-gas* composition depends

sensitively on both the initial fuel source and the reforming process conditions, and additional cleanup steps are often needed to remove adverse contaminants from ‘dirty’ *syn-gas* mixtures to prevent anode poisoning.<sup>[101,110,111]</sup> For example, Kee *et al.* shows representative *syn-gas* compositions from coal- and biomass-gasification with CO/H<sub>2</sub> mole ratios ranging from 2.01 to 0.765.<sup>[111]</sup> These ratios influence SOFC power densities with cell performance typically improving with lower CO/H<sub>2</sub> mole ratios in *syn-gas* mixtures.<sup>[112]</sup>

SOFCs operating with *syn-gas* can produce electricity via electrochemical oxidation of H<sub>2</sub> (Eq. 3.1) and CO (Eq. 3.2) at the anode.



High operating temperatures, low P<sub>O<sub>2</sub></sub> and SOFC anode catalysts also promote heterogeneous reactions including the water-gas shift (Eq. 3.3), the reverse Boudouard (Eq. 3.4) and carbon gasification (Eq. 3.5) reactions.



The formation/removal of carbon (via Eq. 3.4 and Eq. 3.5) is of particular importance for SOFCs with Ni-based cermet anodes. Carbon accumulation (or coking) occurs when the rate of carbon formation exceeds the rate of carbon removal. Under these circumstances, carbon accumulation in SOFC anodes has been shown to diminish cell performance as catalytic sites become blocked and carbon deposits restrict gas flow within the porous

anode.<sup>[113]</sup> Excessive carbon accumulation eventually leads to device failure due to corrosion of the Ni catalyst (metal dusting) and the delamination of the anode from the electrolyte.<sup>[114,115]</sup> The deleterious effects of coking necessitate operating SOFCs under conditions that have little to no carbon accumulation.

Thermodynamic calculations and kinetic models predict conditions where carbon accumulation from *syn-gas* is expected.<sup>[116-118]</sup> Under equilibrium conditions, carbon accumulation is favored at lower temperatures, higher CO/H<sub>2</sub> ratios and/or higher CO/CO<sub>2</sub> ratios. (Table 3.1) Specifically for temperatures below 700 °C, the reverse Boudouard reaction (Eq. 3.4) predicts that solid carbon should be the stable species;<sup>[117,119]</sup> therefore, SOFCs fueled with *syn-gas* should operate at higher temperatures to minimize carbon formation. However, polarized SOFCs create distinctly non-equilibrium conditions and questions about carbon accumulation and structure (graphitic or amorphous carbon) on the anode surface during operation depend on kinetic considerations as well as fuel composition, temperature and polarization conditions.<sup>[42,120]</sup>

Table 3.1. Gibbs energies calculated for the heterogeneous reactions with *syn-gas* at each of the tested temperatures.

Reaction*	$\Delta G_{948K}^{\circ}$ (kJ/mol)	$\Delta G_{973K}^{\circ}$ (kJ/mol)	$\Delta G_{998K}^{\circ}$ (kJ/mol)	$\Delta G_{1023K}^{\circ}$ (kJ/mol)	$\Delta G_{1073K}^{\circ}$ (kJ/mol)
$\text{CO}_{(g)} + \text{H}_2\text{O}_{(g)} \leftrightarrow \text{H}_{2(g)} + \text{CO}_{2(g)}$	-4.674	-3.879	-3.084	-2.289	-0.699
$2 \text{CO}_{(g)} \leftrightarrow \text{CO}_{2(g)} + \text{C}_{(s)}$	-4.506	-0.123	4.259	8.642	17.407
$\text{H}_{2(g)} + \text{CO}_{(g)} \leftrightarrow \text{H}_2\text{O} + \text{C}_{(s)}$	0.168	3.755	7.343	10.931	18.106

\*Thermochemical data for the forward proceeding reactions calculated using values from NIST-JANAF Thermochemical Tables (<http://kinetics.nist.gov/janaf/>).

Identifying material changes occurring in SOFCs *in operando* (defined by atmospheric, thermal, and polarization test conditions representative of realistic SOFC operating conditions) is challenging. Electrochemical techniques such as voltammetry and impedance spectroscopy provide real-time information about cell performance and can be modeled with equivalent circuits to infer changes in the cell's components under various operating conditions. These measurements, however, cannot directly identify material changes and average results over the entire membrane electrode assembly. In contrast, *post mortem* analyses (such as energy-dispersive X-ray spectroscopy, X-ray photoelectron spectroscopy, and temperature-programed oxidation) have chemical specificity but are incapable of assigning changes in performance directly to electrode chemical composition. In recent years, a number of non-invasive optical methods have been developed to probe SOFC surface chemistry under realistic operating conditions. Near IR thermal imaging, Fourier transform IR emission spectroscopy and vibrational Raman spectroscopy have all been employed to examine the molecular/material changes in SOFCs operating with various fuels.<sup>[41,121-125]</sup> When coupled with electrochemical measurements, these spectroscopic techniques directly correlate molecular/materials changes with electrochemical performance providing mechanistic insight into device degradation/improvement.

In the studies described below, *in operando* Raman spectroscopy and electrochemical measurements were performed to examine early time carbon accumulation on Ni-YSZ anode-supported SOFCs operating with a surrogate *syn-gas* mixture under various thermal (675-800 °C) and polarization conditions. Data show that

polarizing the cell and operating at elevated temperatures limited the extent of carbon accumulation. For all of the tested temperatures, carbon accumulated on anodes at open circuit voltage (OCV) and was suppressed when SOFCs were polarized at a constant current. Carbon was not observed in Raman spectra from experiments conducted at 800 °C; however, spectrochronopotentiometry (SCP) tests revealed that carbon was present in the anode functional layer under OCV conditions. These results demonstrate that the initial formation of graphitic carbon is a thermally controlled process that can be minimized by either operating at higher temperatures or operating SOFCs at high polarization currents at lower temperatures. One additional observation was that prior to the appearance of graphite with CO/H<sub>2</sub> under polarization, cell potentials were unstable and would fluctuate on the order of 10-100 mV from the average measured potential at a constant current. Interestingly, the accumulation of observable carbon coincided with a stabilization in the measured cell potentials data during polarization with fluctuations decreasing initially to < 10 mV when evidence of graphite first appeared in the Raman spectra and dropping to < 1 mV as graphite continued to accumulate. The corresponding Raman spectra and cell potentials indicate that a limited amount of graphitic carbon improved connectivity throughout the anode microstructure. These results suggest that intentionally coking the anode with limited quantities of carbon may be one strategy for stabilizing SOFC performance.

## Experimental Methods

### Sample Preparation and Experimental Protocol

Experiments were performed with anode-supported SOFCs purchased from Materials and Systems Research, Inc. The cells measured 27.4 mm in diameter and were comprised of a 0.8 mm thick (with a 12  $\mu\text{m}$  thick functional layer) Ni-YSZ cermet anode and a 50  $\mu\text{m}$  thick (with a 15  $\mu\text{m}$  thick functional layer) LSM-YSZ cathode separated by a 10  $\mu\text{m}$  thick YSZ electrolyte. Silver and platinum mesh (each 25  $\text{mm}^2$ ) current collectors were attached to the anode with gold paste and to the cathode with platinum paste, respectively.

Cells were heated to 675 °C, 700 °C, 725 °C, 750 °C, or 800 °C at <1 °C/min in an experimental test apparatus described previously.<sup>[126,127]</sup> During high temperature testing, 85 ml/min of air was supplied to the cathode and the anode was cycled under various fuel conditions to explore how operating temperature affected early time coking with CO/H<sub>2</sub>. The anode was first reduced with 100 ml/min H<sub>2</sub> and a 100 ml/min Ar carrier gas (benchmark flow rates) until the cell potential stabilized before a test cycle was performed. The time required to fully reduce the anode ranged from 2 hours at 800 °C to 5 hours at 675 °C. A test cycle (Fig. 3.1) began by exposing the anode to 40 ml/min of a 50%/50% CO/H<sub>2</sub> surrogate *syn-gas* mixture for 10 minute, followed by a 4 minute Ar purge of the anode chamber, and finally the carbon was removed from the anode with humidified Ar (~2% H<sub>2</sub>O).



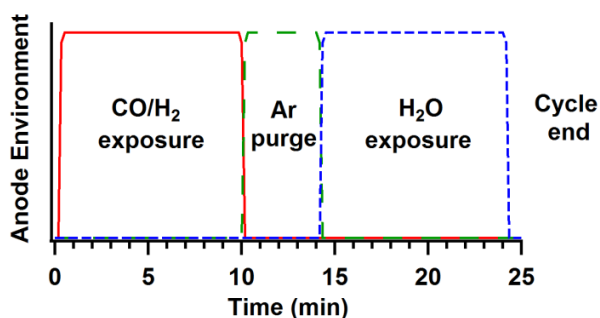


Figure 3.1. Schematic showing the gas exposure sequence for a test cycle. Carbon that formed during the 10 minute exposure to CO/H<sub>2</sub> was removed with H<sub>2</sub>O (via humidified Ar) at the end of the cycle. The anode was continuously exposed to the Ar carrier gas during each step of the cycle.

After the cycle, the anode was reduced under the benchmark flow rates. The first cycle was performed with the cell at OCV during CO/H<sub>2</sub> exposure after which cycles were repeated with the cell at OCV or under polarization during CO/H<sub>2</sub> exposure. Since carbon was not spectroscopically observed in experiments conducted at 800 °C, SCP tests were performed by replacing the last step in the CO/H<sub>2</sub> test cycle (exposure to humidified Ar) with a chronopotentiometry test under Ar. Under these polarization conditions in the absence of a gas phase fuel, carbon within the anode acted as a fuel source and was electrochemically oxidized in order to maintain a constant current through the cell. The potentiometric data from these SCP tests were then used to quantify carbon accumulation as a function of polarization condition. A minimum of two cells were tested at each operating temperature to verify results.

### Vibrational Raman Spectroscopy

Throughout each experiment, Raman spectroscopy and electrochemical measurements were conducted. Raman data were acquired with a 488 nm laser excitation

source (Lexel 85-SHG Ar-ion Laser) and Renishaw InVia Spectrometer equipped with a long pass edge filter assembly ( $\sim 150\text{ cm}^{-1}$  Stokes scattered light cutoff) and a Pelletier cooled CCD detector. Each Raman spectrum was collected using a 10x objective and 10 second exposure time. Extended Raman spectra (ranging from  $150\text{-}3200\text{ cm}^{-1}$ ) were collected on the anode prior to and near the end of the 10 minute of  $\text{CO}/\text{H}_2$  exposure. During  $\text{CO}/\text{H}_2$  exposure, static Raman spectra (ranging from  $267\text{-}1860\text{ cm}^{-1}$ ) were recorded continuously and the rate of carbon formation was determined by plotting the highly ordered graphite peak intensity at  $1561\text{ cm}^{-1}$  as a function of time.

#### Electrochemical Measurements

Voltammetry and electrochemical impedance spectroscopy (EIS) measurements were performed with a Princeton Applied Research VersaStat MC. Device performance was characterized with power versus current ( $P$ - $I$ ) and potential versus current ( $V$ - $I$ ) traces from linear sweep voltammetry (LSV) data. Cell condition was evaluated with the bulk ( $R_B$ ) and polarization ( $R_P$ ) resistances from EIS data recorded with a  $\pm 0.01\text{ V}$  amplitude over a frequency range of  $100,000\text{-}0.03\text{ Hz}$  (at the lower test temperatures) or  $100,000\text{-}0.01\text{ Hz}$  (at the higher test temperatures). In the Nyquist plots,  $R_B$  (the x-intercept at high frequencies) is attributed to the resistance associated with  $\text{O}^{2-}$  diffusion through the electrolyte and  $R_P$  (the arc width) is defined by impedances from electrochemical reactions and mass transport at the electrodes.<sup>[69]</sup> Based on this model, anode degradation over the course of an experiment corresponds to increasing  $R_B$  and  $R_P$  values.

## Results and Discussion

### Electrochemical Diagnostics with H<sub>2</sub>

Voltammetry and EIS measurements with H<sub>2</sub> were performed throughout each experiment to provide benchmark indicators of cell performance and condition. Under dry H<sub>2</sub>, cell OCV varied between 1.16 V and 1.25 V. Prior to the first CO/H<sub>2</sub> cycle, the average maximum power and R<sub>B</sub> were  $102 \pm 24$  mW and  $2.70 \pm 1.05$   $\Omega$ , respectively, for all of the tested cells. The measured OCV values under benchmark H<sub>2</sub> conditions were similar to their corresponding OCV values recorded prior to the initial CO/H<sub>2</sub> test cycle and did not decrease throughout each experiment indicating that no significant leaks formed between the cathode and anode during the experiments. Since these results demonstrate the structural integrity of the cells and acceptable isolation between the anode and cathode atmospheres, we assign spectroscopic and electrochemical changes to chemistry occurring within the anode microstructure.

During each experiment, the overall device performance decreased due to carbon accumulation from the CO/H<sub>2</sub> causing irreversible damage to the anodes. The reduced cell performance was more pronounced for cells tested at the lower temperatures compared to cells tested at the higher temperatures. This result is attributed to higher carbon loading during CO/H<sub>2</sub> test cycles at the lower temperatures. For example, benchmark LSV data recorded after nine CO/H<sub>2</sub> cycles showed that the average maximum power of cells tested at 675-725 °C decreased by ~14% and for cells tested at  $\geq 750$  °C, the maximum power decreased by ~3%. The accelerated degradation at lower temperatures coincided with higher resistances to charge transfer, as evidenced by steeper

slopes in the LSV data at lower currents (Fig. 3.2a) and by consistently larger  $R_B$  values in the EIS spectra (Fig. 3.2b). The higher resistances most likely resulted from degradation of the Ni network within the anode. Degradation of the percolated Ni network reduces electronic conductivity and leaves behind isolated Ni particles that are unable to participate in electrochemical oxidation reactions.

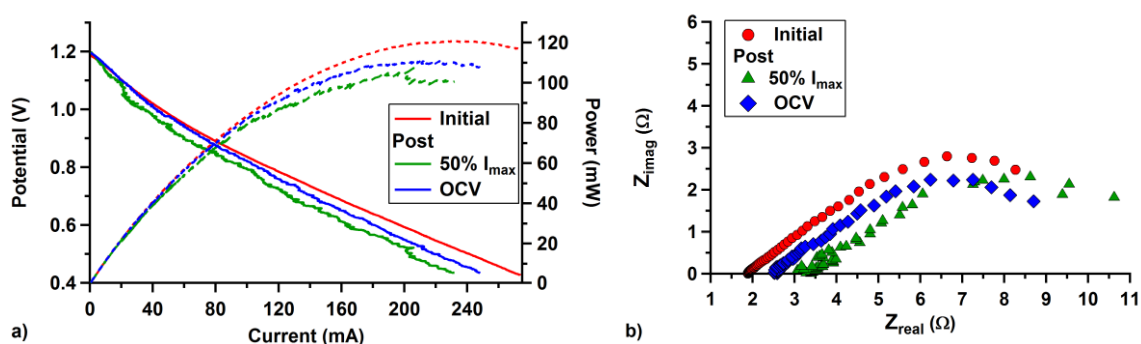


Figure 3.2. Comparison of benchmark (a) LSV and (b) EIS data at 700 °C collected with dry  $H_2$  before the first CO/ $H_2$  test cycle (initial) and after test cycles with the cell held at OCV or polarized at 227 mA (50%  $I_{max}$ ) during CO/ $H_2$  exposure. (a) Repeated CO/ $H_2$  cycling damaged the cell resulting reduced powers. (b) The corresponding EIS data show  $R_B$  increased from 1.88 Ω to 3.40 Ω as the cell degraded. Following test cycles with the cell under polarization, the voltammetry and EIS data exhibited larger levels of fluctuations compared to measurements performed after test cycles at OCV.

In addition to anode degradation and reduced cell performance, most cells exhibited erratic fluctuations in LSV and EIS data acquired with the benchmark  $H_2$ . These high frequency instabilities in the electrochemical data varied after each cycle and were dependent on cell condition and the CO/ $H_2$  cycling history. Fluctuations in the LSV and EIS data with  $H_2$  were more pronounced for benchmark measurements recorded after CO/ $H_2$  cycles where the cell had been polarized at higher currents (50% and 75%  $I_{max}$ ). Conversely, benchmark LSV and EIS measurements following CO/ $H_2$  cycles with the cell at OCV or polarized at lower currents (25%  $I_{max}$ ) appeared smoother. An example of

this behavior is presented in Figure 3.2 showing how the benchmark LSV (Fig. 3.2a) and EIS (Fig. 3.2b) changed between test cycles at 700 °C. Reduced fluctuations in the benchmark electrochemical measurements with H<sub>2</sub> were consistent with the appearance of graphitic carbon in Raman spectra acquired during the previous CO/H<sub>2</sub> cycle. Furthermore, the fluctuations were not observed in LSV and EIS collected during CO/H<sub>2</sub> exposure. These results suggest that electrical connectivity within the anode was improved under conditions with higher carbon loadings. In addition to more stable LSV and EIS data, the OCV values with H<sub>2</sub> increased after CO/H<sub>2</sub> cycling an average of 30 mV for each cell. Previous studies of Ni-YSZ anodes coked with CH<sub>4</sub> fuels have shown that OCV values increase when carbon accumulates in the anode.<sup>[90,128,129]</sup> Therefore, the higher OCV values measured after CO/H<sub>2</sub> cycles are attributed to residual carbon remaining in the anode after the tests. Data acquired during CO/H<sub>2</sub> cycles provide additional evidence for this claim and will be discussed in subsequent sections.

#### Syn-gas at OCV

For early time exposures to the CO/H<sub>2</sub> mixture, the extent of carbon accumulation on Ni-YSZ cermet anodes depended on temperature. Carbon was not observed in Raman spectra acquired at 800 °C while the spectra collected at the lower temperatures clearly show carbon accumulated on the Ni-YSZ anodes. *In operando* extended Raman spectra collected on the anodes after 10 minutes of CO/H<sub>2</sub> exposure are presented in Figure 3.3. Spectra of the anodes reduced with H<sub>2</sub> are included for comparison. The carbon deposits formed highly ordered graphite as evidenced by the strong vibrational bands at 1561 cm<sup>-1</sup>

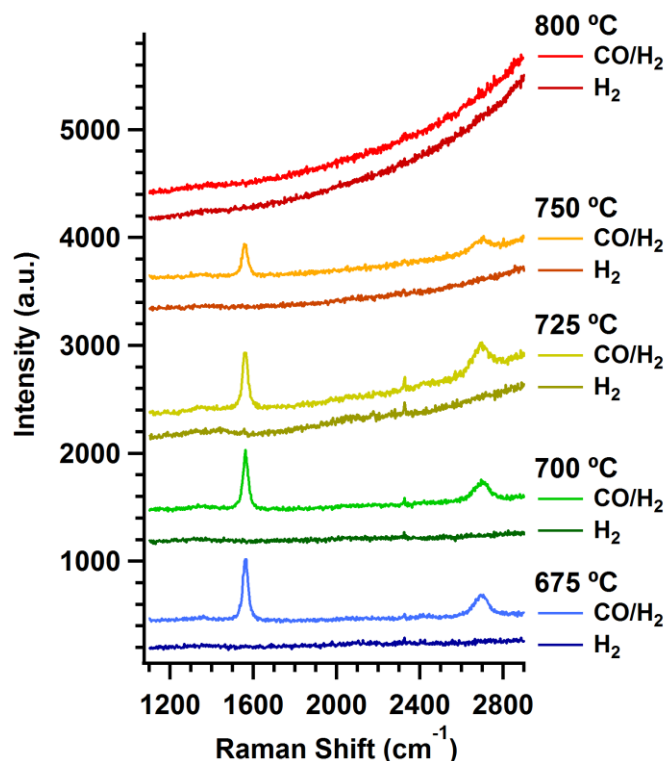


Figure 3.3. *In situ* Raman spectra collected with the anode exposed to CO/H<sub>2</sub> or H<sub>2</sub> at OCV at all of the tested temperatures: 675 °C (blue), 700 °C (green), 725 °C (yellow), 750 °C (orange), and 800 °C (red). The Raman features at 1561 cm<sup>-1</sup> and ~2700 cm<sup>-1</sup> arise from the G and 2D vibrational modes of highly ordered graphite, respectively. All spectra have been offset for clarity.

(G peak) and ~2700 cm<sup>-1</sup> (G' or 2D peak) that arise from the vibrations of sp<sup>2</sup> and sp<sup>3</sup> carbon bonds, respectively.<sup>[92]</sup> The most intense G peak was observed for experiments < 750 °C demonstrating that more carbon accumulated at the lower temperatures. For tests at ≤ 750 °C where carbon accumulation was spectroscopically observable, the ratio of the D and G peak intensities ( $I_D/I_G$ ) varied from 0.15 to 0.08 indicating that the carbon structures primarily formed sp<sup>2</sup> bonds. In addition to  $I_D/I_G$ , the ratio of the 2D and G peak intensities ( $I_{2D}/I_G$ ) provides information on the number of graphene layers in a sample. Based on work by Calizo *et al.*, the calculated  $I_{2D}/I_G$  from our high temperature

Raman spectra,  $0.37 \pm 0.02$ , corresponds to the formation of more than 5 graphene layers.<sup>[130]</sup> These results indicate that carbon accumulated initially as graphite films on the anode Ni catalyst during the early time exposure to the CO/H<sub>2</sub> mixture in our experiments. The rates of carbon growth at the different temperatures were examined by plotting the G peak intensity as a function of time (Fig. 3.4). The initial appearance of graphite occurred sooner for experimental temperatures below 700 °C. After the fuel was switched from H<sub>2</sub> to CO/H<sub>2</sub>, the G peak appeared within ~2 minutes at 675 °C and between 3-4 minutes for the tests at 700-750 °C. These results agree with thermodynamic results presented in Table 3.1 that predict carbon formation to be favorable at lower temperatures from the reverse Boudouard (Eq. 3.4) and reverse carbon gasification (reverse of Eq. 3.5) reactions.

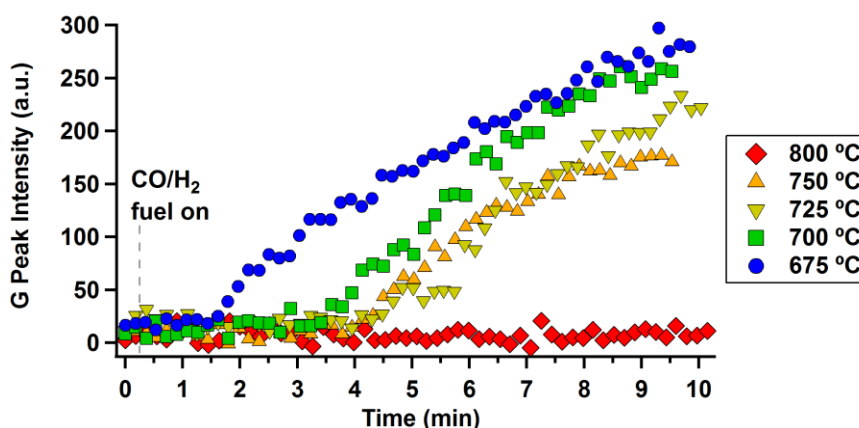


Figure 3.4. Carbon accumulation kinetics collected with the anodes exposed to the CO/H<sub>2</sub> gas mixture at OCV for each of the tested temperatures. Plotting the highly ordered graphite G peak intensity at 1561 cm<sup>-1</sup> as a function of fuel exposure time shows that the onset of carbon accumulation occurred earlier at the lower temperatures. The initial appearance of graphitic carbon on anodes at 700-750 °C occurred 1.5-2 times later than anodes at 675 °C. Carbon accumulation was not observed with Raman spectroscopy in the experiments at 800 °C.

The cell potentials provide additional insight into carbon accumulation with CO/H<sub>2</sub> as a function of temperature. At the end of the 10 minute CO/H<sub>2</sub> exposure, the cell OCVs ranged from 1.09-1.10 V for experiments at  $\leq 725$  °C, from 1.10-1.12 V for experiments at 750 °C and from 1.13-1.14 V for experiments at 800 °C. Changes are due to different operating temperatures and gas partial pressures ( $P_{H_2}$ ,  $P_{CO}$ ,  $P_{H_2O}$ , and  $P_{CO_2}$ ) within the anode functional layer. This OCV dependence on the partial pressures is supported by *in situ* Raman spectra that showed suppressed carbon accumulation at the higher temperatures and more carbon accumulated at the lower temperatures. Since carbon accumulation occurs when the rate of carbon formation exceeds the rate of carbon removal, the appearance and growth of carbon on the anodes will coincide with an increase in  $P_{CO_2}$  and/or  $P_{H_2O}$  via the reverse Boudouard reaction (Eq. 3.4) and the reduction of CO (reverse of Eq. 3.5), respectively, causing the measured OCV to decrease. Conversely, when the rate of carbon removal is equal to or faster than the rate of carbon formation, carbon will not accumulate on the anode but will be rapidly oxidized via the Boudouard reaction (reverse of Eq. 3.4) and/or carbon gasification reaction (Eq. 3.5) resulting in lower  $P_{CO_2}$  and  $P_{H_2O}$ , respectively, causing the measured OCV to increase. Contributions from the water-gas shift reaction (Eq. 3.3) are coupled the Boudouard and carbon gasification reactions and difficult to identify in our experiments.

In addition to monitoring cell potential, EIS and LSV measurements were periodically conducted with the anode exposed to the CO/H<sub>2</sub> fuel mixture. These measurements were performed after the anode had been exposed to CO/H<sub>2</sub> for ~9



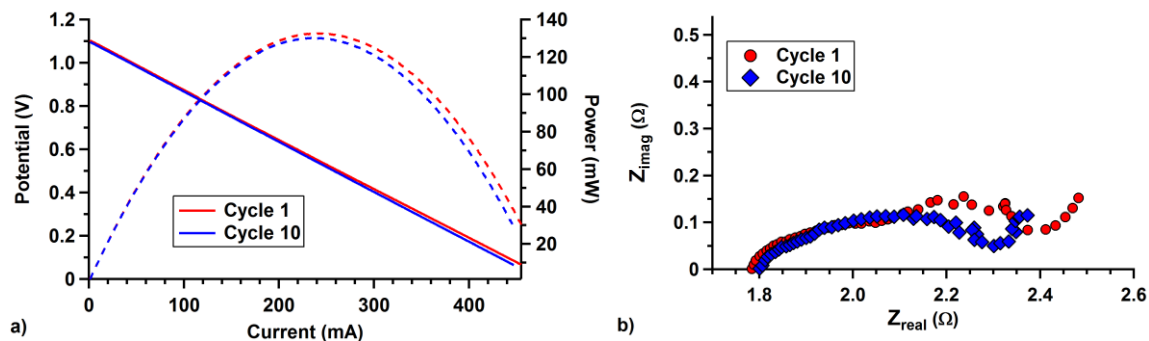


Figure 3.5. (a) LSV and (b) EIS data collected with the anode exposed to the CO/H<sub>2</sub> fuel mixture at 700 °C. (a) The decrease in cell performance between CO/H<sub>2</sub> cycles was less pronounced than with LSV acquired under the H<sub>2</sub> benchmarks between cycles. (b) After repeated cycling, the EIS data under OCV conditions exhibited a decrease in the low frequency arc associated with gas conversion reactions.

minutes under OCV conditions. In all of the experiments, the maximum powers with the CO/H<sub>2</sub> fuel were higher than those recorded with the benchmark H<sub>2</sub> flow rates. The EIS data revealed overall lower cell impedances with lower  $R_B$  and  $R_P$  values during CO/H<sub>2</sub> exposure. Figure 3.5 shows the LSV and EIS data with CO/H<sub>2</sub> acquired from the same cell shown in Figure 3.2 with H<sub>2</sub>. The improved cell performance with the CO/H<sub>2</sub> fuel was most likely due to a combination of processes within the anode that include: (1) the water-gas shift reaction (Eq. 3.3) increasing the concentration of H<sub>2</sub> fuel within the anode functional layer; (2) carbon within the anode acting as an additional fuel source; and (3) the carbon deposits improving electrical connectivity throughout the anode microstructure. Based on the close correlation between spectroscopically observed carbon and improved device performance, we propose that carbon deposits within the anode were the primary contributor to the lower impedances in EIS data collected with the CO/H<sub>2</sub> fuel mixture. Support for this idea is found in the EIS analysis of SOFCs operating with *syn-gas* by Kromp et al. where the low frequency arc in the Nyquist plot

(Fig. 3.5b) is ascribed to the water-gas shift reaction and moves to higher frequencies as  $P_{H_2}$  and  $P_{CO}$  increase.<sup>[131]</sup> In our studies, the feature in the EIS data associated with the water-gas shift reaction moved to higher frequencies after repeated CO/H<sub>2</sub> cycling indicating that  $P_{H_2}$  and  $P_{CO}$  increased within the anode over the course of an experiment. The higher  $P_{H_2}$  and  $P_{CO}$  after repeated cycling is attributed to the loss of Ni particles within the anode due to anode degradation. This loss of Ni catalyst surface area would reduce H<sub>2</sub> production via the water-gas shift reaction resulting in lower maximum powers in the LSV data; however, the maximum powers during CO/H<sub>2</sub> were similar after multiple cycles. Although carbon at the electrochemically active regions will act as a fuel source, H<sub>2</sub> oxidation is 2-3 times faster than carbon oxidation and will dominate electrochemical reactions for SOFCs with the 50/50 CO/H<sub>2</sub> gas composition.<sup>[122,128,132-135]</sup> Therefore, the lower  $R_B$  and  $R_P$  values with CO/H<sub>2</sub> are attributed carbon deposits improving connectivity throughout the anode microstructure. Additionally, the high frequency instabilities in LSV traces with H<sub>2</sub> diminished significantly once the anode has been loaded with carbon, as evidenced in Figure 3.2a. Improved connectivity within the anode microstructure with low levels of carbon loading has been proposed in previous studies and is discussed in greater detail below.<sup>[113,127,136,137]</sup>

### Syn-gas with Polarization

For experiments conducted at temperatures  $\leq 750$  °C, cells were polarized during CO/H<sub>2</sub> exposure under various constant currents corresponding to 25%, 50% or 75%  $I_{max}$  (where  $I_{max}$  corresponds to the maximum current from LSV data recorded during CO/H<sub>2</sub> exposure). Experiments performed at 675 °C were presented previously and showed that

the rate of carbon accumulation was inversely proportional to the polarization current with minimal graphite formation during CO/H<sub>2</sub> exposure at 75% I<sub>max</sub>.<sup>[127]</sup> Results presented in the current work expand upon those preliminary findings and provide a more in-depth analysis of carbon accumulation from the surrogate *syn-gas* mixture as a function of both operating temperature and polarization conditions.

*In operando* Raman spectra revealed that at all of the tested temperatures the initial appearance of carbon was delayed and carbon accumulation was suppressed when the cell was polarized at a constant current during CO/H<sub>2</sub> exposure. Carbon accumulation was reduced for experiments with 25% I<sub>max</sub> polarization at 700 °C, 725 °C and 750 °C while graphite was not observed in Raman spectra at the higher currents. Although graphitic carbon was not observed directly on these cells when polarized at 50% or 75 % I<sub>max</sub>, Raman spectroscopy was only able to detect the presence (or absence) of carbon on the anode surface. Any carbon that accumulated sub-surface, closer to the functional layer, had to be inferred from electrochemical measurements.

Previous studies using electrolyte-supported membrane electrode assemblies (with much thinner anodes) have shown close correlation between electrochemical data and spectroscopically observable carbon.<sup>[129]</sup> Specifically, changes in measured cell potential at OCV tracked the condition of the anode and served as an independent confirmation of carbon's presence as well as oxidation of the Ni itself to NiO. In line with these previous studies, cell potentials recorded during CO/H<sub>2</sub> exposure and subject to different polarizations at temperatures  $\leq 750$  °C are analyzed below and provide additional insight into carbon accumulation mechanisms.

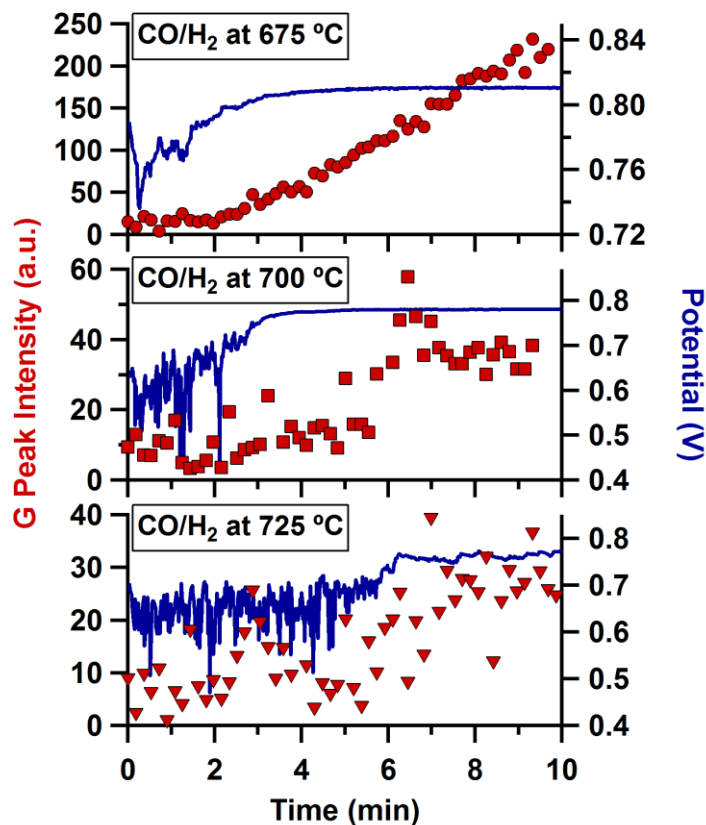


Figure 3.6. Cell potential and *in operando* Raman G peak intensity (symbols) as a function of time from three separate cells operating with the CO/H<sub>2</sub> fuel mixture at 675 °C (107 mA), 700 °C (114 mA), and 725 °C (125 mA). During test cycles with the cell polarized at a constant current, the appearance of graphitic carbon on the anode coincided with reduced fluctuations in cell potential.

When cells were polarized at constant current with the CO/H<sub>2</sub> fuel mixture, the measured cell potentials initially fluctuated on the order of 10-100 mV with respect to the average measured potential. The cell potential and *in operando* Raman spectra acquired during all of the polarized cycles at 675 °C exhibited a strong correlation between a reduction in cell potential fluctuations and an increase in G peak intensity as a function of time. Similarly for the 25%  $I_{\max}$  cycles at temperatures ranging from 700-750 °C, the cell potentials also became more stable as carbon accumulated on the anodes. Figure 3.6

shows the increase in G peak correlated with a dampening of cell potential fluctuations for CO/H<sub>2</sub> cycles polarized at 25%  $I_{\max}$  at 675 °C, 700 °C and 725 °C. For all of these cycles, the initial appearance of graphitic carbon in the Raman spectra coincided with a decrease in cell potential fluctuations to < 10 mV and as carbon continued to accumulate, as evidenced by the increasing Raman G peak intensity, the cell potential fluctuations decreased to < 1 mV. These results show that the level of carbon accumulation during our experiments did not hinder cell performance under constant current conditions for the limited CO/H<sub>2</sub> exposure of these cycles. Rather, the presence of carbon in the anode appeared to improve electronic connectivity between Ni particles allowing for electron charge transfer processes between the functional layer and current collector to proceed more easily. Although carbon was not directly observed for CO/H<sub>2</sub> cycles at 700-750 °C polarized at 50% and 75%  $I_{\max}$ , the cell potentials exhibited a similar reduction in fluctuations over the course of the 10 minute CO/H<sub>2</sub> exposure. These results imply that carbon accumulated within the anode functional layer under all of these conditions despite the inability of Raman spectroscopy to observe carbon formation directly.

Although the vibrational modes for graphite were absent in the Raman spectra acquired on the anode surface during experiments at 800 °C, the improved cell performance and reduced polarization resistance in the LSV and EIS data collected during CO/H<sub>2</sub> exposure implied that the carbon was present deeper in the anode. In order to quantify the extent of carbon accumulation in the anodes at this highest temperature, SCP tests were performed with the cell at OCV or polarized at 50%  $I_{\max}$  during CO/H<sub>2</sub> exposure (Fig. 3.7). Published work by Kirtley *et al.* has shown that SCP can be used to

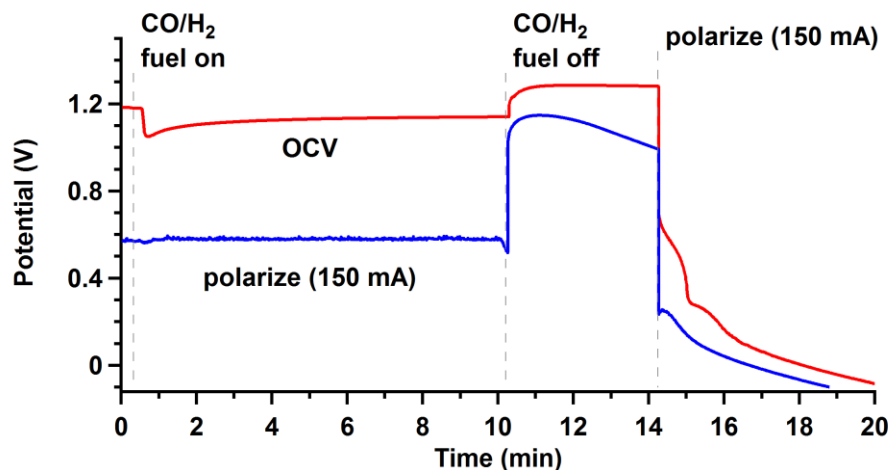


Figure 3.7. Cell potential as a function of time for two different cycles with SCP tests at 800 °C. The cell was held at OCV (red trace) or polarized under a constant current at 150 mA (blue trace) during CO/H<sub>2</sub> exposure for 10 minutes. The anode chamber was then purged with Ar while the cell was held at OCV for 4 minutes. Finally, the cell was polarized at 150 mA to electrochemically oxidize any carbon that had accumulated within the anode.

quantify carbon accumulation at the electrochemically active three-phase boundaries (TPBs) of coked Ni-YSZ anodes.<sup>[90]</sup> In their work, the authors proposed mechanisms for anode oxidation reactions during SCP tests and proposed that 1.38 mol of O<sup>2-</sup> are required to oxidize 1 mol of carbon (producing CO and CO<sub>2</sub>). Using this O<sup>2-</sup>/C mole ratio and the potentiometric data from our SCP tests at 800 °C, we estimated that ~0.31 mg (or  $2.6 \times 10^{-5}$  mol) of carbon had accumulated in the electrochemically active regions of the anode when exposed to CO/H<sub>2</sub> for 10 minutes at OCV (corresponding to 250 mg or  $8.9 \times 10^{-3}$  mol of CO). Based on these results when no current was drawn from the cell, ~0.29% of the carbon supplied to the anode remained at the electrochemically active regions. Conversely, carbon was undetectable in the potentiometric data acquired from SCP tests where the cell was polarized at 50%  $I_{\max}$  during CO/H<sub>2</sub> exposure. These

results clearly show that carbon accumulation is most effectively suppressed on the anodes producing high currents at 800 °C.

In conclusion, delayed and suppressed carbon accumulation with the CO/H<sub>2</sub> fuel mixture was the most pronounced for operating conditions that promoted heterogeneous reactions directly involving the carbon oxidation. As predicted by the thermochemical data, the Boudouard reaction (reverse of Eq. 3.4) and carbon gasification reactions (Eq. 3.5) were the most effective at minimizing carbon accumulation at the higher temperatures. Polarizing the cells helped to remove carbon via electrochemical oxidation at the TPBs as well as increasing P<sub>H<sub>2</sub>O</sub> and P<sub>CO<sub>2</sub></sub> via the electrochemical oxidation of H<sub>2</sub> (Eq. 3.1) and CO (Eq. 3.2). However, carbon removal reactions were enhanced to a greater degree by changing operating temperatures compared to changing polarization conditions.

### Conclusions

Temperature and polarization dependent carbon accumulation for early times exposures to a 50/50 CO/H<sub>2</sub> mixture were examined with *in operando* Raman spectroscopy combined with electrochemical diagnostics. Raman spectra show highly ordered graphite formed on cells operating at 675 °C, 700 °C, 725 °C and 750 °C. Although graphite was not directly observed in vibrational Raman spectra acquired at 800 °C, spectrochronopotentiometry tests confirmed the presence of carbon within the anode functional layer under OCV conditions and the absence of carbon within the anode under polarization. The rate of carbon accumulation was inversely related to both

operating temperature and polarization current. *In operando* Raman spectroscopy and electrochemical data showed a strong correlation between carbon accumulation on the anode and the reduced fluctuations in the measured cell potential under constant current conditions. The stabilization of cell potential corresponded with lower resistances to charge transfer reactions indicating that small amounts of carbon improved electronic conductivity within the anode.

#### Acknowledgements

This work was supported by the Office of Naval Research (N00014-10-WX-1-0954).



## CHAPTER FOUR

COMPARING *IN SITU* CARBON TOLERANCES OF SN-INFILTRATED AND BAO-INFILTRATED NI-YSZ CERMET ANODES IN SOLID OXIDE FUEL CELLS EXPOSED TO METHANEContribution of Authors and Co-Authors

Manuscript in Chapter 4

Author: Melissa D. McIntyre

Contributions: Aided in acquisition of *in situ* Raman spectra and electrochemical measurements on solid oxide fuel cell samples. Analyzed data, generated figures, and wrote the manuscript in preparation for publication.

Co-Author: John D. Kirtley

Contributions: Aided in acquisition of *in situ* Raman spectra and electrochemical measurements on solid oxide fuel cell samples. Edited/commented on the manuscript.

Co-Author: Anand Singh

Contributions: Fabricated solid oxide fuel cells and aided in acquisition of *in situ* Raman spectra and electrochemical measurements. Edited/commented on the manuscript.

Co-Author: Shamiul Islam

Contributions: Fabricated solid oxide fuel cells. Edited/commented on the manuscript.

Co-Author: Josephine M. Hill

Contributions: Provided important insight into performing experiments and interpreting results. Aided in the preparation of the manuscript.

Co-Author: Robert A. Walker

Contributions: Provided important insight into performing experiments and interpreting results. Aided in the preparation of the manuscript and figures.

Manuscript Information Page

Melissa D. McIntyre, John D. Kirtley, Anand Singh, Shamiul Islam, Josephine M. Hill,  
Robert A. Walker

The Journal of Physical Chemistry C

Status of Manuscript:

☐ Prepared for submission to a peer-reviewed journal

☐ Officially submitted to a peer-review journal

☐ Accepted by a peer-reviewed journal

☒ Published in a peer-reviewed journal

Published by the American Chemical Society

In Volume 119, Issue 14, 7637-7647 (2015)

Reprinted (adapted) with permission from DOI: 10.1021/acs.jpcc.5b01345.

Copyright 2015 American Chemical Society.

COMPARING *IN SITU* CARBON TOLERANCES OF SN-INFILTRATED AND BAO-INFILTRATED NI-YSZ CERMET ANODES IN SOLID OXIDE FUEL CELLS EXPOSED TO METHANE

M. D. McIntyre<sup>†</sup>, J. D. Kirtley<sup>†</sup>, A. Singh<sup>‡</sup>, S. Islam<sup>‡</sup>, J. M. Hill<sup>‡</sup>, R. A. Walker<sup>†</sup>

<sup>†</sup>Department of Chemistry and Biochemistry, Montana State University, Bozeman, Montana 59717, USA

<sup>‡</sup>Department of Chemical and Petroleum Engineering, University of Calgary, 2500 University Dr. NW, Calgary, Alberta T2N 1N4, Canada

Abstract

Experiments performed in this work explored how Ni-YSZ cermet anodes infiltrated with 1% Sn or 1% BaO mitigate carbon formation compared to undoped Ni-YSZ anodes in functioning solid oxide fuel cells (SOFCs). *In situ* vibrational Raman spectroscopy was used to study the early stages of carbon accumulation on the SOFC anodes at 730 °C with methane and under open circuit voltage (OCV) conditions. Additionally, carbon removal with different gas phase reforming agents was evaluated. The effects of these phenomena – carbon accumulation from methane and carbon removal by reforming agents – on the electrochemical capabilities of a device were monitored with electrochemical impedance and voltammetry measurements. Vibrational spectra showed that the undoped and 1% Sn infiltrated anodes were very susceptible to carbon formation from methane while considerably less carbon accumulated on the 1% BaO anodes. Electrochemical data, however, implied that carbon accumulated in different regions of the anode and that both Sn and BaO effectively reduced carbon accumulation but also inhibited electrochemical oxidation. For each anode, H<sub>2</sub>O was the

most effective reforming agent for removing carbon followed by O<sub>2</sub> and then CO<sub>2</sub>. H<sub>2</sub>O and CO<sub>2</sub>, however, left the anode only partially oxidized, while prolonged exposure to O<sub>2</sub> completely oxidized Ni to nickel oxide. The spectroscopic and electrochemical data showed strong correlations that provide mechanistic insight into the consequences of adding secondary materials to SOFC anodes with the intent of reducing carbon accumulation.

### Introduction

Carbon accumulation in energy conversion devices and catalytic reactors leads to diminished performance and, ultimately, system failure. This concern becomes increasingly important in high temperature applications where complex gas-phase pyrolysis reactions and activated surface chemistry can result in rapid carbon deposition.<sup>[138-140]</sup> Deposited carbon can block catalytic sites and, in some instances dissolve into the catalyst leading to a phenomenon known as metal dusting.<sup>[141-143]</sup> To prevent carbon from accumulating on catalysts, numerous strategies have been employed including gas phase reforming (with steam or CO<sub>2</sub>) and the development of novel catalysts. These catalysts include mixed bimetallic and/or metal-metal oxide materials<sup>[144-150]</sup> or traditional catalysts that are doped with small amounts ( $\leq 1-5\%$ ) of a secondary (2°) species.<sup>[141,151-153]</sup>

Ni-based catalysts used in SOFCs are particularly sensitive to carbon-induced degradation.<sup>[42,154,155]</sup> SOFCs consist of two electrocatalytic electrodes separated by an ion-conducting, solid oxide electrolyte. Molecular oxygen is reduced at the cathode (to

form  $O^{2-}$ ). The large activation energies required for  $O_2$  dissociation and for  $O^{2-}$  diffusion through the solid electrolyte require that SOFCs operate at temperatures typically above 650 °C. One advantage conferred to SOFCs by these high temperatures is fuel flexibility. Unlike low temperature fuel cells that use precious metal catalysts and can operate only with sources of clean hydrogen, SOFCs can convert a wide variety of fuels into products and electricity electrochemically. These fuels include natural gas, biogas, *syn-gas*, alcohols, and intermediate molecular weight alkanes.<sup>[109,154,156-159]</sup> All of these fuels, however, are also capable of forming solid carbon deposits on functioning SOFC anodes.

Nickel is the most common electrocatalyst used in SOFC anodes and in steam reforming applications because it is very effective at activating carbon-hydrogen bonds.<sup>[160-162]</sup> The accumulation of carbon must be prevented (either chemically or electrochemically), however, or active sites will be blocked and/or gas diffusion (through the porous anode) hindered. Depending on the identity of the incident fuel and operating temperature, these carbon deposits or ‘coke’ can assume different structures including carbon filaments,<sup>[163]</sup> highly ordered graphite<sup>[128]</sup> or disordered carbon that has a high density of grain boundaries and/or site defects.<sup>[89,114]</sup> The Ni catalyst is also susceptible to metal dusting where the SOFC anode simply disintegrates resulting in device failure.<sup>[114]</sup>

Recent reports have suggested that doping Ni-based catalysts with small amounts of 2° metals suppresses carbon accumulation.<sup>[47,164-168]</sup> Specifically, Ni anodes infiltrated with Sn have shown improved carbon tolerance in steam reforming applications,<sup>[48,169-171]</sup> although recent reports have shown that small amounts (1-5% by mass) of Sn added to

SOFC electrodes appeared to enhance carbon accumulation and destabilize SOFC anodes over the course of 24 hours relative to undoped electrodes.<sup>[48,172]</sup> Coking of conventional Ni cermet electrodes has been explored extensively by numerous groups using a variety of *in situ* and *ex situ* techniques.<sup>[76,90,100,173-176]</sup> Conversely, studies of infiltrated Ni-YSZ anodes have been limited mostly to methods unable to directly identify changes in anode structure and composition during operation. Techniques such as temperature programmed oxidation<sup>[37,47,177,178]</sup> and X-ray photoelectron spectroscopy<sup>[48,156]</sup> provide insight into how infiltrated anode structures change following operation under different conditions. Conclusions about the mechanisms responsible for electrochemical oxidation and anode degradation remain speculative, however, given that *post mortem* data do not report on chemical changes and their effects on electrochemical performance in real time. An advantage to coupling *in situ* techniques such as vibrational spectroscopy<sup>[125,179,180]</sup> with electrochemical measurements is that the material evolution of the SOFC anode can be related directly to the electrochemical condition of the device itself.

Studies described in this work used *in situ* vibrational Raman spectroscopy coupled with voltammetry measurements to examine directly the early stages of carbon formation from methane exposure at 730 °C on undoped Ni-YSZ cermet anodes and Ni-YSZ cermet anodes infiltrated with Sn or BaO (both 1% by mass with respect to Ni). Experiments also characterized the ability of different reforming agents (H<sub>2</sub>O, CO<sub>2</sub> and O<sub>2</sub>) to remove carbon after it accumulated on the three different anode types. Spectroscopic data were coupled with electrochemical measurements that monitored OCV as a function of local gas phase conditions. Results show that while anode

infiltration *can* mitigate carbon accumulation in the electrochemically active region of the anode, carbon deposits will still form on the top anode surface exposed directly to the fuel stream. The 1% BaO infiltrated anode shows the greatest ability to suppress carbon formation but the intrinsic chemical activity of BaO also leads to undesirable Ni oxidation even in the absence of any applied polarization.

## Experimental Methods

### Cell Fabrication and Assembly

Experiments described in this paper were performed on undoped and infiltrated samples that consisted of membrane electrode assemblies (MEAs) and Ni-YSZ cermet catalysts on YSZ substrates without cathodes (referred to as chip studies). Descriptions of the cell preparations have been given previously: Ni-YSZ,<sup>[135]</sup> 1% Sn-Ni-YSZ,<sup>[48]</sup> and 1% BaO-Ni-YSZ.<sup>[47]</sup> Briefly, electrolyte-supported cells with ~100  $\mu\text{m}$  thick anodes were used for this study. The anode powder was prepared by mixing NiO (50.6 wt.%, Alfa Aesar, USA) with YSZ (43.1 wt.%, TZ-8Y; Tosoh Co, Japan) and graphite (6.3 wt.%, Alfa Aesar, USA) by ball milling in acetone for 24 hours. The anode powder was mixed with glycerol and brush painted onto the electrolyte, followed by sintering at 1450 °C for 2 hours. The cathode powder was prepared by mixing  $\text{La}_{0.8}\text{Sr}_{0.2}\text{MnO}_3$  (40 wt.%, LSM, Praxair Specialty Ceramics, USA) with YSZ (40 wt.%) and graphite (20 wt.%). The cathode powder was mixed with glycerol and applied on the other side of the electrolyte and sintered at 1250 °C for 2 hours. The thicknesses of the cathode (LSM-

YSZ) and electrolyte (YSZ) were 80 and 600  $\mu\text{m}$ , respectively. The areas of the anode and cathode were both  $0.9\text{ cm}^2$ .

Sn was incorporated into the porous, sintered NiO/YSZ anode-substrate by impregnating a solution of  $\text{SnCl}_2 \cdot 2\text{H}_2\text{O}$  (Aldrich, USA) dissolved in ethanol, followed by calcination at  $500\text{ }^\circ\text{C}$  for 4 hours. BaO was incorporated by impregnating the anodes with an aqueous solution of  $\text{Ba}(\text{NO}_3)_2$  (Alfa Aesar, USA) followed by calcination at  $600\text{ }^\circ\text{C}$  in air to decompose the  $\text{Ba}(\text{NO}_3)_2$  to BaO.

For the MEAs, a metal mesh connected to a gold wire was attached to each electrode with metal paste (Heraeus) and acted as the current collector during electrochemical measurements. A silver mesh with gold paste and a platinum mesh with platinum paste were used on the anode and cathode, respectively. The cathode side of the MEA was attached to an alumina tube using ceramic paste (552 VFG, Aremco, USA), such that the cathode and anode were exposed to the gases flowing inside and outside the alumina tube, respectively. For the MEAs, this acted as a seal to isolate the two electrode chambers. This assembly was placed in a quartz tube (Quark Glass), sealed at the bottom with a silicon stopper, and positioned inside of a tube furnace. The sample was then heated to  $730\text{ }^\circ\text{C}$  at a rate  $\leq 1\text{ }^\circ\text{C}/\text{min}$  with low flow rates of Ar and air on the anode and cathode, respectively.

### Vibrational Raman Spectroscopy

Raman spectra were acquired *in situ* with a Renishaw InVia Spectrometer and a custom designed optical system. A 10x objective focused the 488 nm Ar-ion excitation source ( $\sim 18\text{ mW}$  before the objective) onto the sample, and the backscattered light was



directed through an edge filter ( $\sim 150\text{ cm}^{-1}$  cutoff) allowing for only Stokes scattered radiation to be measured by the charge-coupled device (CCD) detector. Vibrational Raman spectra were acquired continuously with a 10 second exposure per spectrum when recording kinetics data. Additional details about this assembly can be found in previously published reports.<sup>[180,181]</sup>

### Electrochemical Diagnostics

Voltammetry and electrochemical impedance spectroscopy (EIS) data were collected with a Princeton Applied Research VersaStat MC. Cell potentials were recorded with reference to the reduction of  $\text{O}_2$  on the cathode resulting in OCV data with negative values. Device performance was evaluated with linear sweep voltammetry (LSV) measurements and calculated power curves. To avoid damaging the MEA by drawing excessive current loads, LSV measurements were not carried out to the maximum current. The cell condition was assessed by the series ( $R_s$ ) and polarization ( $R_p$ ) impedances obtained from EIS data that were measured over a frequency range of 100,000-0.10 Hz with an AC voltage amplitude of 0.01 V. Impedance spectra were plotted on Nyquist plots where  $R_s$  is the purely resistive component at high frequencies associated with oxide ion transport through the electrolyte and electron transport in the current collectors and electrodes, and  $R_p$  is the impedance related to electrochemical reactions, fuel activation and mass transport.<sup>[182]</sup> Additional analysis and modeling of the individual contributions to  $R_p$  were not explored in this study.

## Procedure

Once the sample temperature had stabilized at  $730 \pm 5$  °C, the pristine anode was reduced with  $31 \pm 1$  mL/min  $H_2$  and benchmark electrochemical measurements were performed to assess how the addition of Sn and BaO affected the electrochemistry relative to the undoped Ni-YSZ sample. Throughout the course of an experiment, each sample underwent repeated cycling. A cycle (Fig. 4.1) began by exposing the anode to  $20 \pm 1$  mL/min  $CH_4$  for 10 minutes. The anode chamber was then purged with a continuous flow of Ar for 3-4 minutes before the addition of the gas oxidant ( $H_2O$ ,  $CO_2$  or  $O_2$ ) to remove the deposited carbon from the anode. To prevent the anode from fully oxidizing and suffering irreversible damage, exposure to  $O_2$  was limited to 3 minutes whereas exposure to  $H_2O$  and  $CO_2$  lasted for 10 minutes. Near the end of an experiment the  $O_2$  was allowed to flow for 10 minutes and completely oxidize the anode. Upon completion of a cycle the anode was re-reduced with  $H_2$ . Electrochemical measurements were again performed (with  $H_2$ ) to characterize cell condition and record how (or if) the carbon formation/removal cycles affected device degradation over the course of an experiment.

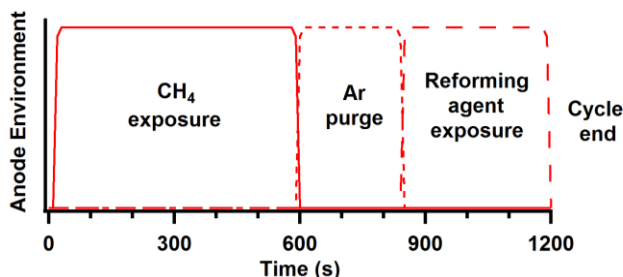


Figure 4.1. Schematic diagram showing the sequence of gas exposures during a single carbon formation/removal cycle. Both the  $CH_4$  and reforming agents were present at low partial pressures in an Ar carrier gas. Quantitative details related to residence times and gas flows are reported in Table 4.1.

In addition to experiments with functional SOFCs, chip studies were performed following the same protocol (excluding the electrochemical measurements) with flowing Ar on the side of the YSZ substrate opposite the Ni cermet catalyst. These tests were conducted to verify that the Raman data were not influenced by the air atmosphere (or leaks) on the cathode side of the functional SOFC MEA experiments. Since the Ni catalysts of the chip studies are structurally and compositionally equivalent to MEA anodes at OCV, they will be referred to as anodes throughout the remainder of this work.

Table 4.1 shows the flow rates and residence times for all three reforming agents between the point of introduction into the manifold and the anode. Variations in residence times result from adjustments in the gas handling manifold between experiments. Although the oxidant residence times ranged between 0.4 and 3.4 seconds, these times are less than the spectroscopic temporal resolution of 10 seconds.

Table 4.1. Representative flow parameters for each MEA experiment.

Oxidant	Flow Rate <sup>a</sup> (mL/min)	Oxidant in Gas Flow (%)	Gas Residence Time (s)
Ni-YSZ <sup>b</sup>			
H <sub>2</sub> O	2 ± 0.1	2	1.1
CO <sub>2</sub>	13.4	11.2	1.9
O <sub>2</sub>	12.0	10.2	2.4
1% Sn-Ni-YSZ			
H <sub>2</sub> O	4 ± 0.1	2	0.4
CO <sub>2</sub>	13.4	6.3	2.8
O <sub>2</sub>	13.4	6.3	3.4
1% BaO-Ni-YSZ			
H <sub>2</sub> O	4 ± 0.1	2	0.5
CO <sub>2</sub>	13.4	6.3	1.6
O <sub>2</sub>	13.4	6.3	2.1

<sup>a</sup>Uncertainties are ± 0.5 mL/min unless stated otherwise. <sup>b</sup>Tests from previous studies exploring how flow rate effected carbon removal.<sup>[135]</sup>

All experiments were conducted with the MEA held at OCV. The cell potential was monitored continuously during each cycle with the various atmospheric conditions (including an Ar carrier gas flow rate of  $200 \pm 2$  mL/min) above the anode and a constant flow of air ( $143 \pm 2$  mL/min) over the cathode. Under these conditions, any changes in the OCV can be attributed to reactions at the three-phase boundaries (TPBs) in the anode including charge transfer reactions, changes in anode composition and relative concentrations of adsorbed and gas phase species. Experiments performed with full MEA assemblies at OCV and chips (with anodes only) led to carbon accumulation and removal kinetics that were consistent within experimental uncertainty.

We note that a leak between the cathode and anode would result in chemical (vs. electrochemical) carbon and Ni oxidation and unstable electrochemical data; however, at the beginning of an experiment, a leak test was performed to ensure that the atmosphere above the anode was not affected by the cathode atmosphere. Additionally, the measured OCV values were similar for the H<sub>2</sub> benchmark experiments performed after each cycle indicating that leaks did not form during experiments. Since these results support MEA structural integrity and atmosphere separation between the anode and cathode, we attribute changing spectroscopic and electrochemical data to surface chemistry specific to the anode materials.

## Results and Discussion

Studies described in this work examined several issues relevant to high temperature surface chemistry in SOFCs including the tendency of carbon to accumulate

on Ni-based cermet anodes infiltrated with either Sn or BaO exposed to methane and the effects of carbon accumulation on device performance. Also explored was the ability of different reforming agents to remove accumulated carbon. Three different types of anodes were tested using two different techniques and three different reforming agents. For clarity, we separate the Results and Discussion section into two parts: the first part considers the impact of Sn and BaO on carbon formation and the second part examines the effects of these dopants on carbon removal by reforming agents.

#### Carbon Formation with CH<sub>4</sub>

Results. Under H<sub>2</sub> and prior to methane exposure, the cell OCV for the undoped cell and the 1% Sn infiltrated MEA were  $-1.22 \pm 0.01$  V while OCV for the 1% BaO infiltrated MEA was  $-1.17 \pm 0.01$  V. Distinct differences in the electrochemistry between each cell type were emphasized in LSV and EIS data. Representative results are shown in Figure 4.2. These data show that differences between the anodes existed both prior to any exposure to methane (Fig. 4.2a and 4.2b) and persisted after repeated cycling with methane (Fig. 4.2c and 4.2d). Over the course of an experiment (consisting of multiple carbon accumulation and removal cycles), MEA performance suffered but remained higher for the undoped Ni-YSZ compared to the infiltrated anodes (Fig. 4.2c). Cell performance for the MEA with BaO infiltrated anodes was consistently lower than for the MEA with Sn infiltrated anodes. In addition to lower conversion efficiencies, EIS measurements for the infiltrated anodes (Fig. 4.2b and 4.2d) exhibited similar  $R_s$  values as the undoped MEA ( $\sim 5 \Omega$ ) but higher  $R_p$  values (ranging from 24-34  $\Omega$  and 35-103  $\Omega$

for the Sn and BaO infiltrated anodes, respectively) compared to the undoped cell (ranging from 15-20  $\Omega$ ).

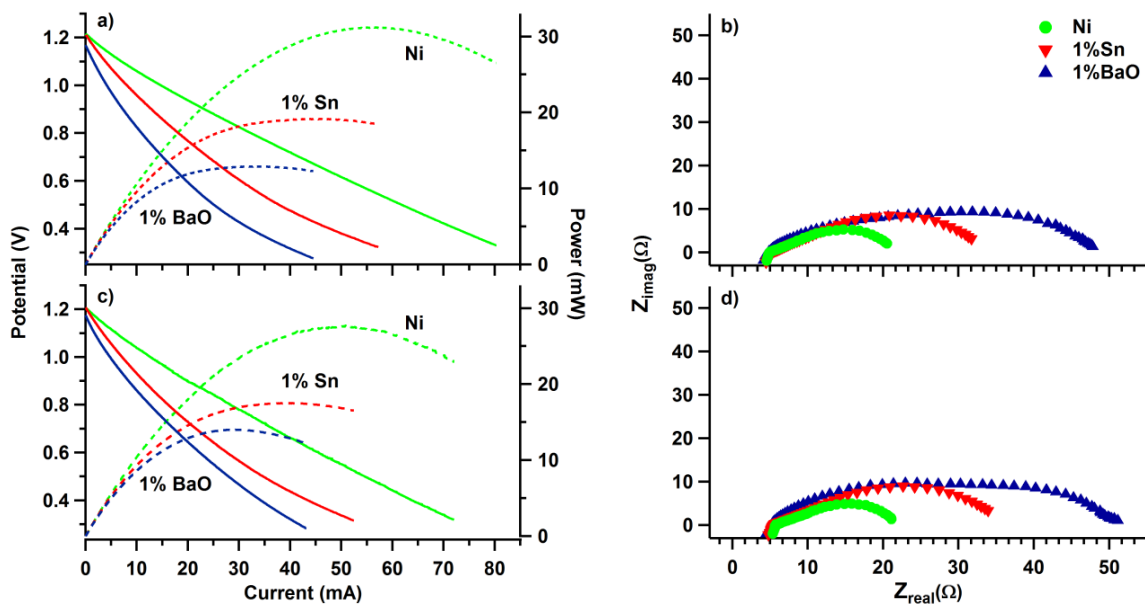


Figure 4.2. Benchmark electrochemical measurements collected for undoped and infiltrated Ni-YSZ MEAs operating with  $\text{H}_2$  at 730  $^{\circ}\text{C}$  (a, b) prior to exposure to  $\text{CH}_4$  and (c, d) after repeated cycling. The  $V-I$  and  $P-I$  traces in (a, c) correspond to the solid and dashed lines, respectively. Note that the voltammetry data do not extend to short circuit voltage (0 V) or, equivalently,  $I_{\text{max}}$ . Electrochemical impedance spectroscopy data are shown in (b, d).

Raman spectra acquired from the different anodes exposed to  $\text{CH}_4$  show that carbon accumulated on all three anode types with the smallest amount of carbon forming on the 1% BaO infiltrated anodes (Fig. 4.3a). The deposited carbon on all three anodes was comprised predominantly of highly ordered graphite as evident by the sharp “G” peak at 1561  $\text{cm}^{-1}$ . For all of the anodes, YSZ, graphite and NiO were the only chemical species observed in the Raman spectra.

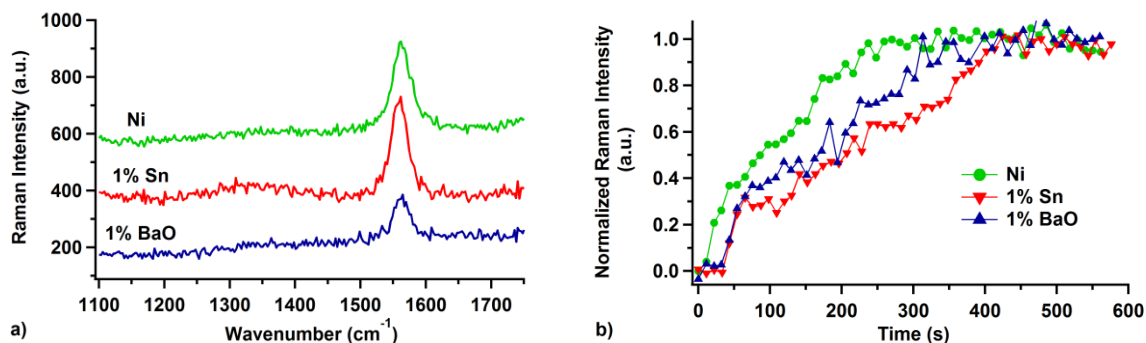


Figure 4.3. (a) Representative Raman spectra acquired from undoped Ni-YSZ and infiltrated Ni-YSZ anodes at the end of the 10 minute CH<sub>4</sub> exposure period. (b) Normalized G peak intensity at 1561 cm<sup>-1</sup> as a function of time during CH<sub>4</sub> exposure showing carbon growth on each anode type.

The rate of carbon growth was determined by plotting the G peak intensity as a function of time (Fig. 4.3b). Due to variations in absolute intensities (of approximately  $\pm 20\%$ ) between experiments, data were normalized to compare carbon growth kinetics directly. For all MEAs, graphite began to accumulate within 1 minute of exposing the anode to CH<sub>4</sub> and the signals reached asymptotic limits after ~8 minutes. The asymptotic limit in the kinetics data for the 1% BaO infiltrated anode is attributed to the amount of deposited carbon reaching a steady state while the kinetics for the undoped and 1% Sn infiltrated anodes are likely limited by the penetration depth of the Raman excitation source. This claim is based on the significantly lower absolute graphite signal observed for the BaO infiltrated samples (Fig. 4.3a). The undoped Ni-YSZ anodes showed rapid carbon growth beginning at ~20 seconds while carbon accumulation on the infiltrated samples was delayed slightly and appeared at 40-50 seconds. These results show that small amounts of the dopants slowed the initial formation of carbon, while BaO also reduced the total amount of carbon that accumulated; notably, the addition of 1% BaO or

1% Sn to Ni-YSZ anodes did not prevent carbon from eventually forming on the anode surface.

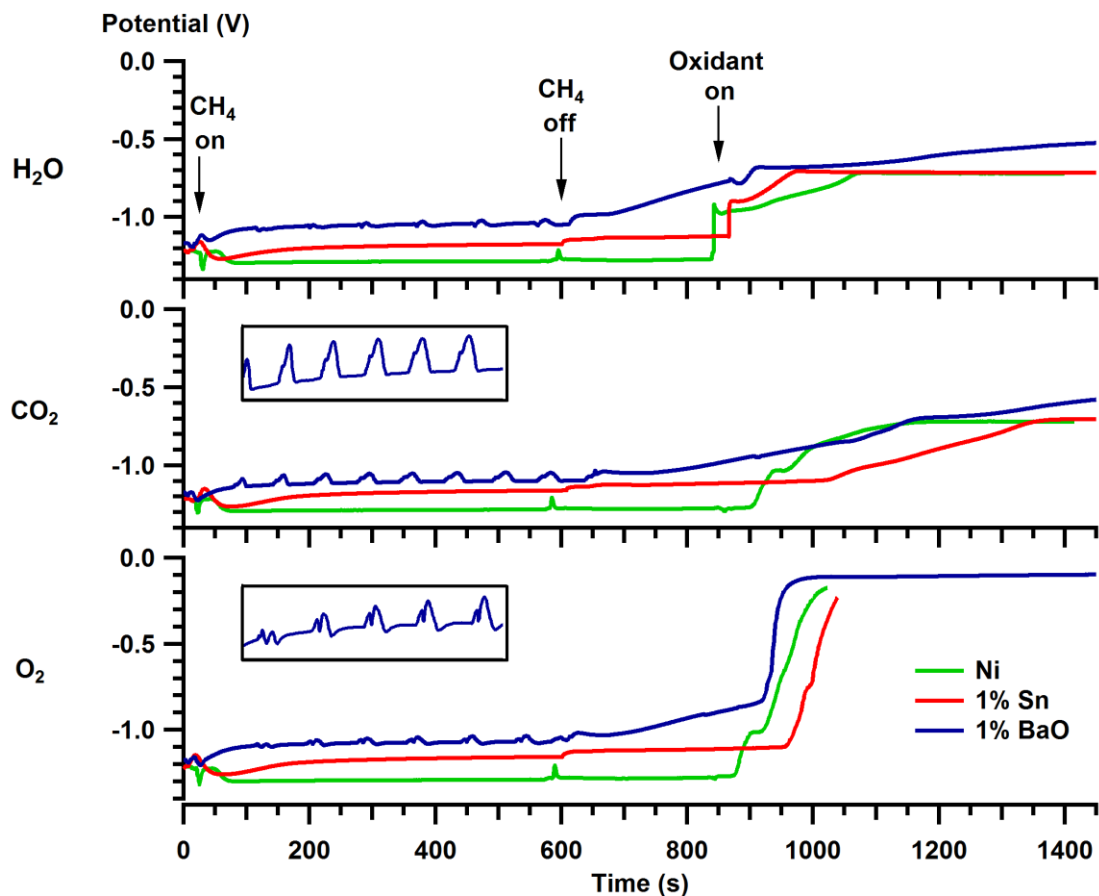


Figure 4.4. Cell potential as a function of time during the carbon formation/removal cycles for the three different cermet anodes held at OCV. The CH<sub>4</sub> fuel was supplied to the anode until ~600 seconds; the anode chamber was then purged with Ar for ~240 seconds; and at ~840 seconds the anode was exposed to the H<sub>2</sub>O (top), CO<sub>2</sub> (middle), and O<sub>2</sub> (bottom) oxidant. The insets show the oscillating behavior observed with the 1% BaO infiltrated anode during CH<sub>4</sub> exposure.

Although the Raman spectra showed that more carbon accumulated on the undoped and Sn infiltrated anodes, the presence of Sn in the anode had a measurable effect on the cell potential relative to the undoped anode. As shown in Figure 4.4, the



OCV of the Ni-YSZ anode exposed to CH<sub>4</sub> was consistently  $-1.28 \pm 0.01$  V, while the values for the 1% Sn and 1% BaO infiltrated anodes were  $-1.17 \pm 0.01$  and  $-1.05 \pm 0.02$  V, respectively. Voltammetry measurements with the 1% BaO infiltrated anode showed very unusual oscillatory behavior in the OCV data during the 10 minute CH<sub>4</sub> exposure (insets in Fig. 4.4). This response was never observed from the same anode exposed to H<sub>2</sub> or the reforming agents, nor was such activity observed with either the undoped Ni-YSZ or the 1% Sn infiltrated anodes. During the first 90 seconds following introduction of CH<sub>4</sub> to the 1% BaO anode, the OCV increased steadily to -1.07 V while the Raman spectra showed measurable, albeit weak, evidence of carbon formation. The cell potential then began to oscillate with a ~70 second period and amplitude of  $\sim \pm 0.04$  V. By the end of the exposure period, the average voltage of these fluctuations began to stabilize to  $-1.05 \pm 0.01$  V.

Discussion. The identical cell potentials for the Ni-YSZ and 1% Sn anodes exposed to H<sub>2</sub> (y-axis intercepts at -1.22 V in Fig. 4.4) imply that the Sn did not participate directly in electrochemical reactions of H<sub>2</sub> at anode's electrochemically active TPB. In contrast, the cell potential for the 1% BaO infiltrated anode exposed to H<sub>2</sub> was measurably different with an OCV that was 0.05 V smaller in magnitude than the measured voltage for the undoped cell. According to the Nernst equation for H<sub>2</sub> oxidation, the smaller cell potential indicates a higher conversion of H<sub>2</sub> to H<sub>2</sub>O<sub>(g)</sub> at the BaO infiltrated anode.<sup>[183]</sup> The higher concentration of H<sub>2</sub>O<sub>(g)</sub> above the BaO infiltrated anode likely arises from the known ability of BaO to promote chemical oxidation of H<sub>2</sub>.<sup>[184]</sup> Similarly, the benchmark LSV and EIS measurements suggest differences in the

surface chemistry between the infiltrated and undoped Ni-YSZ anodes. The lower powers produced by the Sn and BaO infiltrated cells (see Fig. 4.2a and 4.2c) may be attributed to the dopants occupying catalytic sites on the Ni reducing the overall number of catalytic reactions at the anode and/or changes in the anode microstructure.<sup>[48,185]</sup> The increase in  $R_p$  for MEAs with Sn or BaO infiltrated anodes (see Fig. 4.2b and 4.2d) is attributed to decreased catalytic activity at the TPBs and reduced mass transport relative to the MEA with the undoped Ni-YSZ anode. Specifically, the higher  $R_p$  values for the BaO infiltrated cell have been attributed to the dopants occupying catalytic sites on the Ni, reducing electrochemical activity for  $H_2$  oxidation<sup>[47]</sup> and a volume expansion of the anode due to interactions between the YSZ and BaO.<sup>[186]</sup> Changes in anode microstructure can impede gas flow, an effect that would be associated with the increased  $R_p$  and would require additional components to fit the EIS data (Fig. 4.2b). Impedance data coupled with the voltammetry results show clearly that infiltrating the Ni-YSZ cermet anodes adversely impacts electrochemical performance of these electrolyte-supported MEAs operating with  $H_2$ .

During  $CH_4$  exposure at OCV, the Raman spectra showed that graphite formed on all of the anodes with the least amount of carbon accumulating on the BaO infiltrated anodes (Fig. 4.3a). Differences in the measured cell OCV (Fig. 4.4) indicate that carbon accumulation within the infiltrated anodes was not the same as within the undoped Ni-YSZ. Previous studies have shown that as graphite begins to accumulate within the anode, the cell OCV stabilizes within the vicinity of -1.3 V.<sup>[90,128]</sup> Based on these findings, cell potentials close to this value are attributed to carbon accumulation in the

electrochemically active region of the anode, and any significant variations in OCV measurements from this value during CH<sub>4</sub> exposure will arise from additional electrochemical reactions and/or surface reactions that change the partial pressures of species (such as H<sub>2</sub>O, CO<sub>2</sub> and CO) above the anode.<sup>[44,187,188]</sup> Given that these measurements are performed without cell polarization, we assume that changes in gas phase partial pressures arise from Sn or BaO catalyzed surface chemistry.

Raman data from the undoped Ni-YSZ and 1% Sn anodes implied that similar amounts of carbon formed on the surface of each anode. However, CH<sub>4</sub> affected the electrochemical behavior of the 1% Sn infiltrated anodes very differently relative to the undoped Ni-YSZ anode (Fig. 4.4). Unlike the undoped Ni-YSZ anode where changes in OCV indicated carbon accumulation throughout the anode, the OCV for the 1% Sn anode increased (or became less negative) under CH<sub>4</sub>. The fact that the OCV of the 1% Sn anode exposed to CH<sub>4</sub> did not decrease to a value approaching -1.3 V shows that spectroscopically observable carbon did not accumulate within the electrochemically active region. Instead, the cell potential suggested that hydrogen and/or CO oxidation were the relevant half reactions at the TPB.

Earlier studies of Ni-YSZ anodes infiltrated with Sn have proposed that Sn displaces the Ni from carbon nucleation sites lowering carbon binding energy to the catalyst.<sup>[185]</sup> If carbon on these sites is less tightly bound to the surface, carbon that forms near the TPBs will be more susceptible to removal by electrochemical oxidation and surface reforming reactions. Conversely, carbon deposited at locations far from the TPB will be removed only via reactions with the gas phase products or mobile surface species

and will not contribute to the measured cell potential. Given spectroscopic data that clearly show significant carbon accumulation and voltammetry measurements indicating just as clearly that less – if any – deposited carbon is electrochemically accessible, we conclude that the net result of infiltrating a Ni-YSZ anode with Sn still enables carbon growth on the top surface of the anode but inhibits carbon accumulation in the electrochemically active region.

The cyclic behavior of the cell potential for MEAs with 1% BaO is attributed to oscillatory carbon formation/removal on the anode. The oscillating OCV implies that electrochemical reactions at the TPBs and/or gas phase reactant and product partial pressures varied cyclically in the anode chamber. Raman spectra collected during exposure to CH<sub>4</sub> confirmed the presence of carbon on the BaO infiltrated anode but rapid changes in the amount of carbon that might correlate with the oscillating OCV data were not discernible in the spectra.

Several studies have examined the effects of adding BaO to high temperature catalysts in an effort to reduce coking or to promote selective reactions such as the direct decomposition of NO in exhaust systems.<sup>[47,164,165]</sup> BaO islands on the order of 10–100 nm in diameter have been observed on the surface of electrodes infiltrated or coated with BaO following thermal conditioning.<sup>[47,164,167,189]</sup> Experimental and computational studies conducted by Yang *et al.* provide a possible explanation of the role BaO plays mitigating carbon formation on Ni catalysts.<sup>[165]</sup> Based on their proposed mechanism, we can interpret the oscillatory behavior observed in the voltammetry measurements for the MEA with the 1% BaO anodes exposed to CH<sub>4</sub>. After switching the fuel from H<sub>2</sub> to CH<sub>4</sub>,

Ni catalyzes dissociative chemisorption of  $\text{CH}_4$  to produce adsorbed carbon and hydrogen. The hydrogen can react either with surface oxides (such as YSZ) to produce  $\text{H}_2\text{O}$ <sup>[190]</sup> that either desorbs and is carried away in the exhaust or rapidly dissociates on the BaO islands to create a population of surface hydroxides.<sup>[191]</sup> The hydroxyl groups on BaO can then remove carbon that has formed near the dopant-TPBs to create CO and  $\text{H}_2$ . (Here, the term ‘dopant-TPB’ is used to refer to boundaries between the BaO and Ni and the ambient gas phase.) These processes will promote the production of the reaction products CO and  $\text{CO}_2$ , and the measured OCV will increase towards the CO/ $\text{CO}_2$  equilibrium potential at -0.99 V.<sup>[44]</sup> Carbon accumulation will continue on the Ni regions that are far from the BaO structures. If the carbon accumulates far away from the dopant-TPBs of the BaO islands and cannot be oxidized by gas species, then the partial pressure of  $\text{CO}_2$  decreases and the OCV approaches -1.07 V. As more carbon accumulates, the carbon that grows towards the dopant-TPBs can be oxidized resulting in an increase the  $\text{CO}_2$  partial pressure and rise in cell potential. While this proposed sequence is admittedly speculative, the spectroscopic and voltammetry data reported above coupled with the computational efforts of Yang, *et al.* provide an internally consistent description of experimental observations and raise important questions about the role of adsorbate surface mobility in these complex catalytic systems.

### Carbon Removal with Reforming Agents

Results. Following exposure to  $\text{CH}_4$ , the anode chamber was purged with Ar for 240 seconds to remove any residual fuel before a reforming agent was introduced. The

cell OCV increased for all of the anodes after switching off the supply of  $\text{CH}_4$  (Fig. 4.4). For the undoped cell, the OCV changed by 0.01-0.04 V while the OCV for the Sn- and BaO-infiltrated anodes rose by 0.04-0.06 V and 0.09-0.35 V, respectively. Although this changing OCV under Ar implied continued chemistry in the electrochemically active region, Raman spectroscopy confirmed that graphite remained on the top surface of each anode.

Similar to previous studies,<sup>[135]</sup> experiments presented in this work found that  $\text{H}_2\text{O}$  and  $\text{CO}_2$  removed carbon and only partially oxidized Ni in the anode while  $\text{O}_2$  oxidized both the deposited carbon and the Ni anode itself. Representative Raman spectra collected from the undoped Ni-YSZ during exposure to  $\text{O}_2$  are presented in Figure 4.5. Raman kinetics data showing rates of carbon removal and NiO formation are shown in Figure 4.6 for Ni-YSZ and both the Sn and BaO infiltrated anodes. Data have been normalized with respect to the maximum signal intensities to allow for direct comparisons between each anode/reforming agent combination. Low Raman intensities observed for the 1% BaO sample exposed to  $\text{H}_2\text{O}$  and  $\text{CO}_2$  led to large fluctuations in the normalized kinetics spectra. The removal of carbon from the anode is defined to be complete when the normalized Raman G peak intensity drops to the baseline (average normalized Raman intensity  $\sim 0.1$ ) while the appearance of NiO is defined by the time corresponding to a normalized Raman intensity above the baseline with all subsequent data points increasing in intensity.

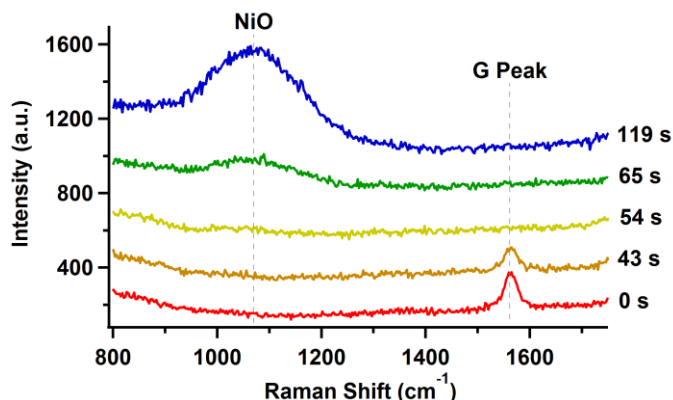


Figure 4.5. Raman spectra collected undoped Ni-YSZ prior ( $t = 0$  s) and during ( $t > 0$  s)  $O_2$  exposure at 730 °C showing the removal of carbon (G peak at  $1561\text{ cm}^{-1}$ ) and formation of NiO (broad peak at  $1070\text{ cm}^{-1}$ ). Spectra have been offset in the y-axis for clarity.

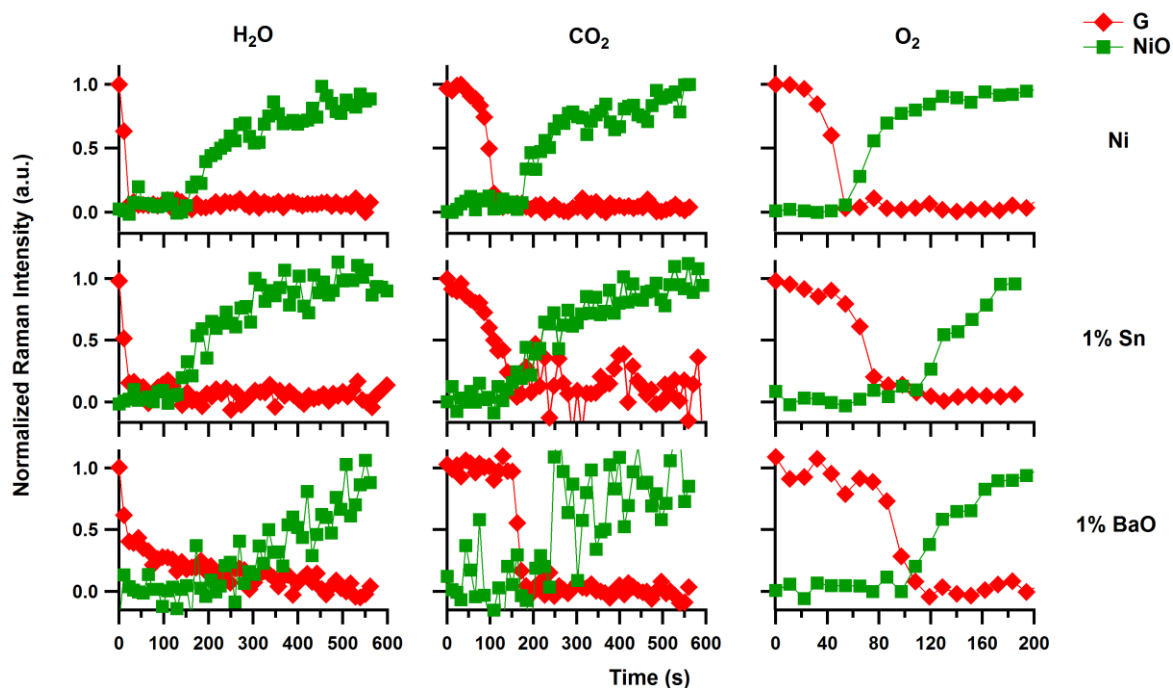


Figure 4.6. Raman kinetics data acquired during the introduction of the reforming agents (at  $\sim 5$  seconds) where the top, middle and bottom rows correspond to spectra collected from the Ni-YSZ, 1% Sn and 1% BaO infiltrated anodes, respectively, and the columns correspond to cycles for a given reforming agent. The oxidation of carbon and Ni correspond to a decrease in G peak intensity at  $1561\text{ cm}^{-1}$  (red diamonds) and an increase in NiO signal at  $1070\text{ cm}^{-1}$  (green squares). Note that in the plots above,  $t = 0$  s corresponds to  $t \sim 840$  s in Figure 4.4.

Table 4.2. Reforming agent oxidation data for each MEA experiment.

Reforming agent	C <sub>(s)</sub> oxidation time (s) <sup>a</sup> [sample size] <sup>d</sup>	Ni oxidation time (s) <sup>a</sup> [sample size] <sup>d</sup>	Raman $\Delta t_{\text{lapse time}}$ (s) <sup>b</sup>	Potential $\Delta t_{\text{lapse time}}$ (s) <sup>c</sup> [sample size] <sup>e</sup>
Ni-YSZ				
H <sub>2</sub> O	20 [6]	160 [2]	140	13 ± 4 [2]
CO <sub>2</sub>	120 [2]	180 [2]	60	52 ± 3 [4]
O <sub>2</sub>	60 [2]	60 [2]	0	31 ± 7 [4]
1% Sn-Ni-YSZ				
H <sub>2</sub> O	20 [6]	140 [3]	120	24 ± 6 [4]
CO <sub>2</sub>	130 [4]	170 [2]	40	110 ± 5 [2]
O <sub>2</sub>	100 [3]	100 [2]	0	48 ± 0 [1]
1% BaO-Ni-YSZ				
H <sub>2</sub> O	40 & 240* [3]	290 [1]	250 & 50*	19 ± 1 [2]
CO <sub>2</sub>	180 [4]	260 [2]	80	100 ± 18 [2]
O <sub>2</sub>	110 [3]	110 [3]	0	74 ± 17 [3]

<sup>a</sup>Uncertainties are ± 10 s (limited by spectra acquisition times) unless stated otherwise.

<sup>b</sup>Period of time difference between loss of graphitic G peak signal and appearance of NiO signal. <sup>c</sup>Period of time between introducing the oxidizing agent and the rapid change in cell potential. <sup>d</sup>Sample size for spectroscopic observations include data from both full MEAs (with cathodes) and ‘chips’ that have only the anode attached to the electrolyte.

<sup>e</sup>Sample size for electrochemical measurements report only measurements from complete MEAs. \*Approximately 65% reduction of the graphite Raman signal occurred within 40 s proceeded by a slower decrease in the remaining G peak intensity.

Raman spectroscopy measurements verified that the removal of carbon preceded the formation of NiO for all of the reforming agents. As shown in Figure 4.6, the rate of carbon removal was slower for the Sn infiltrated anode exposed to O<sub>2</sub> while the rate of carbon removal on the BaO infiltrated anode was slowest for the all of the reforming agents. Carbon oxidation rates shared some similarities for all of the anodes with H<sub>2</sub>O being the most efficient reforming agent that rapidly removed a majority or all of the carbon from the anode surface within the first 40 seconds of exposure and CO<sub>2</sub> being the least efficient reforming agent (Table 4.2). Correlations between the spectroscopic and



voltammetry recorded during exposure to each reforming agent are discussed in detail below. A summary of the carbon and Ni oxidation kinetics data is presented in Table 4.2.

The Raman kinetics data show that within 20 seconds of switching on the H<sub>2</sub>O, all observable carbon was removed from both the undoped and Sn infiltrated Ni-YSZ electrodes (Fig. 4.6 and Table 4.2). The decrease in the graphite signal was accompanied by a steep increase in cell potential and after ~120 seconds of H<sub>2</sub>O exposure, the OCV reached an asymptotic limit of  $-0.72 \pm 0.01$  V (Fig. 4.4). Shortly after the cell OCV reached this limit, Raman spectra showed evidence of NiO formation. When exposed to H<sub>2</sub>O, the MEA with 1% BaO exhibited an initial, steep decrease in the amount of graphite, but even after 40 seconds some graphite signal persisted. This remaining graphite disappeared more slowly. Following the loss in graphite signal, the NiO feature appeared at ~240 seconds and the OCV continued to increase above -0.72 V. Comparing these results shows that oxidation reactions associated with the H<sub>2</sub>O reforming agent were similar for the undoped and Sn infiltrated anodes, while kinetics for BaO infiltrated anode were more complicated and included a slower carbon removal step.

As a reforming agent, CO<sub>2</sub> was the slowest to remove carbon with average removal times of 120, 130 and 180 seconds for the undoped, 1% Sn and 1% BaO infiltrated samples, respectively (Table 4.2). Similar to the cell potentials with H<sub>2</sub>O, the cell OCV during exposure to CO<sub>2</sub> approached -0.99 V as the graphitic G peak in the Raman spectra disappeared. After the graphite feature had disappeared from the Raman spectra, the cell OCV began to increase as the CO<sub>2</sub> began to oxidize Ni. The NiO feature appeared in the Raman spectra at 180 and 170 seconds after the start of CO<sub>2</sub> exposure for

the undoped and Sn infiltrated anodes, respectively, but was delayed until 250 seconds for the BaO infiltrated anode (Fig. 4.6). In addition to slower kinetics, the spectroscopic signal associated with NiO for the BaO samples had a low intensity that continuously increased over the 10 minute exposure period to CO<sub>2</sub>. Repeated efforts to find evidence of BaCO<sub>3</sub> formation<sup>[192]</sup> were unsuccessful, likely due to the relatively small amount of BaO present in the anode.

Carbon removal with O<sub>2</sub> took almost twice as long on the infiltrated anodes compared to the undoped anode (Table 4.2). Spectra from the different anodes exposed to O<sub>2</sub> show that NiO formation occurred almost immediately after the graphite Raman signal had disappeared (Fig. 4.6). For the Sn-infiltrated anodes, NiO appeared simultaneously with the disappearance of graphite although the measured OCV was slower to change. Carbon removal from the BaO anode exposed to O<sub>2</sub> was accompanied by a gradual increase in OCV. As the carbon signature disappeared from the Raman spectra, the NiO feature began to grow and the OCV rose rapidly and approached an asymptotic limit of -0.1 V. Since repeated redox cycling of SOFCs leads to irreversible damage to the cell,<sup>[193]</sup> many of the O<sub>2</sub> exposure cycles were conducted for only 3 minutes; however, near the end of an experiment, exposure to O<sub>2</sub> was extended for a full 10 minutes.

Discussion. During the Ar purge, changing Raman intensities and OCV implied that surface reactions continued to occur. As noted in the Experimental Methods above, numerous benchmark measurements were performed at the start of an experiment and between cycles to test for the presence/development of leaks between the cathode and

anode. No evidence of leaks was observed. Following carbon formation, the small change in OCV for the undoped anode during the purge period suggests that its electrochemical behavior remained dominated by the carbon deposits in the electrochemically active region. During the Ar purge, the OCV for the Sn infiltrated anode gradually increased and approached the standard reduction potential associated with the CO/CO<sub>2</sub> equilibrium. The BaO infiltrated anode exhibited an increase in OCV approaching the Ni/NiO equilibrium potential (at  $\sim -0.73$  V)<sup>[49]</sup> indicating that Ni oxidation was already likely starting to occur in the electrochemically active region.

Changes in the kinetics data brought about by infiltrating the anodes with either Sn or BaO may arise from several mechanisms: (1) the dopants occupy catalytic sites on Ni, slowing surface reactions at the anode relative to the undoped anode; (2) the presence of the dopants changes the binding energy of the carbon to the Ni catalyst; and/or (3) the dopants participate directly in reactions with the H<sub>2</sub>O, CO<sub>2</sub> and O<sub>2</sub>.

If Sn and BaO acted as spectators and did not directly influence surface chemistry, dopants located on the Ni surface would reduce the number of catalytic sites available to promote oxidation reactions between the reforming agent and graphite.<sup>[185]</sup> Such a ‘mechanical’ argument would predict that graphite removal from the Sn and BaO infiltrated anode should be slower than for the undoped samples. This conclusion is supported generally by Raman spectra (Fig. 4.6) that showed carbon removal from the infiltrated anodes required similar or longer times than from the undoped MEA.

The second proposed mechanism considers changes in the binding energy between the adsorbed species and the Ni surface.<sup>[185]</sup> In this model the increased bond

strength between the Ni substrate and adsorbed species would lead to consistently longer times for carbon removal and Ni oxidation. Table 4.2 shows with H<sub>2</sub>O and CO<sub>2</sub>, the undoped and Sn-infiltrated anodes behave similarly but that carbon removal and Ni oxidation on the BaO infiltrated anode requires considerably more time. With O<sub>2</sub> as the reforming agent, carbon removal and Ni oxidation take more time with *both* infiltrated anodes than for the undoped Ni-YSZ anode. This pattern of reactivity is inconsistent with models that attribute changes in surface reaction kinetics with changes in binding energy between the deposited carbon and Ni surface. We note, however, that this conclusion may not apply in the limit where the 2° material is present in higher concentrations and can more directly mediate carbon adhesion to the anode.

Finally, the third proposed mechanism involves reactions between the dopant and the reforming agent. Previously reported findings from Kirtley *et al.*<sup>[135]</sup> attributed the relative efficacy of H<sub>2</sub>O, O<sub>2</sub> and CO<sub>2</sub> in removing carbon from (non-infiltrated) Ni-YSZ cermet anodes to the ability of the anode to promote formation of surface oxygen species. This step is predicted to be fastest with H<sub>2</sub>O and slowest with CO<sub>2</sub>.<sup>[100]</sup> If dopants can compete with accumulated carbon to react with surface oxygen created by chemisorption of a reforming agent, then the rate of carbon removal will be slowed. This prediction is largely supported by the data in Table 4.2 with one exception: carbon removal by H<sub>2</sub>O from the BaO infiltrated anode shows two distinct steps, one fast (and consistent with the undoped and Sn-infiltrated anodes) and a second, slower process that requires ~4 minutes to remove the remaining carbon deposits.

To better understand these observations, specific reactions between the dopant species and reforming agents must be considered. All of the reforming agents can react with the Sn to produce  $\text{SnO}_2$  <sup>[194,195]</sup> while the oxidized BaO species ( $\text{Ba(OH)}_2$ ,  $\text{BaO}_2$ , and  $\text{BaCO}_3$ ) is dependent on the gas. <sup>[196-198]</sup> Formation of these oxidized dopants will slow the carbon oxidation kinetics if the reforming agent readily reacts with the dopant. For example when the Sn infiltrated anode is exposed to  $\text{O}_2$ , not all of the  $\text{O}_2$  that reaches the anode will oxidize carbon immediately since a portion of the  $\text{O}_2$  is consumed by Sn oxidation. After the Sn has been completely oxidized, all of the  $\text{O}_2$  that reaches the anode will then oxidize the remaining carbon. This condition permits continued formation of NiO unhindered by the dopant, and the elapsed time between when the graphitic G peak disappears and the NiO signal begins to grow will be similar to the undoped sample. The experimental results in Table 4.2 show that carbon removal requires longer times for the Sn and Ba-infiltrated anodes but that Ni oxidation immediately follows carbon removal ( $\Delta t_{\text{lapse time}} = 0$  seconds) for all three anodes.

The kinetic traces in Figure 4.6 indicate that two different mechanisms are responsible for removal of graphite from BaO infiltrated anodes by steam as evident by the two distinct rates of carbon removal where the G peak loses intensity abruptly during the first 40 seconds of exposure and then more gradually during the next ~200 seconds. These data are markedly different from steam-driven graphite removal from the undoped and 1% Sn anodes where the graphite intensity observed in the Raman spectra drops to baseline within 30 seconds. These two different rates of graphite removal from the 1% BaO infiltrated anodes are assigned to different heterogeneous surface processes. Since

the OCV data in Figure 4.4 establish that accumulated carbon is not present in the electrochemically active TPB region of the anode, graphite oxidation could not be observed directly through voltammetry measurements. The slow decrease in deposited carbon that began after 40 seconds may be a consequence of the surface reaction kinetics in the presence of  $\text{Ba}(\text{OH})_2$ . More studies are needed to explore the possible role of  $\text{Ba}(\text{OH})_2$  and are beyond the scope of this paper. Additionally, changes in the NiO kinetics indicate that Ni oxidation mechanisms associated with the BaO infiltrated anodes exposed to  $\text{H}_2\text{O}$  are not the same as the Ni oxidation in the other anodes. The elapsed time between the disappearance of the spectroscopic G peak and the appearance of the NiO feature was approximately half the time for the undoped and Sn infiltrated anodes.

### Conclusions

The effects of Sn and BaO (1% by mass) added Ni-YSZ SOFC cermet anodes were investigated by performing *in situ* Raman spectroscopy coupled with voltammetry measurements at OCV. The spectroscopic data revealed that highly ordered graphite formed on the top surface of all of anodes exposed to  $\text{CH}_4$  while the measured cell potentials strongly implied a heterogeneous distribution of carbon throughout the anode microstructure. Raman spectra collected on anodes infiltrated with 1% Sn had graphite G peak intensities similar to those of the undoped MEAs, but OCV data indicated that carbon did not accumulate in the Sn-doped electrochemically active region suggesting that Sn-driven reforming of methane changed the fuel composition near the electrolyte-anode interface. The amount of carbon that formed on MEAs with 1% BaO was

noticeably less than on the 1% Sn infiltrated anodes, as evidenced by the lower intensity Raman signal. Interestingly, the OCV for the BaO infiltrated anodes exhibited a cyclic behavior during exposure to  $\text{CH}_4$ . This phenomenon is attributed to the oscillatory formation and removal of carbon within the anode microstructure catalyzed by the Ba/BaO dopant. Vibrational spectra recorded during the Ar purge verified that graphite remained on the anode in the absence of a gas phase fuel although oxidation of the deposited carbon continued to occur. The pronounced increase in OCV during the Ar purge of the BaO infiltrated anodes compared to the undoped and Sn samples emphasized the dynamic role BaO plays in the removal of carbon from the Ni catalyst.

In addition to carbon formation, the ability of reforming agents to remove graphite from each anode type was examined. The graphite oxidization was most rapid for  $\text{H}_2\text{O}$  followed by  $\text{O}_2$  and then  $\text{CO}_2$  on the undoped and Sn infiltrated anodes. On the BaO infiltrated anode, carbon removal by  $\text{H}_2\text{O}$  showed evidence of two distinct mechanisms while removal of carbon by  $\text{O}_2$  and  $\text{CO}_2$  followed patterns similar to the Sn-infiltrated and undoped anodes.

Several important findings emerged from this work:

- While the Ni-YSZ and Sn infiltrated anode surfaces showed similar susceptibilities to carbon deposition, the electrochemically active interface between the electrode and electrolyte appeared to remain carbon-free for the Sn infiltrated anode but carbon accumulated throughout the undoped anode.
- BaO inhibited carbon deposition throughout the anode with less carbon present both in the electrochemically active region *and* on the anode's top surface.

- Of the three reforming agents used to remove carbon from the anodes, steam was the most efficient and  $\text{CO}_2$  required the longest time.  $\text{O}_2$  required slightly longer exposure to remove deposited carbon, but then oxidized the anode completely. Steam and  $\text{CO}_2$  only partially oxidized the anode, establishing equilibrium distributions of Ni and NiO on the undoped and Sn infiltrated anodes over a 10 minute exposure period. The BaO infiltrated anodes, however, showed strong evidence of continued Ni oxidation under steam and  $\text{CO}_2$  suggesting that BaO can destabilize anode microstructure and reduce electrochemical conversion efficiency.

Taken together, these results showed that both Sn and BaO were effective at keeping carbon from accumulating in the electrochemically active regions of an SOFC anode during limited exposure to methane. Sn, however, was unable to suppress carbon deposition on the top surface of the anode and BaO was moderately effective in this capacity. This paradox – carbon on the anode surface but not in the electrochemically active region – implies large variations in heterogeneous surface chemistry throughout the porous anode structure.

#### Acknowledgements

This work was supported by grants from the United States Office of Naval Research (N000141010954, N000141210199, and N000141410326) and an NSERC Solid Oxide Fuel Cell Canada Strategic Research Network from the Natural Science and Engineering Research Council (NSERC).



## CHAPTER FIVE

*IN SITU* FORMATION OF MULTIFUNCTIONAL CERAMICS: MIXED ION-ELECTRON CONDUCTING PROPERTIES OF ZIRCONIUM TITANIUM OXIDESContribution of Authors and Co-Authors

Manuscript in Chapter 5

Author: Melissa D. McIntyre

Contributions: Aided in the preparation of  $\text{ZrO}_2\text{-TiO}_2$  reaction samples. Prepared samples and performed Raman spectroscopy and electrochemical measurements on the samples. Analyzed data, generated figures, and wrote the manuscript in preparation for publication.

Co-Author: David R. Driscoll

Contributions: Prepared  $\text{ZrO}_2\text{-TiO}_2$  reaction samples. Acquired and analyzed XRD spectra. Aided in the preparation of the materials fabrication and XRD sections in the manuscript.

Co-Author: Märtha M. Welander

Contributions: Aided in the acquisition of Raman spectra on samples. Edited/commented on the manuscript.

Co-Author: Josh B. Sinrud

Contributions: Prepared  $\text{Zr}_5\text{Ti}_7\text{O}_{24}$  symmetric cell and performed Arrhenius analysis. Aided in the preparation of the activation energies section of the manuscript.

Co-Author: Stephen W. Sofie

Contributions: Provided important insight into performing experiments and interpreting the defect chemistry and results. Aided in the preparation of the manuscript.

Co-Author: Robert A. Walker

Contributions: Provided important insight into performing experiments and interpreting results. Aided in the preparation of the manuscript and figures.

Manuscript Information Page

Melissa D. McIntyre, David R. Driscoll, Märtha M. Welander, Josh B. Sinrud, Stephen W. Sofie, Robert A. Walker

The Journal of Materials Chemistry A

Status of Manuscript:

☒ Prepared for submission to a peer-reviewed journal

☐ Officially submitted to a peer-review journal

☐ Accepted by a peer-reviewed journal

☐ Published in a peer-reviewed journal

Publication anticipated by the Royal Society of Chemistry

*IN SITU* FORMATION OF MULTIFUNCTIONAL CERAMICS: MIXED ION-ELECTRON CONDUCTING PROPERTIES OF ZIRCONIUM TITANIUM OXIDES

M. D. McIntyre<sup>†</sup>, D. R. Driscoll<sup>‡</sup>, M. M. Welander<sup>†</sup>, J. B. Sinrud<sup>†</sup>, S. W. Sofie<sup>‡</sup>,  
R. A. Walker<sup>†</sup>

<sup>†</sup>Department of Chemistry and Biochemistry, Montana State University, Bozeman,  
Montana 59717, USA

<sup>‡</sup>Department of Mechanical and Industrial Engineering, Montana State University,  
Bozeman, Montana 59717, USA

Abstract

XRD and Raman spectroscopy are used to investigate the formation of functional zirconium titanate secondary phases in Ti/Zr oxides. Different zirconia polymorphs (either pure or stabilized with small amounts of yttria (YSZ)) mechanically mixed with TiO<sub>2</sub> and heated above 1000 °C in stagnant air react to form several secondary phases. For sintering temperatures > 1100 °C, mixtures of TiO<sub>2</sub> and *m*-ZrO<sub>2</sub> form a ZrTiO<sub>4</sub> secondary phase while mixtures of TiO<sub>2</sub> and 3YSZ or 8YSZ form Zr<sub>5</sub>Ti<sub>7</sub>O<sub>24</sub>. The extent of secondary phase formation is enhanced with both higher sintering temperature and yttria content. The Zr<sub>5</sub>Ti<sub>7</sub>O<sub>24</sub> secondary phase formed from TiO<sub>2</sub>/8YSZ samples sintered at 1400 °C exhibits unexpected mixed ionic and electronic conductivity at 800 °C. These findings suggest that secondary phases intentionally integrated into electrode architectures can improve the performance of high temperature electrocatalyst systems.

### Introduction

Infiltrating porous electrodes with solution phase precursors is a strategy employed to improve performance, catalytic activity and longevity in high temperature electrochemical devices.<sup>[199-205]</sup> For example, traditional Ni yttria-stabilized zirconia (Ni-YSZ) cermet anodes used in solid oxide fuel cells (SOFCs) are susceptible to carbon accumulation and to sulfur poisoning.<sup>[206]</sup> To counter the effects of degradation, anodes have been infiltrated with secondary materials containing Sn, Ba, Al and a host of other constituents, typically at levels of 1-5% (by mass).<sup>[129,153,169,207-210]</sup> Processing and preparing infiltrated electrodes, however, can lead to formation of new material phases that affect surface chemistry and electrode microstructure in unexpected ways. Findings reported below show how thermally treating mixtures of YSZ and TiO<sub>2</sub> leads to the formation of a Zr<sub>5</sub>Ti<sub>7</sub>O<sub>24</sub> superstructure that has mixed ion-electron conducting (MIEC) properties. This discovery resolves questions about how TiO<sub>2</sub> enhances SOFC anode performance.<sup>[203,211-213]</sup> More importantly, *in situ* formation of this MIEC phase shows how strategic modification of anode composition can create multi-functional secondary phases that confer advantageous electrochemical behavior to high temperature solid-state electrodes.

Materials having MIEC properties are attractive for high temperature electrochemical applications including solid oxide electrolysis cells (SOECs) and SOFCs.<sup>[6,214]</sup> In most solid oxide-based energy conversion systems, electrochemical oxidation and reduction occurs at the putative three-phase boundary – a junction where the ionically conducting solid oxide electrolyte, the electronically conducting electrode

and the gas phase atmosphere converge. MIECs expand the 1-dimensional, three-phase boundary by enabling electrochemical reactions to occur across the entire electrocatalytic surface.<sup>[215,216]</sup> Common MIECs include gadolinium doped ceria (GDC), samarium doped ceria (SDC), calcium doped lanthanum ferrites, and a host of other perovskite materials.<sup>[23,217-220]</sup> These materials have been employed as electrolytes and electrodes in intermediate temperature (500-700 °C) SOEC/SOFC applications. They have also found application as functional layers between ion conducting electrolytes and electronically conducting electrodes. Despite their advantages in electrocatalytic systems, however, MIECs do have limitations, particularly when used as electrolytes. In these cases, non-negligible oxygen partial pressure above the MIEC adversely affects the measured Nernst potential and limits sustainable open circuit voltages (OCVs).<sup>[221-223]</sup> This internal short circuiting restricts the usage of MIEC electrolytes in SOEC/SOFCs and requires incorporating additional purely ion conducting materials into the electrolyte, such as zirconia-based ceramics.<sup>[224]</sup>

Zirconia-based electrolytes are commonly employed in SOFCs and SOECs due to their chemical and thermal stability under oxidizing and reducing conditions at elevated temperatures. At temperatures below ~1170 °C, zirconia is stable in its monoclinic phase (*m*-ZrO<sub>2</sub>) and is both an electronic and ionic insulator.<sup>[225]</sup> Doping zirconia with rare earth oxides such as Y<sub>2</sub>O<sub>3</sub> (yttria-stabilized zirconia or YSZ) and Sc<sub>2</sub>O<sub>3</sub> (scandia-stabilized zirconia or ScSZ) stabilizes the ZrO<sub>2</sub> cubic phase (*c*-ZrO<sub>2</sub>) and confers ionic conductivity to the resulting material.<sup>[28,34]</sup> ScSZ electrolytes exhibit higher ionic conductivity than YSZ, but long term exposure at temperatures above 600 °C induces

decomposition of ScSZ's cubic phase and reduces ionic conductivity.<sup>[226,227]</sup> Consequently, YSZ electrolytes are typically used in SOFCs operating at 600-1000 °C.

In experiments described below, TiO<sub>2</sub> was added to YSZ and the resulting changes in structure and electrochemical properties were studied. Motivating this work were previous findings that have reported enhanced SOFC performance with TiO<sub>2</sub> doped Ni-YSZ anodes.<sup>[211,212,228-230]</sup> The origin(s) of these effects is not fully understood due to the complexity of the ZrO<sub>2</sub>-TiO<sub>2</sub> phase diagram, the addition of rare earth stabilizing dopants, and the multitude of stable and meta-stable forms of zirconia, zirconium titanate, and pyrochlore structures reported in the literature.<sup>[231]</sup> Of particular interest for solid oxide electrochemical devices are two closely related stoichiometric materials that have orthorhombic  $\alpha$ -PbO<sub>2</sub> type structures: ZrTiO<sub>4</sub> and Zr<sub>5</sub>Ti<sub>7</sub>O<sub>24</sub>. Although the cation-disordered structure, ZrTiO<sub>4</sub>, is the dominant phase at higher temperatures (T > 1100 °C), the ordered Zr<sub>5</sub>Ti<sub>7</sub>O<sub>24</sub> structure is stable at lower temperatures (T < 1200 °C) and forms readily in the presence of Y<sub>2</sub>O<sub>3</sub>.<sup>[232-235]</sup> Published works by Christoffersen and Azough *et al.* have shown that Y<sub>2</sub>O<sub>3</sub> promotes cation ordering and stabilizes the low temperature zirconium titanate superstructure.<sup>[236,237]</sup> Given that Y<sub>2</sub>O<sub>3</sub> is commonly used to stabilize the cubic, ion conducting phase of zirconia, the consequences of yttrium substituted zirconium titanate secondary phases on an electrode's electrochemical properties should be considered when evaluating performance in SOFCs and SOECs.

The presented studies consider explicitly conditions that promote Zr<sub>5</sub>Ti<sub>7</sub>O<sub>24</sub> formation and the effects that small, non-percolating quantities of this material can have on the performance of cermet electrochemical electrodes. In order to identify the specific

Zr/Ti stoichiometry of secondary phases that form during fabrication of  $\text{TiO}_2$  containing, zirconia-based electrodes, experiments were designed to explore material composition and structure as a function of sintering temperature using *ex situ* XRD and vibrational Raman spectroscopy. Reactions with the monoclinic phase were investigated with pure  $m\text{-ZrO}_2$  while partially stabilized zirconia with 3 mol%  $\text{Y}_2\text{O}_3$  (3YSZ) and fully stabilized zirconia with 8 mol%  $\text{Y}_2\text{O}_3$  (8YSZ) were used to examine reactions of  $\text{TiO}_2$  with the tetragonal ( $t\text{-ZrO}_2$ ) and  $c\text{-ZrO}_2$  phases. The  $m\text{-ZrO}_2$ ,  $t\text{-ZrO}_2$  and  $c\text{-ZrO}_2$  phases in samples that contain  $\text{Y}_2\text{O}_3$  will be referred to as  $m\text{-YSZ}$ ,  $t\text{-YSZ}$  and  $c\text{-YSZ}$  to distinguish them from phases observed in samples that do not contain  $\text{Y}_2\text{O}_3$ . To assess the electrochemical properties of  $\text{Zr}_5\text{Ti}_7\text{O}_{24}$ , this material was used as an electrolyte in a symmetric membrane electrode assembly and the device was characterized using voltammetry and electrochemical impedance measurements. The cell was able to sustain only a low open circuit voltage implying appreciable electronic conductivity. Furthermore, the cell showed a characteristic impedance response consistent with the behavior of ion conducting materials. Additional impedance measurements were used to calculate ionic and electronic conduction activation energies. These latter quantities compared favorably to those of other known MIEC materials.

### Experimental Methods

#### $\text{ZrO}_2\text{-TiO}_2$ Reactions Sample Fabrication

Powders for the  $\text{ZrO}_2\text{-TiO}_2$  reaction study were prepared with the solid-state reaction method by mixing commercially available powders of yttria-stabilized zirconia

(8Y and 3Y grades, Tosoh) or pure zirconia ( $\text{ZrO}_2$ , 40N-0801, Advanced Materials) with titania ( $\text{TiO}_2$ , 22N-0801A, Advanced Materials). Combinations of 8YSZ/ $\text{TiO}_2$ , 3YSZ/ $\text{TiO}_2$ , and  $\text{ZrO}_2$ / $\text{TiO}_2$  were all prepared in a 1 mol Zr : 1 mol Ti ratio in anticipation of  $\text{ZrTiO}_4$  formation based off of the work by Law *et al.*<sup>[228]</sup> These mixtures were ball-milled in an aqueous suspension for 24 hours before being flash frozen and lyophilization. Powder mixtures were then pressed as 3 g pellets in a 1.9 cm (0.75 in) diameter die at 250 MPa. The pellets were sintered at 1100 °C, 1200 °C, 1300 °C or 1400 °C with 5 °C/min ramp rates and 5 hour dwell times.

#### X-ray Powder Diffraction

Following heat treatment, the pellets were ground into powder with a Diamonite mortar and pestle. Sample composition was characterized using Cu K $\alpha$  radiation with a SCINTAG X1 diffraction system. XRD data were collected from 2 $\theta$  26-37°. Materials were identified in the XRD data with the corresponding JCPDS card numbers:  $\text{TiO}_2$  (97-000-9161), *m*- $\text{ZrO}_2$  (97-005-7157), *t*- $\text{ZrO}_2$  (97-009-3126), YSZ (97-009-0885),  $\text{ZrTiO}_4$  (97-002-7311) and  $\text{Zr}_5\text{Ti}_7\text{O}_{24}$  (97-020-1961).

#### Raman Spectroscopy

Vibrational spectra were acquired with a Renishaw InVia spectrometer and 488 nm Ar-ion laser excitation source. A 180° backscattering geometry was used to collect the Stokes-scattered light and Rayleigh scattered light was removed with an edge filter (~150  $\text{cm}^{-1}$  cutoff). Room and high temperature Raman spectra were acquired with



50x and 10x objectives, respectively. Each Raman spectrum was recorded with a 10 second exposure time over the spectral range up to  $3200\text{ cm}^{-1}$ .

#### Electrochemical Evaluation of $\text{Zr}_5\text{Ti}_7\text{O}_{24}$

The electronic and ionic conductivity of  $\text{Zr}_5\text{Ti}_7\text{O}_{24}$  was evaluated at  $800\text{ }^\circ\text{C}$  using a symmetric cell comprised of a  $\sim 640\text{ }\mu\text{m}$  thick  $\text{Zr}_5\text{Ti}_7\text{O}_{24}$  electrolyte (1:1 molar ratio of  $\text{TiO}_2$ :8YSZ sintered at  $1400\text{ }^\circ\text{C}$ ) with platinum electrodes. The Pt- $\text{Zr}_5\text{Ti}_7\text{O}_{24}$ -Pt cell was secured to an alumina tube with alumina paste (Ceramabond 522-VFG, Aremco), which created a gas-tight barrier between each electrode's gas atmosphere. This assembly was then placed in a quartz tube and positioned in the tube furnace of a custom-made high temperature Raman spectroscopy setup that is described in more detail in previous publications.<sup>[126,238]</sup> The cell was heated to  $800 \pm 5\text{ }^\circ\text{C}$  at a ramp rate  $< 1\text{ }^\circ\text{C}/\text{min}$ . The oxidizing and reducing electrodes were then exposed to  $200\text{ mL}/\text{min}$  of 50/50  $\text{H}_2/\text{Ar}$  gas and  $85\text{ mL}/\text{min}$  of air, respectively. Electrochemical measurements were performed with a Princeton Applied Research VersaStat MC. Electrochemical impedance spectroscopy (EIS) data were recorded over the frequency range from  $100,000\text{--}0.1\text{ Hz}$  with  $10\text{ mV rms}$  amplitude. Cell power was calculated from linear sweep voltammetry (LSV) data measured from open circuit voltage (OCV) to maximum current (corresponding to a cell potential of  $0.0\text{ V}$ ) with a  $0.1\text{ V/s}$  scan rate. A box smooth algorithm was applied to the presented LSV data to reduce high frequency electronic interference from the resistive heating furnace that was used to heat the symmetric cell to  $800\text{ }^\circ\text{C}$ .

Ionic and electronic activation energies were determined from an Arrhenius analysis of the complex impedance data.<sup>[70,239,240]</sup> In order to separate the ionic from the

electronic contributions, additional EIS experiments were performed on a symmetric cell with a  $\text{Zr}_5\text{Ti}_7\text{O}_{24}$  membrane between two ionically blocking, symmetric Au electrodes. The electrodes were exposed to 100 ml/min of dry air (laboratory cylinder grade D air). Impedance measurements were performed at OCV over a frequency range from 1,000,000-0.1 Hz with both 10 mV and 100 mV rms amplitudes. Data were acquired in  $\sim 50^\circ\text{C}$  increments from  $650^\circ\text{C}$  to  $800^\circ\text{C}$ . Additional details about the equivalent circuit used to fit the data appear in the following section.

### Results and Discussion

Experiments were designed to identify how secondary phase formation improves the multifunctional behavior of doped, YSZ-based materials commonly used in high temperature, solid state electrochemical applications. XRD and vibrational Raman data were used to identify zirconium titanate materials that form from different  $\text{ZrO}_2$  compositions mixed with  $\text{TiO}_2$  and heated in oxidizing atmospheres to temperatures as high as  $1400^\circ\text{C}$ . The electrochemical properties of these zirconium titanate secondary phases were examined in a symmetric SOFC configuration. Results suggest that spatially discontinuous  $\text{Zr}_5\text{Ti}_7\text{O}_{24}$  is responsible for enhanced electrochemical activity reported in traditional Ni-YSZ cermet anodes infiltrated with  $\text{TiO}_2$ .<sup>[211,228-230]</sup>

#### $\text{ZrO}_2$ - $\text{TiO}_2$ Reactions

To characterize the influence of both temperature and yttrium content on the formation of Zr/Ti complexes, samples with equimolar mixtures of  $\text{TiO}_2$  and  $m\text{-ZrO}_2$ , 3YSZ, or 8YSZ were sintered at  $1000^\circ\text{C}$ ,  $1200^\circ\text{C}$ ,  $1300^\circ\text{C}$ , or  $1400^\circ\text{C}$  for 5 hours in air.

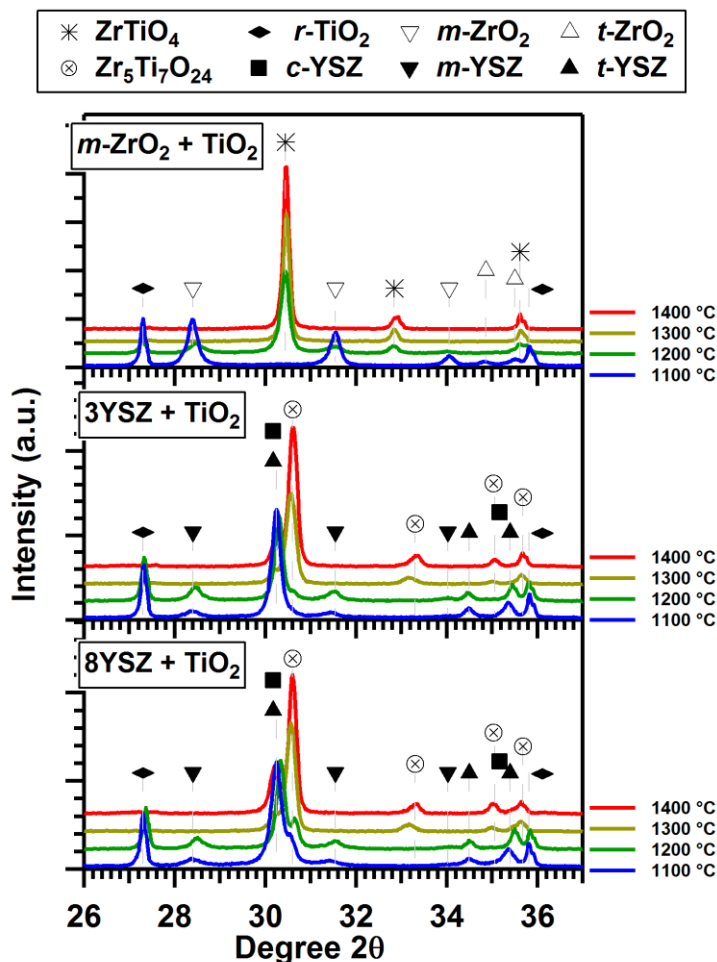


Figure 5.1. XRD data collected on powder mixtures of TiO<sub>2</sub> with (top) monoclinic ZrO<sub>2</sub>, (middle) 3 mol% Y<sub>2</sub>O<sub>3</sub> doped ZrO<sub>2</sub>, and (bottom) 8 mol% Y<sub>2</sub>O<sub>3</sub> doped ZrO<sub>2</sub> sintered at various temperatures ranging from 1100-1400 °C. For the 5 hour sintering times, the formation of Zr<sub>5</sub>Ti<sub>7</sub>O<sub>24</sub> required Y<sub>2</sub>O<sub>3</sub> to be present. Spectra have been offset on the y-axis to facilitate comparison.

At room temperature 3YSZ is comprised of a mixture of cubic and tetragonal structures while 8YSZ (the standard material used in solid oxide electrochemical cells) has an ionically conducting cubic structure. Upon heating, these mixtures of zirconia-based materials and TiO<sub>2</sub> formed zirconium titanate phases. As expected, the composition of the Zr/Ti phases depended sensitively on sintering temperature. XRD measurements

(Fig. 5.1) and vibrational Raman spectra (Fig. 5.2) show that for these short sintering times,  $\text{ZrTiO}_4$  was the only zirconium titanate phase that formed from  $m\text{-ZrO}_2/\text{TiO}_2$  mixtures while mixtures comprised of  $\text{TiO}_2$  and 3YSZ or 8YSZ had additional phases that included  $\text{Zr}_5\text{Ti}_7\text{O}_{24}$  and very small amounts of a pyrochlore structure ( $\text{A}_2\text{B}_2\text{O}_7$ ), generally represented as  $\text{Y}_2\text{Ti}_{2-y}\text{Zr}_y\text{O}_7$ .

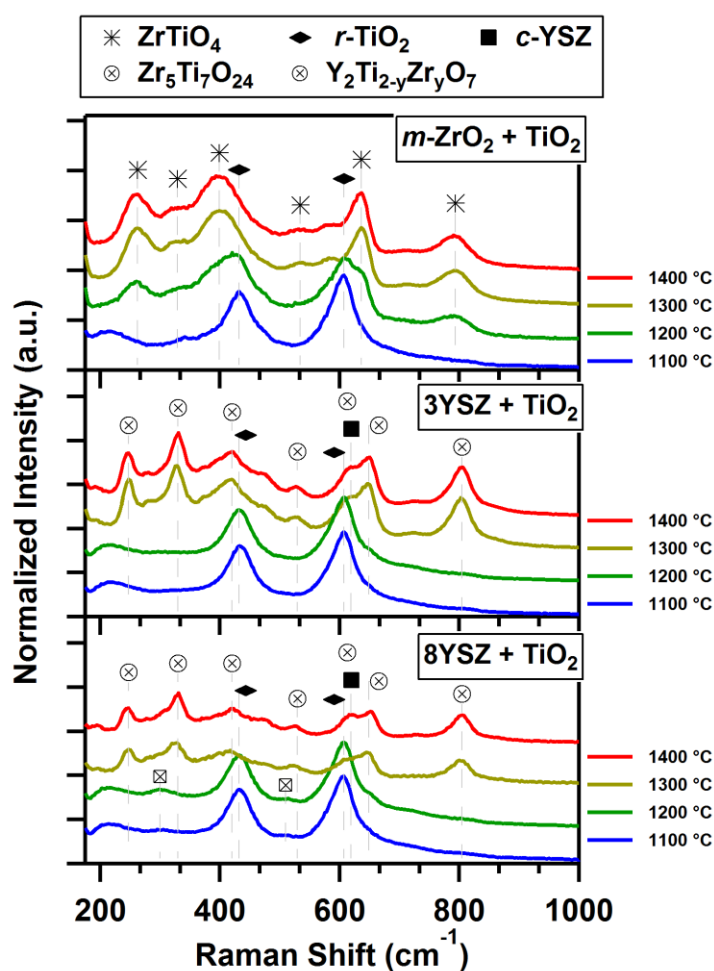


Figure 5.2. Room temperature Raman spectra of powder mixtures of  $\text{TiO}_2$  with (top)  $m\text{-ZrO}_2$ , (middle) 3YSZ, and (bottom) 8YSZ sintered at 1100-1400 °C. The Raman spectra verify that  $\text{Zr}_5\text{Ti}_7\text{O}_{24}$  and  $\text{Y}_2\text{Ti}_{2-y}\text{Zr}_y\text{O}_7$  only formed with YSZ. The complete list of Raman vibrational mode assignments is given in Table 5.1. Spectra have been offset on the y-axis to facilitate comparison.

Table 5.1 Overview of vibrational bands observed in Raman spectra collected on samples in Figure 5.2.

$m\text{-ZrO}_2 + \text{TiO}_2$ Raman Shift <sup>a</sup> ( $\text{cm}^{-1}$ )	YSZ + $\text{TiO}_2$ Raman Shift <sup>a,b</sup> ( $\text{cm}^{-1}$ )	Assignment	Literature Raman Shift [ $\text{cm}^{-1}$ ]
217 b w	217 b w	$\text{Zr}_5\text{Ti}_7\text{O}_{24}$	lit., <sup>[232]</sup> 210 and 215
	247 s	$\text{Zr}_5\text{Ti}_7\text{O}_{24}$	lit., <sup>[232]</sup> 245
262 s		$t\text{-YSZ}/c\text{-YSZ}$	256 <sup>c)</sup>
		$\text{ZrTiO}_4$	259 <sup>c)</sup> ; lit., <sup>[232]</sup> 260
	280 w	$\text{Zr}_5\text{Ti}_7\text{O}_{24}$	lit., <sup>[232]</sup> 282
	300 w	$\text{Y}_2\text{Ti}_{2-y}\text{Zr}_y\text{O}_7$	lit., <sup>[241]</sup> 308-310; lit., <sup>[242]</sup> 308
	307 sh	$\text{Zr}_5\text{Ti}_7\text{O}_{24}$	lit., <sup>[232]</sup> 310
		$c\text{-YSZ}$	318 <sup>c)</sup>
330 sh	330 s	$t\text{-YSZ}$	325 <sup>c)</sup>
		$m\text{-ZrO}_2$	328 and 340 <sup>c)</sup>
		$\text{ZrTiO}_4$	330 <sup>c)</sup>
		$\text{Zr}_5\text{Ti}_7\text{O}_{24}$	lit., <sup>[232]</sup> 340
	370 w	$t\text{-YSZ}/m\text{-ZrO}_2$	375 <sup>c)</sup>
		$\text{Zr}_5\text{Ti}_7\text{O}_{24}$	lit., <sup>[232]</sup> 380
399 s	399 w sh	$\text{ZrTiO}_4$	396 <sup>c)</sup>
		$\text{Zr}_5\text{Ti}_7\text{O}_{24}$	lit., <sup>[232]</sup> 400
	420 s	$\text{Zr}_5\text{Ti}_7\text{O}_{24}$	lit., <sup>[232]</sup> 430
432 s	432 s	$r\text{-TiO}_2$	lit., <sup>[243]</sup> 448
		$\text{Y}_2\text{Ti}_{2-y}\text{Zr}_y\text{O}_7$	lit., <sup>[241]</sup> 413-448; lit., <sup>[242]</sup> 451
	470 sh	$t\text{-YSZ}/c\text{-YSZ}$	465 <sup>c)</sup>
		$m\text{-ZrO}_2$	470 <sup>c)</sup>
		$\text{Zr}_5\text{Ti}_7\text{O}_{24}$	lit., <sup>[232]</sup> 475
	510 vw	$\text{Y}_2\text{Ti}_{2-y}\text{Zr}_y\text{O}_7$	lit., <sup>[241]</sup> 522-531; lit., <sup>[242]</sup> 532
532 w	525 w	$\text{ZrTiO}_4$	531 <sup>c)</sup>
		$m\text{-ZrO}_2$	532 <sup>c)</sup>
		$\text{Zr}_5\text{Ti}_7\text{O}_{24}$	lit., <sup>[232]</sup> 535
590 sh		$\text{ZrTiO}_4$	589 <sup>c)</sup> ; lit., <sup>[232]</sup> 580
607 s	607 s	$r\text{-TiO}_2$	lit., <sup>[243]</sup> 613
		$\text{Y}_2\text{Ti}_{2-y}\text{Zr}_y\text{O}_7$	lit., <sup>[241]</sup> 597-609
	619 s sh	$c\text{-YSZ}$	615 <sup>c)</sup>
		$\text{Zr}_5\text{Ti}_7\text{O}_{24}$	lit., <sup>[232]</sup> 625
639 s		$m\text{-YSZ}/t\text{-YSZ}$	632 <sup>c)</sup>
		$\text{ZrTiO}_4$	638 <sup>c)</sup>
	650 s	$\text{Zr}_5\text{Ti}_7\text{O}_{24}$	lit., <sup>[232]</sup> 650
710 w		$\text{ZrTiO}_4$	710 <sup>c)</sup>
	725-730 w	$\text{Zr}_5\text{Ti}_7\text{O}_{24}$	lit., <sup>[232]</sup> 730
794 s		$\text{ZrTiO}_4$	793 <sup>c)</sup>
	805 s	$\text{Zr}_5\text{Ti}_7\text{O}_{24}$	lit., <sup>[232]</sup> 800

<sup>a</sup>Peaks may not be observed at all sintering temperatures. Peak shapes are defined via b = broad, s = strong, sh = shoulder, w = weak, vw = very weak. <sup>b</sup>Peaks observed on  $\text{TiO}_2$  mixtures with 3YSZ and 8YSZ. <sup>c</sup>Raman shifts measured on reference samples for this work.

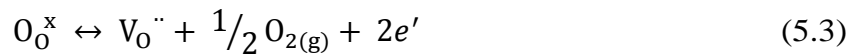
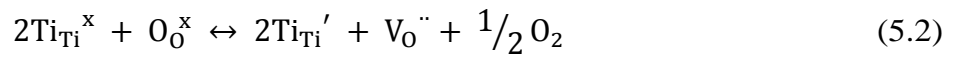
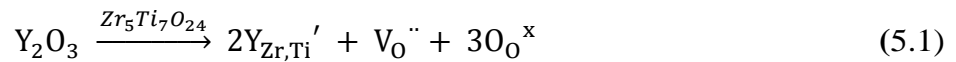
Samples prepared with  $m\text{-ZrO}_2$  and  $\text{TiO}_2$  all showed evidence of  $m\text{-ZrO}_2$ ,  $t\text{-ZrO}_2$  and rutile  $\text{TiO}_2$  ( $r\text{-TiO}_2$ ) for sintering temperatures below 1300 °C. At the higher sintering temperatures,  $\text{ZrO}_2$  reacted with  $\text{TiO}_2$  to form  $\text{ZrTiO}_4$ , as evidenced by the appearance of the peaks at 30.4°, 32.8° and 35.6° 2 $\theta$  in the XRD data (Fig. 5.1a) and vibrational bands at 262, 329, 399, 534, 585, 636 and 794  $\text{cm}^{-1}$  in the Raman spectra (Fig. 5.2a).<sup>[232,244]</sup>  $\text{ZrO}_2$  and  $\text{TiO}_2$  were converted to  $\text{ZrTiO}_4$  quantitatively during the 5 hour sintering time for temperatures higher than 1200 °C, as determined by the absence of the features associated with  $\text{ZrO}_2$  and  $\text{TiO}_2$  in both the XRD and Raman data. These results agree with previous reports showing equimolar mixtures of  $\text{TiO}_2$  and  $\text{ZrO}_2$  sintered above 1100 °C produced a single phase solid solution of orthorhombic  $\text{ZrTiO}_4$ .<sup>[235,245,246]</sup>

For samples prepared with 3YSZ and 8YSZ, reactions with  $\text{TiO}_2$  preferentially produced  $\text{Zr}_5\text{Ti}_7\text{O}_{24}$  at higher sintering temperatures. The  $c\text{-YSZ}$  phase was observed for all sintering temperatures indicating that the stabilizing  $\text{Y}_2\text{O}_3$  in the ionically conducting  $\text{ZrO}_2$  fluorite structure was not completely displaced by reaction with  $\text{TiO}_2$  during the 5 hour thermal treatment. The incomplete reaction between YSZ and  $\text{TiO}_2$  is supported by both the XRD (Fig. 5.1b and 5.1c) and Raman spectra (Fig. 5.2b and 5.2c) showing  $r\text{-TiO}_2$ ,  $m\text{-ZrO}_2$  and  $t\text{-ZrO}_2$  remained in samples sintered below 1300 °C. Previous reports have attributed incomplete conversion of YSZ and  $\text{TiO}_2$  to diffusion limitations,<sup>[235]</sup> and the role played by diffusion is currently being tested. The extent of  $\text{Zr}_5\text{Ti}_7\text{O}_{24}$  formation was enhanced with higher  $\text{Y}_2\text{O}_3$  doping levels and sintering temperatures. The XRD peaks at 30.6° and 33.3° 2 $\theta$  show that  $\text{Zr}_5\text{Ti}_7\text{O}_{24}$  began to form at

1200 °C with the 3YSZ samples (Fig. 5.1b) and at 1100 °C with the 8YSZ samples (Fig. 5.1c).

This temperature dependent formation is further corroborated with the appearance of the features in the Raman spectra (Fig. 5.2b and 5.2c) at approximately 247, 280, 330, 375, 400, 420, 473, 525, 620, 650, 730 and 805  $\text{cm}^{-1}$  that are attributed to the vibrational modes of  $\text{Zr}_5\text{Ti}_7\text{O}_{24}$ . A complete list of all detected Raman vibrational modes is presented in Table 5.1. Peak broadening and shifts in position compared to the Raman spectrum reported by Azough *et al.* are attributed to variations in cation stoichiometry/ordering and oxygen defects due to different sintering and heating/cool down times.<sup>[232]</sup> After thermal treatment, pyrochlore oxide species have been detected by several groups.<sup>[231,233,247,248]</sup> This structure is not expected to be dominant due to the relatively low Y content in our samples,<sup>[249]</sup> and any pyrochlore content present in the samples was below the detection limit of XRD (~3% by mass). Although Raman spectroscopy is more sensitive to subtle phase and compositional changes, small quantities of the pyrochlore are difficult to identify in Raman spectra collected on samples sintered at higher temperatures due to the overlapping vibrational bands in the low frequency region. Weak signals at ~300  $\text{cm}^{-1}$  and 520  $\text{cm}^{-1}$  are visible in Raman spectra for 8YSZ samples sintered at 1100 °C and 1200 °C but are indistinguishable at the higher temperatures from features assigned to  $\text{Zr}_5\text{Ti}_7\text{O}_{24}$  (and confirmed by XRD). These Raman bands may arise from an ionically conductive pyrochlore structure,<sup>[241,242]</sup> but, again, the relative abundance of any pyrochlore phase is expected to be very small.

These findings suggest that the  $\text{Zr}_5\text{Ti}_7\text{O}_{24}$  is the dominant phase formed by reaction between  $\text{TiO}_2$  and 8YSZ, especially at higher sintering temperatures. Since  $\text{Y}_2\text{O}_3$  is needed to facilitate  $\text{Zr}_5\text{Ti}_7\text{O}_{24}$  formation on reasonable timescales, the role of  $\text{Y}_2\text{O}_3$  must be considered in order to optimize any mechanism that promotes secondary phase formation in  $\text{TiO}_2$  doped, electrochemically active materials containing YSZ. Solid oxide electrochemical cells typically use  $\text{ZrO}_2$  doped with 8 mol%  $\text{Y}_2\text{O}_3$  because of the material's relatively high ionic conductivity and mechanical stability.<sup>[27,250]</sup> Moreover, the solubility of  $\text{TiO}_2$  in YSZ increases with higher Y content (up to the solubility limit of approximately 10 mol%  $\text{TiO}_2$  in *c*-YSZ).<sup>[251]</sup> A phase transition from *c*-YSZ to *t*-YSZ occurs as Ti is incorporated into the cell structure due to the smaller ionic radius of  $\text{Ti}^{4+}$  compared to  $\text{Zr}^{4+}$ .<sup>[247,252]</sup> Although *t*-YSZ exhibits diminished conductivity, the substitution of  $\text{Y}^{3+}$  and reduction of  $\text{Ti}^{4+}$  within the lattice is expected to foster an increase in both ionic and electronic conductivities.<sup>[233,253]</sup> The defect chemistry mechanisms are shown in Eq. (5.1-5.3) using Kröger Vink notation:



For the short dwell thermal treatments utilized in this study, the literature indicates that  $\text{Zr}_5\text{Ti}_7\text{O}_{24}$  structure is favored with  $\text{Y}^{3+}$  substitution.<sup>[235-237]</sup> Yttrium substitutions are possible on both the Zr and Ti sub-lattices, in which  $4^+ \leftrightarrow 3^+$  cation substitution is expected to form the oxygen deficient structure:  $\text{Y}_x(\text{Zr}_5\text{Ti}_7)_{1-x}\text{O}_{24-y}$  implied by Eq. (5.1).<sup>[251]</sup> The  $\text{Y}^{3+}$  substituted structure is facilitated by oxygen vacancies, in a



manner similar to stabilized zirconium oxide, providing a mechanistic basis for oxygen ion mobility in the  $\text{Zr}_5\text{Ti}_7\text{O}_{24}$  material. Furthermore, under reducing conditions, oxygen is removed from the lattice as the  $\text{Ti}^{4+}$  ions reduces to  $\text{Ti}^{3+}$  ions generating additional oxygen vacancies shown in Eq. (5.2). Oxygen vacancy generation is accompanied by the formation of charge carriers (electrons) in which the electron conductivity has a  $\sigma_{\text{electrons}} \propto p\text{O}_2^{-1/4}$  dependency, as indicated by Eq. (5.3), supporting mixed ion-electron conductivity.<sup>[219]</sup>

Consequently, the overall ionic conductivity of *c*-YSZ doped with  $\text{TiO}_2$  will depend on both the extent of *t*-YSZ formation and the defect chemistry associated with Ti. These competing effects may enable  $\text{Zr}_5\text{Ti}_7\text{O}_{24}$  to function as a MIEC and could explain the improved electrochemical performance previously observed with  $\text{TiO}_2$  infiltrated Ni-YSZ anodes sintered at 1400 °C.<sup>[228,229]</sup> Resolving this question definitively requires identifying  $\text{Zr}_5\text{Ti}_7\text{O}_{24}$ 's relevant electrochemical properties.

#### Electrochemical Measurements of $\text{Zr}_5\text{Ti}_7\text{O}_{24}$

In order to test the electrochemical properties of  $\text{Zr}_5\text{Ti}_7\text{O}_{24}$  formed from mixtures of 8YSZ and  $\text{TiO}_2$  sintered at 1400 °C, a pellet of the sintered material was made to serve as an electrolyte between two Pt electrodes (Fig. 5.3). Both linear sweep voltammetry (LSV) and electrochemical impedance spectroscopy (EIS) experiments were performed at 800 °C with dry  $\text{H}_2$  as the fuel for the designated anode and air as the oxidant over the cathode (Fig. 5.4). In addition to the electrochemical measurements, *in operando* Raman spectra were collected from the electrolyte on the designated anode side of the device (Fig. 5.5). For the first 5 hours, the sample was held at OCV to allow materials to

equilibrate prior to polarization at 158  $\mu\text{A}$  (equivalent to 40% of the maximum current measured during LSV measurements) for the last 3 hours of testing. LSV and EIS measurements were performed periodically to monitor the cell's electrochemical performance and ionic conductivity.

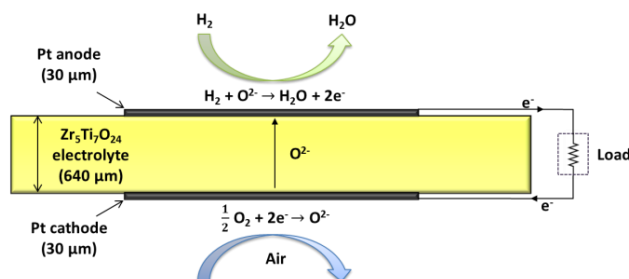


Figure 5.3. Schematic of the symmetric cell used in the electrochemical studies of  $\text{Zr}_5\text{Ti}_7\text{O}_{24}$ . Voltammetry, EIS and in operando Raman spectroscopy measurements were performed to examine the mixed ionic and electronic properties of  $\text{Zr}_5\text{Ti}_7\text{O}_{24}$  at 800  $^{\circ}\text{C}$ .

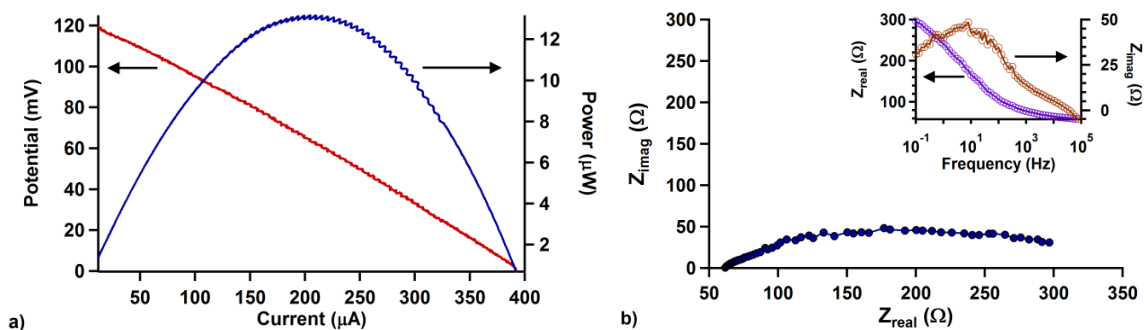


Figure 5.4. (a) LSV and (b) complex impedance at OCV, with an inset of the real and imaginary impedances as a function of frequency, obtained from the symmetric cell with platinum electrodes and an electrolyte comprised primarily of  $\text{Zr}_5\text{Ti}_7\text{O}_{24}$ . One side of the symmetric cell was exposed to 85 ml/min air while the opposite side was exposed to 100 ml/min  $\text{H}_2$  and 100 ml/min Ar.

The measured open circuit voltage was low, ranging from 120-130 mV, indicating that the sample had electronic conducting properties and was unable to sustain the  $\sim 1.2\text{V}$  commonly observed in SOFCs with an  $\text{H}_2$  fuel.<sup>[90,129,254]</sup> Optical spectroscopy coupled

with repeated electrochemical measurements ensured that the anode and cathode remained atmospherically isolated from each other. (*Vide infra.*) The observed response is attributed to the reduction of  $\text{Ti}^{4+}$  to  $\text{Ti}^{3+}$  creating charge carriers (see Eq. (5.2)) that internally short circuit the electrolyte.<sup>[253]</sup> Internal shorting of electrolytes is well established in rare earth doped cerium oxides  $(\text{RE})\text{CeO}_2$ , where  $\text{RE} = \text{Gd}, \text{Sm}$ . With these materials as electrolytes, OCV decreases as mixed conduction develops when  $\text{Ce}^{4+}$  is reduced to  $\text{Ce}^{3+}$ .<sup>[219,222,223,255]</sup>

Polarizing the  $\text{Pt-Zr}_5\text{Ti}_7\text{O}_{24}\text{-Pt}$  device in a fuel cell configuration resulted in maximum currents and powers of  $\sim 400 \mu\text{A}$  and  $\sim 13 \mu\text{W}$ , respectively, (Fig. 5.4a). While these values fall far short of the expectations one would have of an SOFC electrolyte, they do indicate that zirconium-titanate phases can conduct oxide ions meaning that  $\text{Zr}_5\text{Ti}_7\text{O}_{24}$  functions as a MIEC. The electrochemical properties of the electrolyte were explored further using EIS (Fig. 5.4b) where the high frequency arc observed in the complex impedance plots is attributed with the response of the bulk material. The bulk resistance (x-axis intercept in Fig. 5.4b) that is associated with an electrolyte's ionic conductivity decreased from  $105 \Omega$  to  $65 \Omega$  during the 5 hour exposure to  $\text{H}_2$  prior to polarization. The decrease in bulk resistance is attributed to the formation of oxygen vacancies as  $\text{Ti}^{4+}$  ions were reduced within the oxide lattice (see Eq. (5.2)) on the anode side of the electrolyte.

EIS and voltammetry data show that the  $\text{Zr}_5\text{Ti}_7\text{O}_{24}$  'electrolyte' yields a significant electronic and ionic conduction component. The large bulk resistance may arise from the sample thickness and/or low ionic conductivity. These results imply that

$\text{Zr}_5\text{Ti}_7\text{O}_{24}$  present as a secondary phase in conventional solid oxide cermet electrodes can expand the putative three-phase boundary in YSZ-based cermet anodes that have been doped with  $\text{TiO}_2$  and sintered at high temperatures.

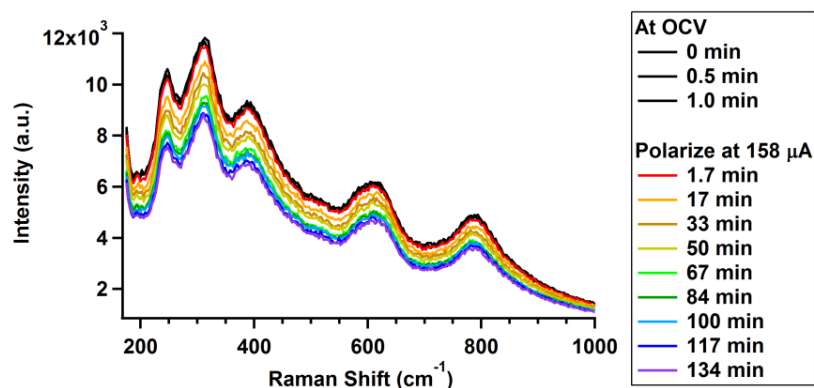


Figure 5.5. Raman spectra collected on the  $\text{Zr}_5\text{Ti}_7\text{O}_{24}$  electrolyte exposed to  $\text{H}_2$  at  $800^\circ\text{C}$ . Spectra were continuously recorded with the cell at open circuit voltage (black traces at OCV) for the first three scans and during polarization at  $158\ \mu\text{A}$  (colored traces). The Raman spectra exhibited  $\sim 25\%$  reduction in overall signal intensity after 2 hours under polarization.

*In operando* Raman spectra collected from the  $\text{Zr}_5\text{Ti}_7\text{O}_{24}$  exposed to  $\text{H}_2$  at OCV and during polarization show that the  $\text{Zr}_5\text{Ti}_7\text{O}_{24}$  is stable during fuel cell operation and no additional secondary phases formed (Fig. 5.5). The reducing conditions (due to the ambient  $\text{H}_2$  atmosphere and applied anodic potential) resulted in an overall decrease in Raman intensities. This response is attributed to a change in oxidation state at the surface layer of the  $\text{Zr}_5\text{Ti}_7\text{O}_{24}$  and has been observed in previous studies with YSZ.<sup>[38,256,257]</sup> Polarizing the sample reduces the metal oxides and changes the reflectivity of the  $\text{Zr}_5\text{Ti}_7\text{O}_{24}$  surface. These results support the proposed mechanism in Eq. (5.1) showing how reducing conditions create oxygen vacancies within the material.

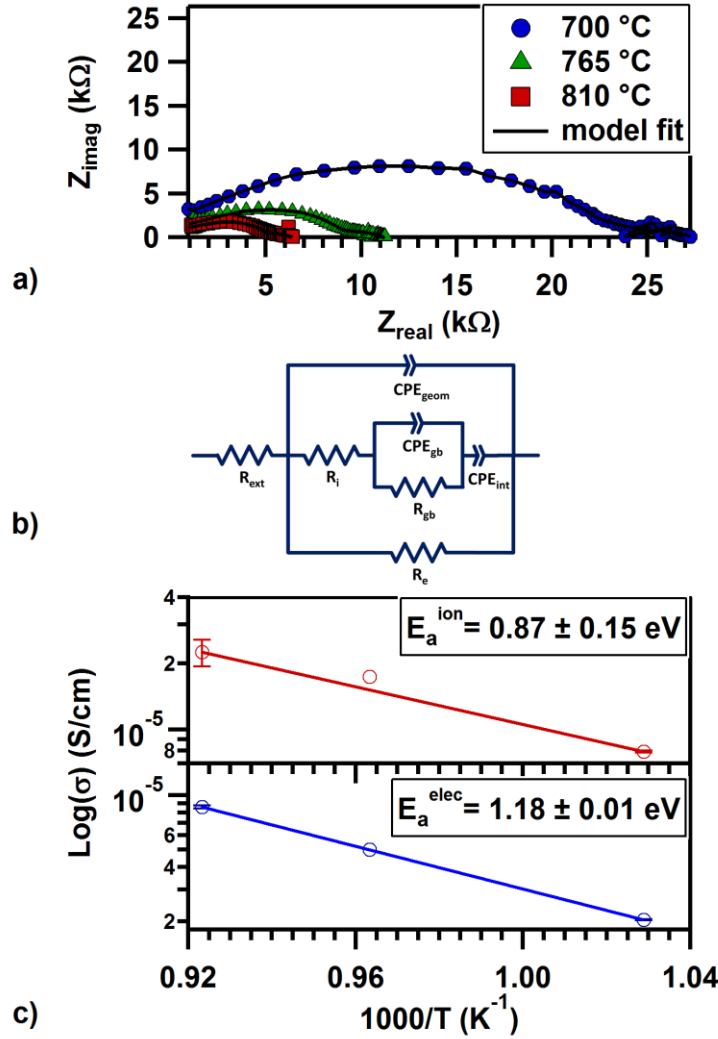


Figure 5.6. (a) Representative complex impedance spectra collected from a  $\text{Zr}_5\text{Ti}_7\text{O}_{24}$  sample heated at various temperatures at OCV. (b) The equivalent circuit used to model the ionic and electronic conductivities, based off of work proposed by Huggins.<sup>[70]</sup> (c) Arrhenius plots and calculated activation energies of the (top) ionic and (bottom) electronic conductivities.

To confirm the MIEC properties of  $\text{Zr}_5\text{Ti}_7\text{O}_{24}$  additional impedance experiments were performed using the same symmetric cell but with equivalent oxidizing (air) atmospheres on either side of the assembly. Fitting impedance data acquired at different

temperatures to an equivalent circuit proposed by Gur and Huggins,<sup>[258]</sup> data were acquired in  $\sim 50$  °C increments and fit to determine frequency dependent ionic and electronic resistivities.<sup>[239,240]</sup> An Arrhenius analysis of the inverse resistivities (or conductivities) resulted in calculated activation energies. Representative impedance data and the equivalent circuit are shown in Figure 5.6a and 5.6b, respectively. Figure 5.6c shows the temperature dependence of the ionic and electronic conductivities.

From the slopes of the lines in Figure 5.6c, we report  $E_{a,ionic} = 0.87 \pm 0.15$  eV and  $E_{a,electronic} = 1.18 \pm 0.01$  eV. These results are similar in magnitude to equivalent quantities calculated for other known MIEC ceramics. For example above 700 °C, GDC has an  $E_{a,ionic} = 0.68$  eV and  $E_{a,electronic} = 0.85$  eV<sup>[239]</sup> while lanthanum strontium gallium magnesium oxide (LSGM), a popular MIEC cathode material, has an  $E_{a,ionic} = 0.74$  eV and  $E_{a,electronic} = 0.73$  eV.<sup>[259]</sup> These comparisons support the hypothesis that the MIEC properties of  $Zr_5Ti_7O_{24}$  are capable of transforming the three-phase boundary in Ni-YSZ cermet electrodes from a one-dimensional into a two-dimensional region. The effect would significantly enhance electrochemical efficiency.

### Conclusions

Experiments were conducted to explore the formation of secondary phases in  $TiO_2/ZrO_2$  systems used in high temperature electrochemical applications. Reactions between  $TiO_2$  and  $ZrO_2$  polymorphs were dependent on sintering temperature and the presence of  $Y_2O_3$ . Thermal treatment with the *m*- $ZrO_2$  produced the disordered  $ZrTiO_4$  structure while samples containing YSZ formed the ordered  $Zr_5Ti_7O_{24}$  structure and

pyrochlore. For the 5 hour dwell times, formation of the secondary phases was enhanced at sintering temperatures above 1200 °C. Voltammetry and EIS data showed that  $\text{Zr}_5\text{Ti}_7\text{O}_{24}$  prepared with equimolar mixtures of  $\text{TiO}_2$  and 8YSZ sintered at 1400 °C, behaved as a MIEC in electrochemical cells operating above 700 °C. The findings from the presented studies suggest that formation of  $\text{Zr}_5\text{Ti}_7\text{O}_{24}$  in Ni-YSZ anodes can expand the electrochemically active region near the three-phase boundary by serving as a mixed ion-electron conducting material.

#### Acknowledgements

This work was supported by the National Science Foundation (NSF-DMR 1411210). The authors would like to acknowledge the Imaging and Chemical Analysis Laboratory (ICAL) at Montana State University for access to XRD and FEM. The authors thank Dr. Hugo Schmidt (Montana State University, Department of Physics) for instructive conversations.

## CHAPTER SIX

REVERSIBLE DECOMPOSITION OF SECONDARY PHASES IN BAO  
INFILTRATED LSM ELECTRODES- POLARIZATION EFFECTSContribution of Authors and Co-Authors

Manuscript in Chapter 6

Author: Marie L. Traulsen

Contributions: Prepared samples and aided in the acquisition of high temperature Raman spectra and electrochemical measurements on the LSM cells. Analyzed data, generated figures, and wrote the manuscript in preparation for publication.

Co-Author: Melissa D. McIntyre

Contributions: Acquired high temperature Raman spectra and electrochemical measurements on the LSM cells. Analyzed data, generated figures, and aided in the preparation of the Raman section of the manuscript.

Co-Author: Kion Norrman

Contributions: Acquired and aided in the analysis of ToF-SIMS data. Edited/commented on the manuscript.

Author: Simone Sanna

Contributions: Prepared thin film samples sample using pulse laser deposition. Edited/commented on the manuscript.

Co-Author: Mogens B. Mogensen

Contributions: Provided important insight into interpreting the experimental results. Aided in the preparation of the manuscript and figures.

Co-Author: Robert A. Walker

Contributions: Provided important insight into interpreting the experimental results. Aided in the preparation of the manuscript and figures.



Manuscript Information Page

Marie L. Traulsen, Melissa D. McIntyre, Kion Norrman, Simone Sanna, Mogens B.  
Mogensen, Robert A. Walker  
Advanced Materials Interfaces

Status of Manuscript:

☐ Prepared for submission to a peer-reviewed journal

☐ Officially submitted to a peer-review journal

☒ Accepted by a peer-reviewed journal

☐ Published in a peer-reviewed journal

Publication by John Wiley & Sons, Inc.

Accepted October 2016

# REVERSIBLE DECOMPOSITION OF SECONDARY PHASES IN BaO INFILTRATED LSM ELECTRODES- POLARIZATION EFFECTS

Marie L. Traulsen<sup>†</sup>, M. D. McIntyre<sup>‡</sup>, K. Norrman<sup>†</sup>, S. Sanna<sup>†</sup>, M. B. Mogensen<sup>†</sup>,  
R. A. Walker<sup>‡</sup>

<sup>†</sup>Department of Energy Conversion and Storage, Technical University Of Denmark,  
Frederiksborgvej 399, 4000 Roskilde, Denmark

<sup>‡</sup> Department of Chemistry and Biochemistry, Montana State University, Bozeman,  
Montana 59717, USA

## Abstract

*In operando* Raman spectroscopy is used to study ceramic  $\text{La}_{0.85}\text{Sr}_{0.15}\text{MnO}_{3\pm\delta}$  (LSM) electrodes infiltrated with BaO. The aim of this work is to clarify why BaO infiltration reduces the polarization resistance in oxygen containing atmospheres. Prior to the *in operando* experiments, *ex situ* XRD and Raman spectroscopy reveals the formation of a secondary phase,  $\text{Ba}_3\text{Mn}_2\text{O}_8$ , on the electrode. During the *in operando* Raman investigation of the BaO infiltrated  $\text{La}_{0.85}\text{Sr}_{0.15}\text{MnO}_{3\pm\delta}$  electrodes, experiments are performed at 300 °C and 500 °C with oxygen partial pressure 0.1 atm and with -1 V or +1 V applied potential. A changing electrode surface is observed during operation as the  $\text{Ba}_3\text{Mn}_2\text{O}_8$  secondary phase decomposes and manganese oxide accumulates on the electrode surface during cathodic polarization. The observed changes are reversible. These results suggest that the formation of  $\text{Ba}_3\text{Mn}_2\text{O}_8$  is responsible for the reduced polarization resistance observed at OCV in an oxygen containing atmosphere. Furthermore, the results illustrate the dramatic differences between the electrode surface composition at OCV and during cathodic polarization. Overall, the results highlight the

dynamic interactions between minor secondary phases and applied potential, a general effect that may be important for the high performance frequently observed with ceramic electrodes prepared by infiltration.

### Introduction

Understanding the surface chemistry of ceramic electrodes is important for a diverse range of electrocatalytic technologies including fuel cells, electrolysis cells and electrochemical gas purification systems.<sup>[6,260,261]</sup> A popular approach for improving the electrocatalytic properties of ceramic electrodes employs infiltration during electrode manufacturing.<sup>[262,263]</sup> During the infiltration step, a material is added in the form of an aqueous precursor solution to an existing scaffold, where the desired material forms during subsequent conditioning of the electrode.<sup>[263]</sup> An unintended consequence of this approach can be the formation of minor secondary phases, either from the infiltrate itself, or from reactions between the infiltrate and the scaffold.<sup>[264,265]</sup> Recent investigations on  $\text{La}_{1-x}\text{Sr}_x\text{CoO}_{3-\delta}$  (LSC) based electrodes have indicated that the presence of minor secondary phases may even improve electrode performance due to the formation of hetero-interfaces.<sup>[264,266-268]</sup> These and other studies of secondary phases often draw conclusions correlating electrode composition with performance based on *ex situ* studies and *in operando* electrochemical characterization. The *ex situ* analyses performed before and after usage provide valuable insight into irreversible changes that occur in electrode composition and structure while *in operando* electrochemical measurements report on how performance changes with different operating conditions. Both approaches – *ex situ*

studies and *in operando* electrochemical characterization – fail to produce direct molecular and materials specific information about the chemical condition of the electrode *in operando*. Electrochemical characterization and materials specific data acquired *in operando* are necessary to understand and improve electrocatalytic properties such as activity, selectivity and durability. Here we define *in situ* studies as studies in which one or two parameters such as temperature, electrical polarization, or atmosphere reflect operating conditions while in *in operando* studies all three parameters correspond to realistic values during operation of ceramic electrodes. The importance of such measurements was demonstrated recently by Backhaus-Ricoult *et al.* and Siebert *et al.* who employed *in situ* XPS and *in operando* Raman spectroscopy, respectively, in studies of perovskite based electrodes and their electrocatalytic properties.<sup>[269,270]</sup> Data showed reversible changes in composition and structure of perovskite oxide electrodes during electrical polarization that could only be observed with *in operando* spectroscopic measurements.<sup>[269,270]</sup> When the electrode returned to open circuit voltage (OCV), the electrode composition resumed its pre-operational state.

One of the most thoroughly investigated perovskites used for ceramic electrodes has been strontium doped lanthanum manganite (LSM), primarily due to the material's high electronic conductivity at high temperatures and the good compatibility with the commonly used yttria stabilized zirconia (YSZ) electrolyte.<sup>[271]</sup> In order to improve the performance of LSM based electrodes for SOFC applications, especially at lower temperatures, experiments with infiltrated LSM electrodes have been conducted including infiltration of the entire LSM phase, infiltration with noble metals or single

oxides as “dopants” and infiltration with high performance oxygen ion conductors.<sup>[263,272-277]</sup> Similarly, LSM based electrodes for electrochemical gas purification have been infiltrated to improve their electrocatalytic properties towards conversion of gaseous pollutants.<sup>[36,278-280]</sup> Infiltration with BaO, possibly with BaCO<sub>3</sub> as the final product, has been observed to cause a significant reduction in the polarization resistance on LSM-based electrodes.<sup>[36,281,282]</sup> The effect of the BaO infiltration has been attributed to changes in processes related to adsorption, dissociation and charge transfer for the gaseous reactant; however, exactly how BaO infiltration affects these processes has not yet been clarified and, as pointed out by Hong *et al.*, attention should be paid to the chemical bonding state of the Ba atom in the surface of the electrodes.<sup>[36,281,282]</sup>

In order to identify the reason(s) for improved performance observed with BaO modified LSM electrodes in an oxygen atmosphere and to identify the behavior of secondary phases under operating conditions, the studies described in this work employed *in operando* Raman spectroscopy coupled with electrochemical measurements.<sup>[36,281,282]</sup> Thin film LSM model electrodes with and without BaO modification were employed, and the studies were conducted under realistic operating conditions for intermediate temperature SOFCs and electrochemical gas conversion cells. Changes in electrode composition were examined as a function of temperature and electrical polarization. The data suggest that at OCV conditions Ba<sub>3</sub>Mn<sub>2</sub>O<sub>8</sub>, a secondary phase formed during the infiltration step, is responsible for the reduced polarization resistance. Furthermore the data showed significant, reversible changes in the electrode surface composition with an applied electrical polarization on the electrodes, resulting in a change in the MnO<sub>x</sub>

species at the electrode surface and reversible decomposition of a secondary phase,  $\text{Ba}_3\text{Mn}_2\text{O}_8$ , with cathodic polarization.

## Experimental Methods

### Sample Architecture and Material Selection

In commercial applications of infiltrated LSM electrodes, the electrode is typically a porous composite electrode with the primarily electron-conducting LSM perovskite entangled with an oxygen-ion conducting electrolyte.<sup>[31,283]</sup> Common electrolyte materials are YSZ for operating temperatures  $> 600^\circ\text{C}$  and CGO for operating temperatures  $< 600^\circ\text{C}$ .<sup>[284]</sup> However, in this work the majority of the *in operando* experiments were performed using a thin film model electrode in order to ensure uniform polarization of the electrode. To assure consistency between thin film model electrodes and conventional porous composite electrodes, both electrode types were fabricated and Raman spectra were recorded from each electrode type. Sketches of the electrochemical cells with thin film and porous electrodes respectively are shown in Figure 6.1.

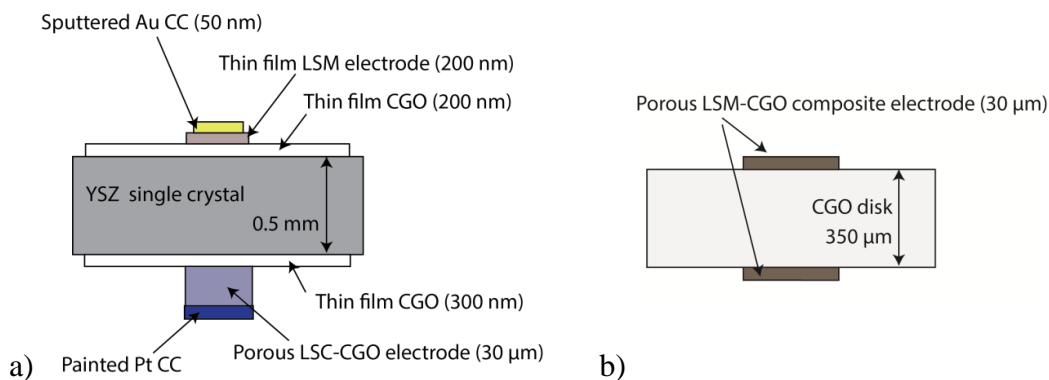


Figure 6.1 Sketch of the electrochemical cells applied in this work (a) the thin film model cell and (b) the “conventional cell” with porous LSM-CGO electrode. CC denotes the current collector.

Experiments described below used LSM as the electron conducting phase due to this material's structural stability and its widespread usage in solid oxide electrolysis/fuel cells and electrochemical cells intended to remediate  $\text{NO}_x$  pollutants from diesel exhaust streams.<sup>[31,278,285,286]</sup> Gadolinium-doped ceria (CGO) served as the electrolyte phase in the conventional cells with porous electrodes due to CGO's high oxygen ion conductivity at comparatively low temperatures ( $< 600\text{ }^\circ\text{C}$ ).<sup>[284]</sup> Furthermore, a CGO thin film layer was applied adjacent to the LSM thin film electrode in the thin film model cell to mimic the materials composition of the conventional cells. For the thin film model cell, a YSZ single crystal served as both the electrolyte and substrate for the CGO and LSM thin films due to the lack of commercially available CGO single crystals. In accordance with these considerations, LSM15 ( $(\text{La}_{0.85}\text{Sr}_{0.15})_{0.9}\text{MnO}_{3\pm\delta}$ ), CGO10 ( $\text{Ce}_{0.90}\text{Gd}_{0.10}\text{O}_{1.95}$ ) and for the thin film samples additionally YSZ ( $(\text{Y}_2\text{O}_3)_{9.5}(\text{ZrO}_2)_{90.5}$ ), were used in the experiments described below.

Fabrication of Electrochemical thin Film Model Cell. The thin film model cell was designed to mimic conventional cells with a composite electrode consisting of an oxygen conducting CGO phase and an electronic conducting LSM phase. A previous study on this type of model cell has been reported elsewhere with further details on the cell preparation.<sup>[256]</sup> The YSZ single crystals (CrysTec GmbH, Germany) that served as electrolyte and substrate for the thin films had a (100) exposed face, were single side polished and measured 2.54 cm in diameter. The LSM thin film electrode and thin films of CGO were deposited on the YSZ using pulsed laser deposition (PLD) with a KrF excimer laser. During the depositions, the fluence was  $2\text{ Jcm}^{-2}$  with a laser frequency of

10 Hz and the distance between the substrate and target was 7.5 cm. The CGO thin films (200-300 nm) were deposited at a substrate temperature of 700 °C and oxygen partial pressure of  $5 \times 10^{-4}$  mbar on both the polished and the rough side of the YSZ single crystal. The LSM thin film electrode (~200 nm) was deposited on top of the CGO layer on the polished side of the YSZ single crystal and a shadow mask maintained LSM thin film electrode dimensions of 0.5 cm x 1 cm. The LSM deposition was conducted with a substrate temperature of 600 °C and with oxygen partial pressure at  $7 \times 10^{-4}$  mbar. The oxygen partial pressure was increased to 0.02 mbar immediately after the deposition and during cool-down to avoid oxygen deficiencies from developing in the LSM electrode. An LSC-CGO (50 wt.%  $(\text{La}_{0.6}\text{Sr}_{0.4})_{0.99}\text{CoO}_3$ -50 wt.%  $\text{Ce}_{0.9}\text{Gd}_{0.1}\text{O}_{1.95}$ ) porous electrode (30  $\mu\text{m}$ ) was screen-printed as a “counter-electrode” to the thin film LSM electrode and was deposited on top of the CGO thin film on the rough side of the YSZ single crystal. Following the application of the LSC-CGO electrode, the entire electrochemical cell was heated to 930 °C for 24 hours. A Pt current collector was painted on the LSC-CGO electrode and sintered at 900 °C for 2 hours. Finally, Au was sputtered onto the thin film electrode and the cell was heat-treated at 700 °C for 120 hours allowing the Au to sinter, with the intention of forming a continuous Au network for current collection. As subsequent imaging revealed the formation of separate  $\mu\text{m}$ -sized Au particles rather than an Au network, adequate current collection was obtained by applying an Au mesh in the final test-set-up. The complete architecture of the thin film model cell is shown in Figure 6.1a and a SEM image of the LSM thin film electrode and the adjacent layers is found in A1.1.



### Preparation of “Conventional” Electrochemical

#### Cell with Porous LSM-CGO Electrodes.

Electrochemical cells with porous LSM-CGO composite electrodes were prepared as follows: a CGO10 (Rhodia) electrolyte with 1% Fe added as a sintering aid was tape-casted, stamped out in disks and sintered at a maximum temperature of 1250 °C for 4 hours. After sintering, the electrolyte disks were dense, 350  $\mu\text{m}$  thick and had a diameter of 23 mm. A circular 10 mm diameter 50 wt.% LSM15 – 50 wt.% CGO10 composite electrode was screen-printed onto each side of the CGO electrolyte disks and sintered with the maximum temperature of 1050 °C for 2 hours, resulting in  $\sim 30$   $\mu\text{m}$  thick porous electrodes. A sketch of the cell with porous LSM-CGO electrodes is shown in Figure 6.1b.

Addition of BaO. BaO was added to both a dense, thin film LSM electrode and a porous LSM-CGO electrode. Due to reaction with  $\text{CO}_2$  in the atmosphere and reaction with the electrode components, the majority of the Ba added was present as  $\text{BaCO}_3$  or as Ba-Mn-O compounds (*vide supra*) throughout the *in operando* experiments; however for brevity, these samples are referred to as BaO-infiltrated samples. Due to differences in sample architecture between the thin film LSM electrode and a porous LSM-CGO electrode, slightly different procedures were used for the BaO addition. The porous LSM-CGO electrodes were infiltrated by adding a droplet of 0.32 M  $\text{Ba}(\text{NO}_3)_2$  (aq) onto the electrode surface and the solution was allowed to soak into the porous structure. Excess solution was removed from the surface and the infiltrated cells were heat-treated at 700 °C for 1 hour to decompose the  $\text{Ba}(\text{NO}_3)_2$  into BaO. This procedure was repeated 7 times to obtain a uniform coverage of  $\sim 50$  nm BaO particles throughout the electrodes.

A similar procedure was employed for deposition of  $\text{Ba}(\text{NO}_3)_2$  onto the LSM thin film electrodes, where an aqueous 0.032 M  $\text{Ba}(\text{NO}_3)_2$  solution containing 10 wt% P123 dispersant (BASF) was used. Excess solution on the thin film electrodes was not wiped off of the surface prior to the heat-treatment at 700 °C and the  $\text{Ba}(\text{NO}_3)_2$  deposition step was only performed once. This procedure resulted in large agglomerations of BaO on some areas of the electrode (Fig. 6.2a), while in other areas nanosized BaO particles were well dispersed on the electrode surface as intended. It is emphasized that the *in operando* Raman spectroscopy reported in this paper was conducted on the electrode area with well-dispersed BaO. Top-view SEM images of an electrode area with BaO present as nanoparticles is shown in Figure 6.2b and a bare LSM thin film electrode for comparison is shown in Figure 6.2c. The BaO particles on the surface caused the BaO treated electrode to appear more “roughened” (Fig. 6.2b) compared to the non-infiltrated surface (Fig. 6.2c).

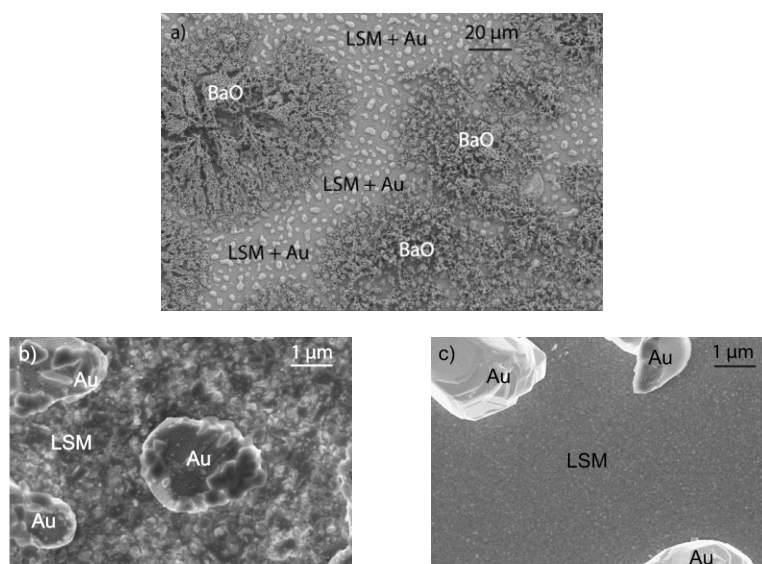


Figure 6.2. Top-view SEM images of the LSM thin film electrodes (a, b) with BaO deposition and (c) without BaO deposition.

### Scanning Electron Microscopy

Electrode surfaces and cross-sections of broken cells were investigated with scanning electron microscopy (SEM) on a Zeiss Supra 35 microscope. The microstructure of the electrode surfaces was investigated using the InLens detector with a 5 kV acceleration voltage and without any pre-treatment of the electrode. The thickness of the thin film layers of broken cross-sections was determined using the backscattered electron detector with a 10 kV acceleration voltage and the cross sections were carbon coated to avoid charging of the sample.

### Time-of-Flight-Secondary Ion Mass Spectroscopy

Analysis of the elemental distribution through LSM thin film electrodes without and with BaO deposition was performed with Time-of-Flight Secondary Ion Mass Spectrometry (TOF-SIMS) using a TOF-SIMS IV (ION-TOF GmbH, Münster, Germany). The 25 ns pulses of 25 keV  $\text{Bi}^+$  (primary ions) were used at a repetition rate of 10 kHz, yielding a target current of 0.7 pA. Depth profiling was performed with approximately 2 nm depth resolution on a  $200 \times 200 \mu\text{m}^2$  surface analysis area centered in a  $300 \times 300 \mu\text{m}^2$  sputter area. The 30 nA of 3 keV  $\text{Xe}^+$  was used as sputter ions (10 second sputtering, 1 second pause and then analysis using one scan and  $256 \times 256$  pixels). For all analyses electron bombardment (20 eV) was used to minimize charge built-up at the surface. Desorbed secondary ions were accelerated to 2 keV, mass analyzed in the flight tube, and post-accelerated to 10 keV before detection.

### X-ray Photoelectron Spectroscopy

The surface stoichiometry of four LSM thin film electrodes without BaO deposition were analyzed with X-ray photoelectron spectroscopy (XPS) performed on a K-alpha (Thermo Electron Limited, Winsford, UK) using a monochromated Al-K- $\alpha$  X-ray source and a take-off angle of 90° from the surface plane. Atomic concentrations were determined from surface spectra (0–1350 eV, 100 eV detector pass energy) and were calculated by determining the relevant integral peak intensities using a Shirley type background. Each sample surface was analyzed at three different surface locations and the average value for all four samples is reported in the results section.

### Raman Spectroscopy

*In operando* Raman spectra were acquired using a Renishaw InVia spectrometer with a 488 nm Ar-ion laser and Pelletier cooled charge-coupled device (CCD) detector. The cells were mounted in an assembly developed originally to perform *in operando* studies of solid oxide cells and has been described in more detail elsewhere.<sup>[126,181]</sup> Cells were fixed on the end of an YSZ tube with YS2B glass paste (IRD Fuel Cell AS) and gold wires were attached to the current collectors for electrochemical measurements. This assembly was then enclosed with a quartz tube (Quark Glass) and placed inside a tube furnace. Optical access to the thin film electrode was maintained for Raman spectroscopic measurements and visual inspection. In this system, the cell was tested in a two-atmosphere environment at elevated temperatures. The laser power out of the spectrometer was 18 mW and this laser power was selected to give the best possible signal-to-noise ratio without causing damage to the samples. It is noted that due to

scattering losses from the optics the power was slightly lower at the electrode surface. During the *in operando* experiments, Raman spectra with 20 second exposure times were continuously collected to record changes in the surface species under applied potential.

Electrochemical Characterization. A potential was applied on the electrochemical cell using a Gamry Reference 600 potentiostat to record chronoamperometry curves. The applied potential difference was either -1 V or +1 V and the potential difference was predominantly across the thin film electrode, as the resistance of the porous LSC-CGO electrode was < 1% of the resistance of the LSM thin film electrode. This was experimentally confirmed by using electrochemical impedance spectroscopy to determine the polarization resistance on symmetric cells with two LSC-CGO electrodes and on cells with one LSC-CGO electrode and one LSM thin film electrode, respectively.

Overall Experimental Sequence. *In operando* Raman spectra were acquired from a BaO-modified LSM thin film cell during 15 individual polarization experiments that comprised a single overall experimental sequence. At the beginning of the sequence the cell was exposed to a constant gas flow of 10% O<sub>2</sub> in Ar and heated to 500 °C. When at 500 °C, the individual experiments were conducted at -1 V or +1 V. The temperature was then reduced to 300 °C and experiments were repeated. During the experimental sequence, the cell was constantly subjected to a gas flow containing 10% O<sub>2</sub>.

### X-ray Diffraction

For phase-determination on the screen-printed electrodes and synthesized Ba<sub>3</sub>Mn<sub>2</sub>O<sub>8</sub> (see next section), XRD measurements were performed at room temperature

with a Bruker D8 XRay Diffractometer (Bruker-Siemens, Germany) using Cu K $\alpha$  radiation with an acceleration voltage of 40 kV and a filament current of 40 mA. The recorded spectra were background corrected using the EVA software (Bruker), and the crystallographic database available in the EVA software was used to identify the present phases.

### Reference Material

During the course of the *in operando* Raman experiments, vibrational bands appeared that could not be assigned to the original materials. Consequently, several new ‘candidate’ materials were chosen for analysis and served as spectroscopic reference data. Many of these materials were available from traditional sources and/or spectra were already available from the literature. These materials included SrO,<sup>[287]</sup> La<sub>2</sub>O<sub>3</sub>,<sup>[288]</sup> Mn<sub>2</sub>O<sub>3</sub>,<sup>[289-291]</sup> Mn<sub>3</sub>O<sub>4</sub>,<sup>[289-291]</sup> MnO<sub>2</sub>,<sup>[289-291]</sup> MnO,<sup>[289]</sup> BaO,<sup>[292,293]</sup> and BaMnO<sub>3</sub>.<sup>[294]</sup> One material that was relatively poorly characterized by Raman spectroscopy was Ba<sub>3</sub>Mn<sub>2</sub>O<sub>8</sub>, which was synthesized in our own laboratory and characterized by XRD and Raman spectroscopy; see A1.2 for further information about synthesis and characterization of this material.

### Results

LSM thin film electrodes were characterized by ToF-SIMS and XPS before and after the *in operando* Raman spectroscopy. Results from the pre- and post-characterization are described below together with the *in operando* Raman spectroscopy

results. Furthermore, evidence of the secondary  $\text{Ba}_3\text{Mn}_2\text{O}_8$  phase in a conventional, porous LSM-CGO electrode is reported.

#### Pre-Characterization of LSM Thin Films

The LSM electrodes used in these studies had the nominal composition  $(\text{La}_{0.85}\text{Sr}_{0.15})_{0.9}\text{MnO}_{3\pm\delta}$ , where the LSM perovskite structure had a slight deficiency on the A-site. Four of these LSM thin films without BaO were characterized by means of ToF-SIMS and XPS. A representative ToF-SIMS depth profile for one of the thin films is shown in Figure 6.3, after the signal intensity for the individual elements has been corrected for the total signal intensity to minimize instrumental effects. The ToF-SIMS profile (Fig. 6.3) shows an approximately 25 nm thick surface layer of the LSM with a composition deviating from the bulk LSM composition (ToF-SIMS measurements have a depth resolution of  $\sim 2$  nm for these materials). Within this surface layer, Mn appears to be depleted and La enriched compared to the bulk values for LSM. Variation in the concentration profiles of individual elements is also observed throughout the layer (Fig. 6.3b). Compared to bulk LSM, Sr appears to be enriched within the 5 nm layer next to the gas-solid interface and depleted at depths from 5 nm to 25 nm. The Mn concentration within the first 5 nm next to the gas-solid interface shows a slight increase towards the interface but never exceeds the bulk value. Furthermore, the LaO concentration profile reaches a maximum at 7 nm's depth. Overall these distributions indicate the existence of two surface layers: a top layer dominated by Sr and Mn and an inner layer enriched in La. These findings agree with reports from similarly prepared electrodes.<sup>[295]</sup> We note that care must be taken when interpreting ToF-SIMS profiles on LSM electrodes, as matrix-

effect may cause artifacts to appear in the concentration profile.<sup>[295]</sup> For this reason the four LSM electrodes were analyzed by XPS to yield quantitative information on the electrode composition within a probe depth of 5-10 nm. The results from the XPS analysis of four LSM films are reported in Table 6.1, where the measured ratios between the elements are compared to the theoretical ratios. The XPS results are in agreement with the results from the ToF-SIMS depth profile and show enrichment in A-site cations (La, Sr) relative to the B-site cation (Mn), with the Sr enrichment being more pronounced than the La enrichment. Sr segregation on the surface of perovskites has been observed previously and is believed to influence the electrode performance, but the specific influence of Sr's enrichment at the electrode surface is still debated.<sup>[296,297]</sup> In conclusion, both XPS and ToF-SIMS show Sr enrichment at the LSM thin film surface, and the ToF-SIMS furthermore reveals that within a 25 nm surface layer of the LSM electrode the composition deviates from the bulk LSM composition.

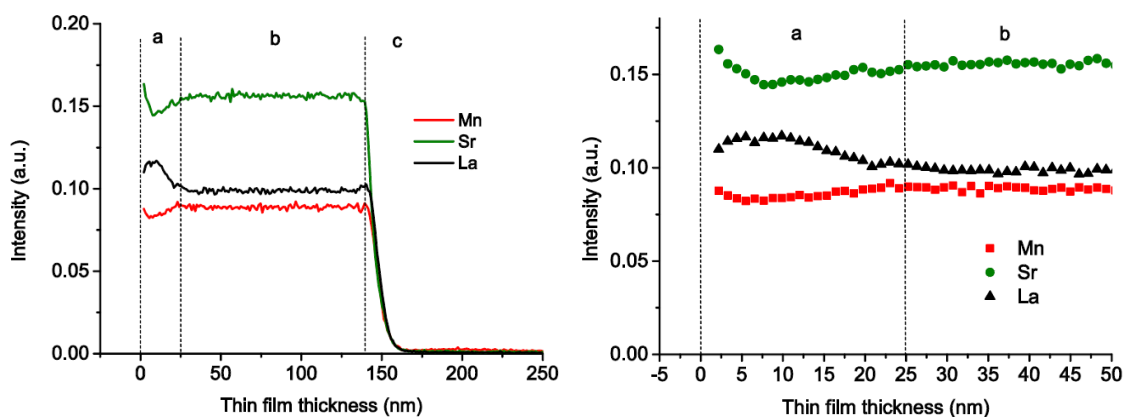


Figure 6.3. ToF-SIMS depth profile through un-tested LSM thin film, the entire thin film (left) and the 50 nm closest to the gas-solid interface (right). The letters state the following a) 25 nm thick LSM surface layer with composition different from the bulk electrode, b) bulk LSM electrode and c) CGO thin film below the LSM electrode. The intensity is proportional to the concentration of the elements.



Table 6.1. Ratio between metallic electrode elements in  $(\text{La}_{0.85}\text{Sr}_{0.15})_{0.9}\text{MnO}_{3\pm\delta}$  as synthesized and measured at the surface of 4 un-tested LSM thin films by XPS, probing depth 5-10 nm.

	As synthesized ratio	Measured ratio	Measured/As synthesized
Sr/La	0.176	$0.27 \pm 0.04$	1.53
Sr/Mn	0.135	$0.41 \pm 0.07$	3.04
La/Mn	0.765	$1.49 \pm 0.15$	1.95
(La+Sr)/Mn	0.9	$1.91 \pm 0.17$	2.12

### Post-Mortem Characterization of LSM Thin Film with BaO

The LSM thin film electrode with BaO was characterized by ToF-SIMS after the in operando Raman spectroscopy experiments. The depth profiles for the electrode elements show less well-defined electrode interfaces (Fig. 6.4) compared to the untested LSM-thin electrodes. This difference is ascribed to the sample preparation rather than being a result from the in operando experiments. The depth profile for the Ba shows diffusion of Ba from the surface through the entire LSM electrode.

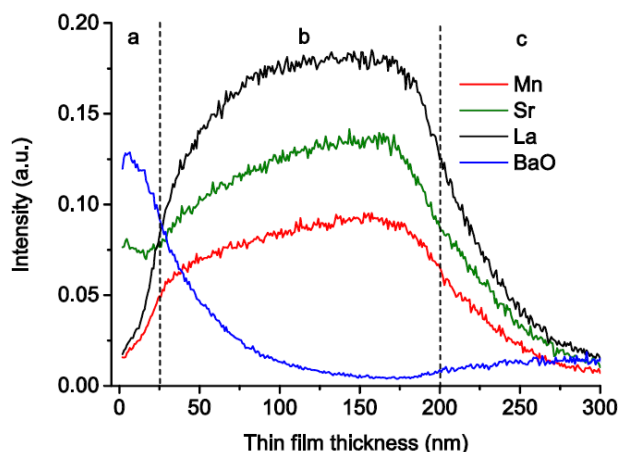


Figure 6.4. Post mortem ToF-SIMS depth profile through LSM thin film electrode impregnated with BaO. The letters state a) the surface layer, b) the bulk LSM electrode and c) the CGO thin film below the LSM electrode. The Ba depth profile shows diffusion of Ba into the LSM electrode.

### Presence of Ba<sub>3</sub>Mn<sub>2</sub>O<sub>8</sub> on BaO-Infiltrated LSM Electrodes

XRD data collected on BaO infiltrated porous LSM-CGO electrodes revealed a minor peak at 24.1° likely due to BaCO<sub>3</sub> (ICSD 91888) and three minor peaks in the diffraction pattern at 2θ locations of 27.7°, 31.4° and 42.2° (A1.3). These latter features correspond to the three dominant peaks of Ba<sub>3</sub>Mn<sub>2</sub>O<sub>8</sub> (ICSD 280045), one of the few compounds in which Mn is present in an oxidation state of +5. This material presumably formed during electrode processing since it was not present during the initial stages of fabrication. As Ba<sub>3</sub>Mn<sub>2</sub>O<sub>8</sub> is not commercially available, Ba<sub>3</sub>Mn<sub>2</sub>O<sub>8</sub> was synthesized according to the procedure described by Weller *et al.*, and characterized by XRD and Raman spectroscopy, the latter revealing two characteristic peaks at ~301 cm<sup>-1</sup> and 771 cm<sup>-1</sup>.<sup>[298]</sup> Details concerning Ba<sub>3</sub>Mn<sub>2</sub>O<sub>8</sub> synthesis are reported in A1.2 together with XRD and Raman data from the pure compound.

### Raman Spectroscopy

In the following sections, results from the Raman experiments are presented, including spectra recorded on thin model electrodes with and without BaO deposition. However at first a comparison between the porous LSM-CGO electrode and the thin film electrode is made.

#### Reproducibility between Porous LSM-CGO

Electrode and LSM Thin Film Model Electrode. Raman spectra recorded from a porous LSM-CGO electrode (A1.4) were consistent with the results from the thin film electrode with respect to the presence of Ba<sub>3</sub>Mn<sub>2</sub>O<sub>8</sub>. In contrast to the thin film electrode, presence of MnO<sub>x</sub> and BaCO<sub>3</sub> was not detected in the porous LSM-CGO though BaCO<sub>3</sub>

residues from the impregnation were detected on the edge of the porous electrode, as evidenced by stronger more well-defined  $690\text{ cm}^{-1}$  and  $1050\text{ cm}^{-1}$  peaks, and likely gave rise to the aforementioned weak  $\text{BaCO}_3$  signal in the XRD. The presence of  $\text{MnO}_x$  and  $\text{BaCO}_3$  on the pristine thin film electrode and not in the porous electrode is assigned to differences in the preparation method, and does not influence the conclusions drawn on  $\text{Ba}_3\text{Mn}_2\text{O}_8$  in this paper.

#### Similarities and Differences between Pure LSM

##### Electrodes and Electrodes with BaO Deposition. Representative *in situ* Raman

spectra collected from thin film LSM electrodes without and with BaO deposition exposed to 0.1 atm  $\text{O}_2$  in Ar at  $500\text{ }^\circ\text{C}$  are shown in Figure 6.5. Spectra recorded prior to polarization show clearly the compositional differences between electrodes. The most distinct vibrational feature for the pure LSM thin film electrode is a broad peak at  $610\text{ cm}^{-1}$ . Vibrational modes of both YSZ and  $\text{MnO}_x$  species are found in this region.<sup>[289,290,299,300]</sup> For cells with thin film electrodes, this feature may therefore arise from  $\text{MnO}_x$  on the electrode surface/within the electrode and/or from the YSZ substrate below the electrode. Cells with the screen printed LSM-CGO electrode (A1.4) did not contain YSZ but showed a similar peak around  $610\text{ cm}^{-1}$  that can result only from  $\text{MnO}_x$  species. The literature reports some discrepancy on peak assignments for the vibrational Raman modes of  $\text{MnO}_x$  species.<sup>[289,290]</sup> Some of this uncertainty can be attributed to material changes induced by exposure to high intensity fields including laser light.<sup>[289,301]</sup> Furthermore, the different phases of  $\text{MnO}_x$  all have vibrational features between  $570\text{-}690\text{ cm}^{-1}$ . Given these considerations and a preponderance of evidence in the

literature, the  $610\text{ cm}^{-1}$  peak is assigned tentatively to  $\text{MnO}_2$ .<sup>[289,291,302]</sup> This assignment is also consistent with XPS results by Backhaus-Ricoult *et al.* that showed Mn in an oxidation state of +4 on the un-polarized LSM surface.<sup>[269]</sup>

In contrast to the pure LSM thin film electrode, the BaO modified LSM thin film electrode exhibits several sharper bands in the Raman spectrum. Two features are observed consistently at  $306\text{ cm}^{-1}$  and  $773\text{ cm}^{-1}$  on the electrodes with BaO. The  $306\text{ cm}^{-1}$  and  $773\text{ cm}^{-1}$  peaks are assigned to a  $\text{Ba}_3\text{Mn}_2\text{O}_8$  secondary phase and are discussed in more detail below. In addition to these features, a peak at  $1051\text{ cm}^{-1}$  was observed and the intensity of this peak varied strongly with the position on the sample. Since MnO has peak at  $1050\text{ cm}^{-1}$  and  $\text{BaCO}_3$  a peak at  $1052\text{ cm}^{-1}$  the observed peak is tentatively assigned to one of these two species.<sup>[192,303]</sup>

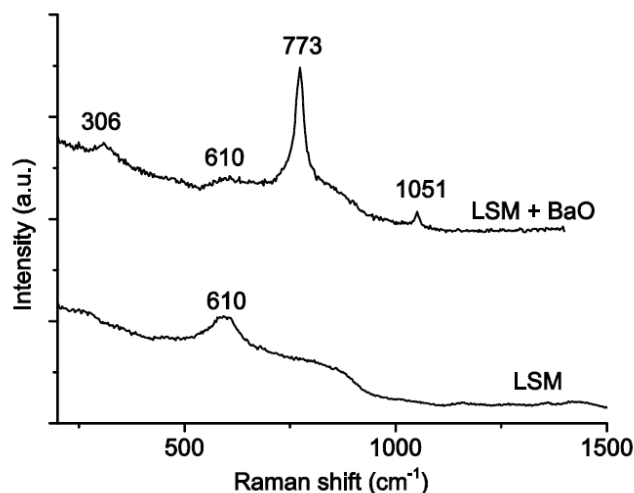


Figure 6.5. Representative Raman spectra recorded on a LSM thin film electrode with and without BaO infiltration at  $500\text{ }^{\circ}\text{C}$  in 10% oxygen flow. The top spectrum is displaced vertically to facilitate comparison.

Table 6.2 summarizes assignments for materials observed in the Raman spectra during the experiments on the thin films samples. All peaks were not present simultaneously, but depended on the sample and experimental conditions.

Table 6.2. Overview of all peaks observed in the Raman spectra recorded on the thin film samples; note all peaks may not be observed simultaneously.

Raman Shift (cm <sup>-1</sup> )	Assignment	Reference
306	Ba <sub>3</sub> Mn <sub>2</sub> O <sub>8</sub>	This work, see A1.2
610	YSZ	[299,300]
610 (broad and weak)	MnO <sub>x</sub> , most likely MnO <sub>2</sub>	[290,302,304]
644	MnO <sub>x</sub> , most likely Mn <sub>3</sub> O <sub>4</sub>	[289,290]
662	MnO <sub>x</sub> , most likely Mn <sub>2</sub> O <sub>3</sub>	[290]
690	BaCO <sub>3</sub>	[192,305]
771	Ba <sub>3</sub> Mn <sub>2</sub> O <sub>8</sub>	This work, see A1.2
1050	MnO	[303]
1052	BaCO <sub>3</sub>	[192]

#### Effect of Applied Potential on Electrode Surface Composition. *In operando*

Raman measurements were performed to investigate how electrode composition changed as a function of applied potential and temperature. Experimental parameters are summarized in Table 6.3. With two exceptions, measurement series were conducted at least twice for each combination of parameters to confirm the reproducibility of the results. In general, the chronoamperometry curves recorded during cathodic polarizations showed a small deactivation during the first ~600 seconds, resulting in a 10-20% decrease in the current density, (see A1.5). After these initial changes, the current density stayed stable indicating the electrode did not suffer further degradation during the experiments.

Table 6.3. The parameters used during the *in operando* Raman characterization.

Parameter	Values
Atmosphere	0.1 atm O <sub>2</sub> in Ar
Temperature	300 °C, 500 °C
Applied voltage	OCV, -1 V, +1 V

The following section describes how the chemical species detected with Raman spectroscopy were influenced by operational conditions. Raman spectra recorded at 500 °C prior to, during and after cathodic polarization of -1 V are shown in Figure 6.6a and Figure 6.6b together with the corresponding changes in selected peak intensities plotted in Figure 6.6c. Finally, Figure 6.7 shows a peak intensity plot for a similar experiment conducted at 500 °C; however, in this case the cell polarization was switched to +1 V immediately after the -1 V polarization. Electrodes exhibited consistent qualitative behaviors with respect to polarization at 300 °C and 500 °C. Spectra from the electrode operating at 300 °C are reported in A1.6.

**Ba<sub>3</sub>Mn<sub>2</sub>O<sub>8</sub>:** The formation and decomposition of Ba<sub>3</sub>Mn<sub>2</sub>O<sub>8</sub> was characterized by reversible increases or decreases, respectively, of the 306 cm<sup>-1</sup> and 773 cm<sup>-1</sup> peak intensities. Raman spectra showed that in a 0.1 atm O<sub>2</sub> environment, the Ba<sub>3</sub>Mn<sub>2</sub>O<sub>8</sub> vibrational band intensity diminished during cathodic polarization at -1 V (Fig. 6.6 and Fig. 6.7) and increased to an asymptotic limit during anodic polarization at +1 V (Fig. 6.7). Similarly, when the cell was held at OCV after cathodic polarization, the Ba<sub>3</sub>Mn<sub>2</sub>O<sub>8</sub> peak intensities increased (Fig. 6.6c), but at a slower rate compared to the increase observed during anodic polarization. Taken together, these observations show that the amount of the Ba<sub>3</sub>Mn<sub>2</sub>O<sub>8</sub> secondary phase in an infiltrated electrode depends

strongly on the applied potential, in this case ranging from almost full decomposition at cathodic polarization to full regeneration at OCV or anodic polarization.

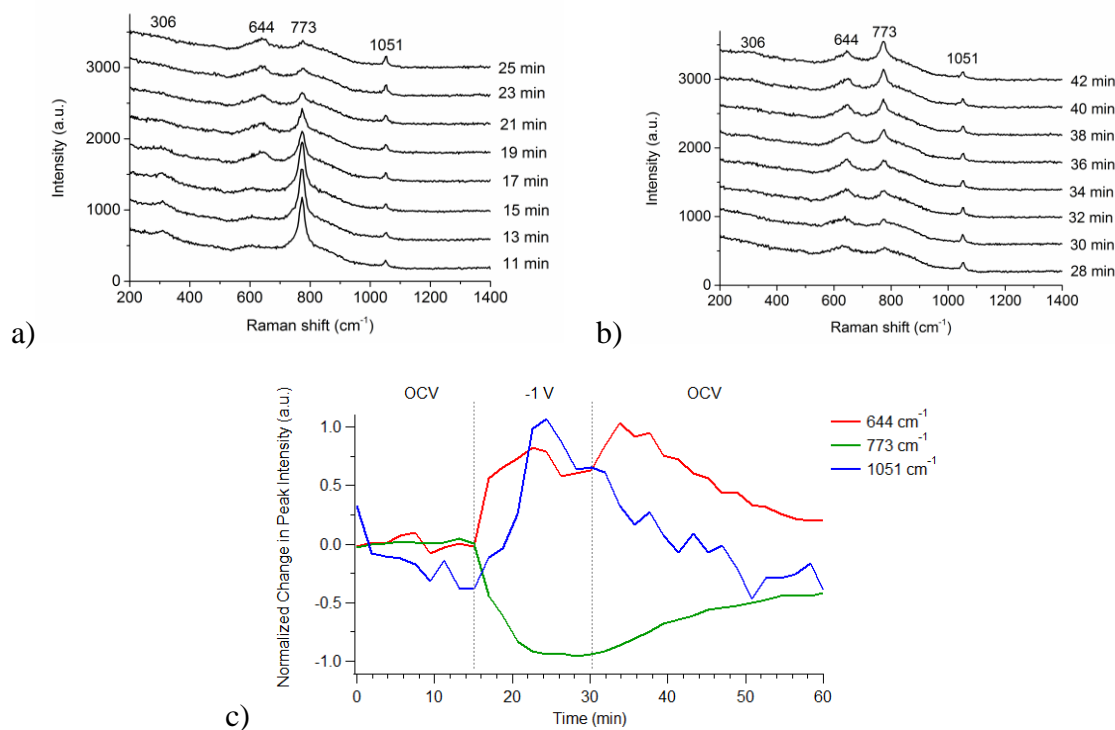


Figure 6.6. Raman spectra on BaO infiltrated LSM thin film electrode at 500 °C with 10% O<sub>2</sub>: (a) before and during the onset of -1 V, (b) at -1 V followed by OCV, and (c) the normalized peak intensity plot for the data set shown in (a) and (b).

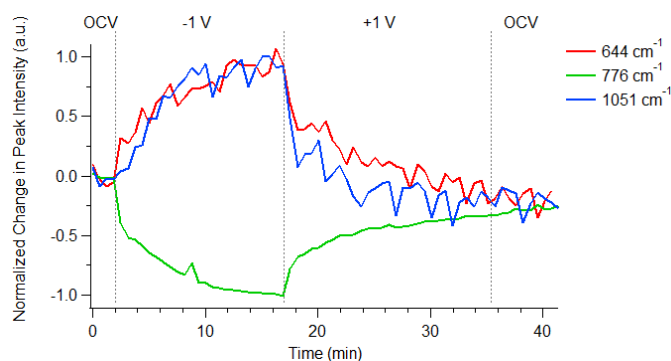


Figure 6.7. Peak intensity plot from Raman spectra on BaO infiltrated LSM thin film electrode at 500 °C with 10% O<sub>2</sub> during -1 V polarization followed immediately by +1 V polarization.

MnO<sub>x</sub>: In addition to the MnO<sub>2</sub> peak at 610 cm<sup>-1</sup>, a broad vibrational band was observed at approximately 644 cm<sup>-1</sup>. Contrary to the behavior observed for the 773 cm<sup>-1</sup> feature assigned to Ba<sub>3</sub>Mn<sub>2</sub>O<sub>8</sub>, the signal at 644 cm<sup>-1</sup> *increased* upon cathodic polarization of the electrode (Fig. 6.6 and Fig. 6.7). This feature is most likely a signature of Mn<sub>3</sub>O<sub>4</sub> given literature reports of a dominant band at 650 cm<sup>-1</sup> in spectra collected at room temperature.<sup>[289,290]</sup> Furthermore, these prior studies have also shown that MnO<sub>2</sub> and Mn<sub>2</sub>O<sub>3</sub> may be converted into Mn<sub>3</sub>O<sub>4</sub> due to localized heating from the laser excitation source used for the Raman measurements.<sup>[289,290,301,306]</sup> In Figure 6.6c and Figure 6.7 the formation of Mn<sub>3</sub>O<sub>4</sub> is anticorrelated with the loss of Ba<sub>3</sub>Mn<sub>2</sub>O<sub>8</sub>. These results suggest that Ba<sub>3</sub>Mn<sub>2</sub>O<sub>8</sub> decomposition is a dominant source for the observed Mn<sub>3</sub>O<sub>4</sub> formation. The Mn<sub>3</sub>O<sub>4</sub> expulsion from the LSM electrode itself during cathodic polarization cannot be excluded either, since the peak intensity plots occasionally show an increase in the Mn<sub>3</sub>O<sub>4</sub> occurring faster than the decrease in the Ba<sub>3</sub>Mn<sub>2</sub>O<sub>8</sub> signal (see A1.7). We propose that under reducing conditions, the Ba<sub>3</sub>Mn<sub>2</sub>O<sub>8</sub> (where Mn is in a +5 oxidation state) decomposes into Mn<sub>3</sub>O<sub>4</sub> (with mixed Mn<sup>2+</sup>/Mn<sup>3+</sup> character). The resulting Ba-containing material eluded detection in these experiments and in this connection, it is noted the absence of CO<sub>2</sub> in the gas flow make generation of BaCO<sub>3</sub> unlikely. A change in the 1051 cm<sup>-1</sup> peak was observed upon polarization as the peak increased during cathodic polarization and decreased during subsequent OCV and anodic polarization (Fig. 6.6 and Fig. 6.7). However, this increase in intensity was only observable when the 1051 cm<sup>-1</sup> was either small or non-existent prior to the polarization. If a large, dominant peak at 1051 cm<sup>-1</sup> was present in spectra before the polarization, no



effect of cathodic polarization was observed, yet a decrease was still observed during anodic polarization (see A1.6). This result is explained by the coincidence between the  $\text{BaCO}_3$  peak at  $1052\text{ cm}^{-1}$  and the  $\text{MnO}$  peak at  $1050\text{ cm}^{-1}$ , as the strong  $\text{BaCO}_3$  peak occasionally overshadowed changes in the weak  $\text{MnO}$  peak. The  $\text{BaCO}_3$  was not affected during cathodic polarization, but partly oxidized during anodic polarization. The  $\text{MnO}$  was formed during cathodic polarization and removed during anodic polarization. The correlation between the polarization induced changes in the  $\text{MnO}_x$  species and the  $\text{Ba}_3\text{Mn}_2\text{O}_8$  will be discussed further on the “Discussion” section.

The transformations observed with cathodic polarizations were reversible. Once the cathodic polarization was removed, the vibrational signature for  $\text{Ba}_3\text{Mn}_2\text{O}_8$  began to reappear (Fig. 6.6b and Fig. 6.6c), eventually approaching its original intensity prior to the -1V polarization. Changing the bias immediately from -1 V to +1 V accelerated the regeneration of  $\text{Ba}_3\text{Mn}_2\text{O}_8$  (Fig. 6.7). Interestingly, when the cathodic polarization (-1 V) was changed to OCV, the  $\text{Ba}_3\text{Mn}_2\text{O}_8$  began to grow back immediately, albeit slowly, while the  $\text{Mn}_3\text{O}_4$  signal continued to increase for several minutes before eventually returning to pre-cathodic polarization levels (Fig. 6.6c). The continued growth of the  $\text{Mn}_3\text{O}_4$  signal after the cathodic polarization was removed is ascribed to re-oxidation of  $\text{MnO}$  and is discussed below.

Finally, we note that all of the spectroscopic measurements show that material changes happen on the order of minutes or tens of minutes when the cell is polarized at  $300\text{ }^\circ\text{C}$  or  $500\text{ }^\circ\text{C}$ , with the most dramatic material changes occurring within the first 5 minutes. Thus, *ex situ* techniques or *in situ* measurements without sufficient temporal

resolution will not be able to resolve compositional changes occurring in these high temperature materials during operation.

## Discussion

### Electrode Surface Composition at OCV Conditions

BaO infiltration of LSM electrodes has in previous work, based on electrochemical impedance spectroscopy at OCV conditions, been reported to cause a significant decrease in the polarization resistance.<sup>[36,281,282]</sup> The aim in the present study is to investigate the reason for this decrease, which, depending on reaction conditions and sample preparation, may be as large as an order of magnitude.<sup>[36,281,282]</sup> Raman spectroscopy performed with electrodes at OCV revealed the presence of Ba<sub>3</sub>Mn<sub>2</sub>O<sub>8</sub> on the BaO infiltrated LSM electrodes to be the only consistent difference between infiltrated and non-infiltrated electrodes. For this reason Ba<sub>3</sub>Mn<sub>2</sub>O<sub>8</sub> is suggested to cause the reduced polarization resistance at OCV observed when LSM electrodes are infiltrated with BaO. Unfortunately there are to the best of the author's knowledge no reports in literature on the electrical properties of Ba<sub>3</sub>Mn<sub>2</sub>O<sub>8</sub>. However, work described by Roos *et al.* may provide insight into the electrical properties of Ba<sub>3</sub>Mn<sub>2</sub>O<sub>8</sub> since Roos *et al.* explain manganese ions in tetrahedral coordination as in Ba<sub>3</sub>Mn<sub>2</sub>O<sub>8</sub> can easily change from Mn<sup>5+</sup> to Mn<sup>4+</sup> and from Mn<sup>4+</sup> to Mn<sup>3+</sup>, which may contribute to the observed enhancement of the electrode's electrocatalytic properties.<sup>[307]</sup> The suggestion that Ba<sub>3</sub>Mn<sub>2</sub>O<sub>8</sub> causes the reduced polarization resistance at OCV is made with the reservation that for each reporting in the literature, both the amount of Ba infiltrate and

the LSM stoichiometry play a role in secondary phase formation and the possible formation of  $\text{BaCO}_3$ , which may also influence the electrocatalytic properties.<sup>[281]</sup> However, regardless of the impregnation method and materials choice, electrodes in a real application are subjected to electrical polarization, for which reason the effect of cathodic and anodic polarization on the BaO infiltrated LSM electrode was investigated in this study.

### Electrical Polarization and Electrode Surface Composition

The *in operando* Raman spectra presented in Figure 6.6 and Figure 6.7 demonstrate clearly that the surfaces of a BaO-infiltrated LSM-electrode are dynamic and significantly affected by an applied polarization. The discussion below focuses on how the dominant species on the electrode surface,  $\text{Ba}_3\text{Mn}_2\text{O}_8$  and  $\text{MnO}_x$ , are affected by the applied reaction conditions.

$\text{Ba}_3\text{Mn}_2\text{O}_8$ : Under 0.1 atm  $\text{O}_2$  in Ar,  $\text{Ba}_3\text{Mn}_2\text{O}_8$  showed a strong dependence on the applied electrical polarization where cathodic polarization promoted decomposition and anodic polarization promoted the regeneration of  $\text{Ba}_3\text{Mn}_2\text{O}_8$  on the LSM electrode. Cathodic polarization has the same effect on LSM electrodes as very low oxygen partial pressures, a condition that promotes the formation of oxygen vacancies.<sup>[308]</sup> Continued exposure to high cathodic polarization conditions and/or low the oxygen partial pressure ultimately leads to decomposition of LSM electrodes and will also decompose complex oxides like  $\text{Ba}_3\text{Mn}_2\text{O}_8$ .<sup>[309-311]</sup> The Ba-Mn-O diagram (Fig. 6.8) shows that the total oxide content in the  $\text{Ba}_3\text{Mn}_2\text{O}_8$  only needs to decrease 4% for the material to transform into a

different stoichiometric compound.<sup>[312]</sup> Furthermore, the diagram reveals that if the oxide content is reduced by 4-5% a region is reached in which several Ba-Mn-O and Mn-O compounds can coexist, which corresponds well with the increase in different  $\text{MnO}_x$  species observed on the electrode surface during cathodic polarization in this study.

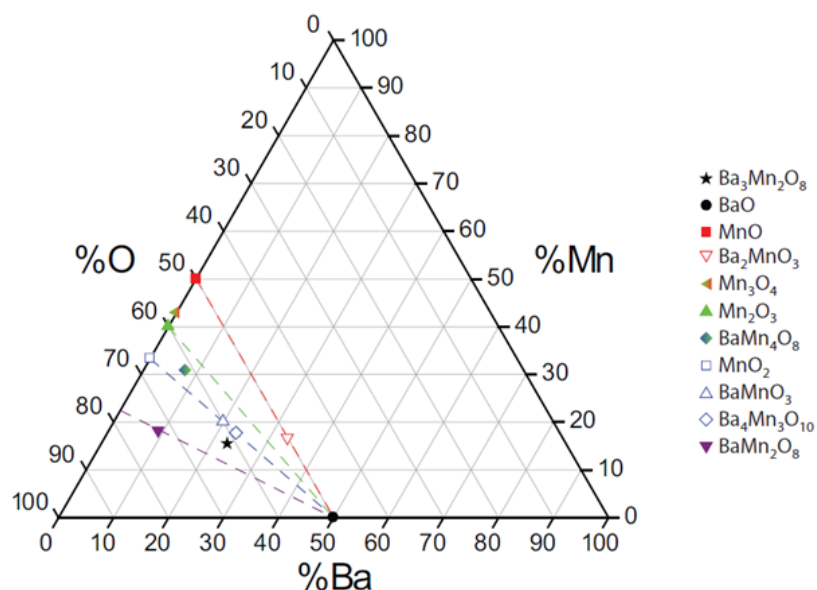


Figure 6.8. Ba-Mn-O ternary diagram showing  $\text{Ba}_3\text{Mn}_2\text{O}_8$  (black star) and other phases. Compounds with the Mn Valence of +2 (red), +3 (green), +4 (blue), and +7 (purple) are grouped by color and connected by dashed lines, while compounds with mixed Mn valence have a gradient between the colors representing the two different valences. The diagram is re-printed from the dissertation thesis of Eric C. Samulon.<sup>[312]</sup>

$\text{MnO}_x$ . The *in operando* Raman spectra show that the amount of  $\text{Mn}_3\text{O}_4$  on the electrode surface increased significantly during cathodic polarization and decreased during anodic polarization. We propose that the dominant source of the  $\text{Mn}_3\text{O}_4$  is  $\text{Ba}_3\text{Mn}_2\text{O}_8$  given that during the majority of the polarizations the intensity of the  $\text{Ba}_3\text{Mn}_2\text{O}_8$  and the  $\text{Mn}_3\text{O}_4$  Raman signal appear directly anti-correlated. Expulsion of  $\text{Mn}_3\text{O}_4$  from the LSM electrode itself during cathodic polarization may also be a minor

source for  $\text{Mn}_3\text{O}_4$ , as expulsion of  $\text{Mn}_3\text{O}_4$  from LSM previously has been observed *ex situ* by XRD on LSM samples sintered at low oxygen partial pressure ( $p\text{O}_2=10^{-6}$  atm).<sup>[311]</sup> Furthermore expulsion of  $\text{MnO}/\text{Mn}_3\text{O}_4$  has been reported on LSM and lanthanum manganite electrodes during cyclic voltammetry.<sup>[310]</sup> *Ex situ* ToF-SIMS studies of LSM microelectrodes have also revealed a strong, *irreversible* redistribution of the Mn from the electrode onto the electrolyte after electrical polarization.<sup>[295]</sup> *In situ* studies of manganese redistribution on LSM electrodes are scarce. Among the few literature reports is work by Backhaus-Ricoult *et al.*, who detected polarization induced reduction and migration of Mn-species onto the electrolyte by XPS under conditions approximating those employed in solid oxide fuel cell systems.<sup>[269]</sup> Results from the *in operando* Raman measurements generally agree with findings from the aforementioned studies in terms of the capability of a cathodic polarization to re-distribute Mn in/on the LSM electrode. However, the Raman data imply  $\text{Mn}_3\text{O}_4$  enrichment during cathodic polarization whereas the *in situ* XPS study showed Mn depletion at the electrode surface during cathodic polarization.<sup>[269]</sup> The discrepancy is likely explained by a combination of: (1) the presence of  $\text{Ba}_3\text{Mn}_2\text{O}_8$  that acts as a  $\text{Mn}_3\text{O}_4$  source in this work, (2) Backhaus-Ricoult using stoichiometric  $\text{La}_{0.8}\text{Sr}_{0.2}\text{MnO}_3$  while the present study employed A-site deficient  $(\text{La}_{0.85}\text{Sr}_{0.15})_{0.9}\text{MnO}_{3\pm\delta}$ , and/or (3) diffusion of Ba-ions into the LSM, as evident from the ToF-SIMS characterization (Fig. 6.4) altering cation segregation mechanism(s).<sup>[269]</sup>

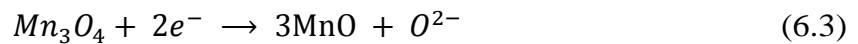
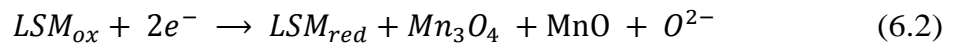
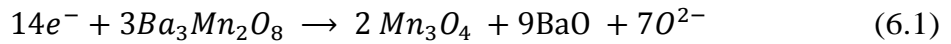
One interesting observation of  $\text{Mn}_3\text{O}_4$  observed *in operando* considers the behavior of  $\text{Mn}_3\text{O}_4$  at OCV following cathodic polarization. After the Raman signal from  $\text{Mn}_3\text{O}_4$  increases and stabilizes during cathodic polarization, the  $\text{Mn}_3\text{O}_4$  increases even

further during the first 3-5 minutes at OCV *after* the polarization has been removed at 500 °C (Fig. 6.6). These observations appear contradictory, namely that applying a cathodic polarization causes an increase in the  $\text{Mn}_3\text{O}_4$  signal, and the removal of the cathodic polarization is accompanied by a  $\text{Mn}_3\text{O}_4$  signal intensity that increases even further. A plausible explanation of this phenomenon hinges on the labile nature of  $\text{Mn}^{n+}$ . In  $\text{Ba}_3\text{Mn}_2\text{O}_8$ , Mn has a formal oxidation state of 5+. Under cathodic polarization of -1 V, Raman spectra show that reduced forms of Mn (i.e.  $\text{Mn}^{3+}$  and  $\text{Mn}^{2+}$ ) become more prevalent, given the growth of vibrational signatures at  $644\text{ cm}^{-1}$  ( $\text{Mn}_3\text{O}_4$ ) and  $1050\text{ cm}^{-1}$  ( $\text{MnO}$ ). When the bias is removed or reversed, thermodynamic considerations will once again favor more oxidized forms of Mn, leading eventually to the fully recovered amount of  $\text{Mn}^{5+}$  in  $\text{Ba}_3\text{Mn}_2\text{O}_8$ . Given the availability of mobile oxide ions, we propose that as  $\text{MnO}$  begins to oxidize,  $\text{Mn}_3\text{O}_4$  forms as an intermediate species on a path that ultimately results in  $\text{Ba}_3\text{Mn}_2\text{O}_8$  and accounts for the growth in the  $644\text{ cm}^{-1}$  Raman band after the cell polarization returns to OCV from -1 V. When the bias is reversed from -1V to +1V, the kinetics of such a transformation would simply be too fast for experiments to report the  $\text{Mn}_3\text{O}_4$  intermediate growth. This hypothesis is supported by a weak decrease in  $\text{Mn}_3\text{O}_4$  signal at the end of the cathodic polarization (Fig. 6.6c).

Finally, an additional observation associated with  $\text{MnO}_x$  segregation on the electrode surface is that the segregation was only observed on LSM electrodes with BaO. A number of LSM thin film electrodes without BaO deposition were subjected to various treatments, including higher temperatures (700 °C) and stronger polarizations (-2.5V) than those applied to the BaO modified electrodes.<sup>[256]</sup> Despite these more extreme

conditions, an increase in the amount of  $Mn_3O_4$  was not observed with Raman spectroscopy during any of the polarizations.<sup>[256]</sup> The fact that changes in  $Mn_3O_4$  were not observed on the pure LSM electrodes suggests that the  $Ba_3Mn_2O_8$  secondary phase is a dominant source for  $Mn_3O_4$  formation, although Ba diffusion into the LSM electrode (Fig. 6.4) can have influenced Mn segregation. Regarding the amount of Ba, which can be accommodated in LSM, experiments have shown that lanthanum manganites are stable with up to 40% substitution of Ba on the La site.<sup>[313]</sup> However, a recent study of lanthanum manganite thin films has shown that the maximum substitution level is strongly dependent on temperature and oxygen partial pressure.<sup>[314]</sup>

The  $Ba_3Mn_2O_8$  secondary phase on LSM electrodes infiltrated with BaO was most likely formed via a reaction with excess  $MnO_x$  in the electrode. The behavior of this secondary phase and of  $MnO_x$  phases during polarization has been discussed above, and in Eq. (6.1)-(6.3) the proposed cathode reactions are summarized.



So far it has been suggested that  $Ba_3Mn_2O_8$  is responsible for the reduced polarization resistance observed on the BaO infiltrated LSM electrodes at OCV conditions. Furthermore, the removal of  $Ba_3Mn_2O_8$  and the associated changes in the electrode surface composition during cathodic polarization have been thoroughly discussed. Still unresolved is how these compositional changes during polarization influence electrode performance. A common issue in LSM electrodes and other

perovskite based electrodes is passivation of the electrode surface due to segregation of Sr and impurities to the surface.<sup>[297]</sup> We suggest that reduction of  $\text{Ba}_3\text{Mn}_2\text{O}_8$  releasing  $\text{Mn}_3\text{O}_4$  and  $\text{MnO}$  onto the electrode surface will increase the electrochemical activity. This suggestion is based on literature reportings showing decreased polarization resistance in oxygen atmospheres on LSM electrodes infiltrated with  $\text{MnO}_x$  or Pt-YSZ electrodes modified with Mn-species.<sup>[315-317]</sup> Since very limited reports are made on the electrocatalytic properties of  $\text{MnO}_x$ , further experiments are needed to test the hypothesis that the release of  $\text{Mn}_3\text{O}_4$  and/or  $\text{MnO}$  on the electrode surface increases the electrochemical activity of the BaO infiltrated electrodes during operation.

### Conclusion

The experiments on BaO modified LSM electrodes described in this work were conducted to explore how the addition of BaO affects the LSM electrodes' electrocatalytic properties, particularly as an  $\text{O}_2$  reduction catalyst. The enhanced electrocatalytic properties caused by the BaO modification is, based on this work, at OCV conditions ascribed to formation of a secondary  $\text{Ba}_3\text{Mn}_2\text{O}_8$  phase. During cathodic polarization a significant redistribution of elements in the electrode surface takes place, as the  $\text{Ba}_3\text{Mn}_2\text{O}_8$  phase decomposes and  $\text{MnO}_x$  species accumulates in the electrode surface. The redistributions are reversible with polarization, thus the electrode returns to the original state when polarized in the anodic direction or returned to OCV. These reversible changes illustrate that element or material specific techniques must be applied *in operando*, to envisage the active state during operation of an infiltrated LSM electrode, or any other solid electrode prepared infiltration. Knowing the exact electrode



composition during operation is a crucial prerequisite for understanding why the widespread use of infiltration in electrode preparation improves the electrocatalytic properties of solid electrodes. Another consequence of results reported herein is recognition that compounds such as  $\text{Ba}_3\text{Mn}_2\text{O}_8$  that include a highly oxidized transition metal can serve as a “storage” compound for the transition metal until polarization is applied and the transition metal having high electrocatalytic activity is “released” or redistributed onto the electrode surface. Further research is however needed in order to explore this intriguing concept in more detail.

#### Acknowledgements

M. L. Traulsen gratefully acknowledges support from the Danish Independent Research Council - Technology and Production (12-131965). R. A. Walker gratefully acknowledges support from the U.S. Office of Naval Research (N000141410326). M. D. McIntyre gratefully acknowledges support from the U.S. National Science Foundation Division of Material Research (1411210).

## CHAPTER SEVEN

## CONCLUDING REMARKS

Conclusions

The studies presented throughout this dissertation demonstrate the efficacy of *in operando* Raman spectroscopy to directly identify material changes in solid oxide fuel cell (SOFC) electrodes. This technique is especially valuable for investigating the catalytically active or inactive role of dopants and secondary phases in mechanisms responsible for enhanced performance. The information obtained from *in operando* Raman spectroscopy studies can aid in selecting materials for optimal SOFC performance at lower operating temperatures.

For example, Chapter 6 has shown that the  $\text{Ba}_3\text{Mn}_2\text{O}_8$  secondary phase improves the electrocatalytic activity of LSM electrodes under OCV conditions at 500 °C. The reduced resistance for oxygen reduction under cathodic polarization conditions is associated with the reversible decomposition of  $\text{Ba}_3\text{Mn}_2\text{O}_8$  and formation of  $\text{MnO}_x$  species on LSM electrodes. These results bring up questions about the electrochemical activity of  $\text{MnO}_x$  species and whether or not these species form on LSM electrodes doped with other chemical species such as  $\text{KNO}_3$ .<sup>[315]</sup>

Although lower operating temperatures will slow the thermal coarsening of Ni particles, modification of Ni-YSZ anodes is required to prevent thermal coarsening and therefore improve the longevity and durability of the cermet.<sup>[59,318]</sup> One common strategy to suppress thermal coarsening is doping Ni-YSZ with materials such as  $\text{TiO}_2$ ,  $\text{Al}_2\text{O}_3$ , and

$\text{Al}_2\text{TiO}_5$  (ALT).<sup>[59,60,228,319]</sup> Chapter 5 showed that at typical SOFC processing temperatures ( $> 1000^\circ\text{C}$ )  $\text{TiO}_2$  will react with YSZ to form the mixed ion-electron conducting  $\text{Zr}_5\text{Ti}_7\text{O}_{24}$  phase.<sup>[320]</sup> The presence of this phase in  $\text{TiO}_2$  or ALT doped Ni-YSZ anodes may contribute to the enhanced performance.<sup>[60,228,230]</sup> Currently, we are investigating ALT doped anodes and the secondary phases formed in these cermets during fabrication processes.<sup>[60]</sup> Our most recent studies of  $\text{Al}_2\text{O}_3$  infiltrated Ni-YSZ anodes show the  $\text{NiAl}_2\text{O}_4$  secondary phase forms during anode fabrication process (Fig. 7.1a) and reduces into  $\text{Al}_2\text{O}_3$  decorated Ni particles under  $\text{H}_2$  at  $800^\circ\text{C}$  (Fig. 7.1b). The infiltrated cells had higher performance and less Ni coarsening than cells with pure Ni-YSZ anodes. These results are promising and warrant future experiments with carbon-containing fuels.

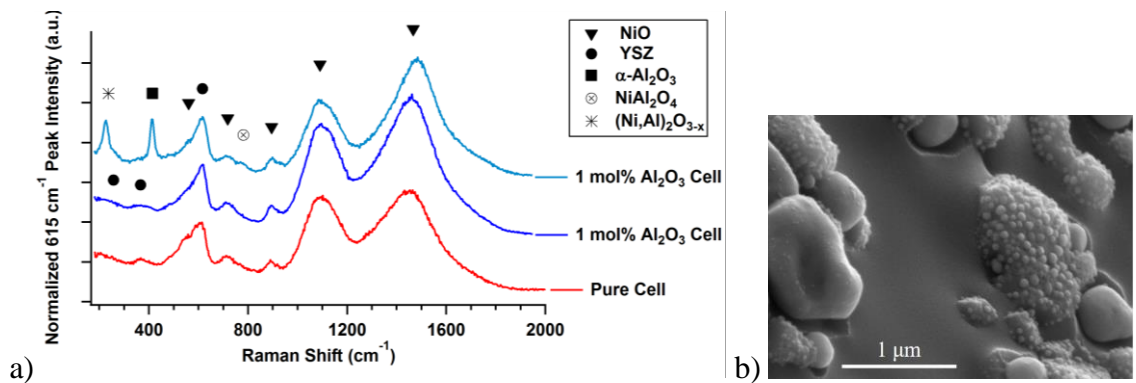


Figure 7.1. (a) Room temperature Raman spectra of pure and  $\text{Al}_2\text{O}_3$  infiltrated Ni-YSZ. (b) SEM image of  $\text{Al}_2\text{O}_3$  infiltrated Ni on a YSZ substrate following reduction with  $\text{H}_2$  at  $800^\circ\text{C}$ .

Conversely, Ni-YSZ anodes infiltrated with BaO or Sn are used to reduce carbon accumulation with carbon-based fuels; metal sintering in these cermets remains to be investigated.<sup>[47,48,129,208,321]</sup> Chapter 4 demonstrated that carbon accumulation with  $\text{CH}_4$

fuel is suppressed in BaO infiltrated and Sn infiltrated Ni-YSZ anodes.<sup>[129]</sup> *In situ* Raman spectroscopy and electrochemical measurements of these SOFCs suggest a heterogeneous distribution of carbon throughout the cermets where carbon accumulated in the electrochemically active region of the anodes closest to the electrolyte. The spectroscopic and electrochemical data revealed that BaO promoted carbon oxidation and was the more effective at mitigating carbon accumulation than Sn infiltrated anodes. In addition to carbon formation processes, this study showed that carbon could be removed from the anode via oxidation with H<sub>2</sub>O, CO<sub>2</sub>, or O<sub>2</sub> reforming agents. H<sub>2</sub>O was the most efficient reforming agent at carbon removal with O<sub>2</sub> and CO<sub>2</sub> taking ~3 and ~6 times longer, respectively.

Studies of carbon accumulation with *syn-gas* are needed since this fuel mixture can be produced from a variety of fuel sources such as biomass, coal gasification, methane reforming and exhaust from solid oxide electrolysis cells (operating with CO<sub>2</sub>/H<sub>2</sub>O mixtures).<sup>[4,105,109]</sup> Thus, understanding carbon formation/oxidation mechanisms with *syn-gas* mixtures is pertinent as *syn-gas* is one of the most accessible and abundant fuels. Both the fuel source and fuel reforming parameters affect *syn-gas* composition. Chapters 2-3 focused on 50%CO:50%H<sub>2</sub> *syn-gas* mixtures and demonstrated reduced carbon accumulation with higher operating temperatures and polarization conditions.<sup>[127,322]</sup> An interesting correlation between spectroscopic and electrochemical measurements revealed that low level of carbon helped to stabilize cell potential at all temperatures. Although several publications have proposed that carbon could help improve connectivity, the results presented in this dissertation are, to the best

of my knowledge, the first studies to show directly carbon growth, as evidenced in the *in operando* Raman spectra, coinciding with a stabilization of the cell's electrical output.

Collectively, the studies presented in this dissertation highlight the versatility of *in operando* Raman spectroscopy to investigate the surface chemistry in high temperature electrocatalysts and materials used for energy conversion. The spectroscopic and electrochemical data obtained from these experiments provide valuable information that directly identifies material and compositional changes with enhanced electrocatalytic activity and overall SOFC performance. These results can be used to develop and refine fabrication processes and develop operational protocols that will aid in the transition to zero-emission energy production/generation.

### Future Directions

#### Operation of SOFCs with *Syn-gas* Mixtures

Although excessive carbon accumulation is deleterious to Ni-YSZ, Chapters 2-3 have shown that low levels of carbon accumulation with a 50/50 CO/H<sub>2</sub> *syn-gas* mixture can help improve connectivity in cermet anodes. This result brings up important questions about how carbon accumulation is affected by *syn-gas* composition and operational temperature. Future experiments would vary gas compositions such as CO/H<sub>2</sub>, CO<sub>2</sub>/CO/H<sub>2</sub>, and CO<sub>2</sub>/CO/H<sub>2</sub>/H<sub>2</sub>O with each at various temperatures. Subsequent *syn-gas* experiments would be conducted with Sn or BaO infiltrated Ni-YSZ to evaluate how well these anodes suppress carbon.

### ALT Ni-YSZ Studies

Currently, studies exploring the mechanisms responsible for the improved performance and stability of ALT doped Ni-YSZ anodes have focused on  $\text{ZrO}_2\text{-TiO}_2$  and  $\text{Al}_2\text{O}_3\text{-Ni-YSZ}$  systems. Future studies of the  $\text{TiO}_2\text{-Ni-YSZ}$  system need to be conducted in order to evaluate how  $\text{Al}_2\text{O}_3$  and  $\text{TiO}_2$  each affect Ni-YSZ and whether or not the enhancement for the ALT doped anode is a synergistic effect. Additional studies would include reduction/oxidation cycling the anodes as well as the *syn-gas* experiments described above to see if carbon accumulation is suppressed in these cermets.

APPENDIX A

SUPPORTING INFORMATION FOR CHAPTER 6

### Supporting Information

#### A1.1. SEM Image of Thin Film Electrode

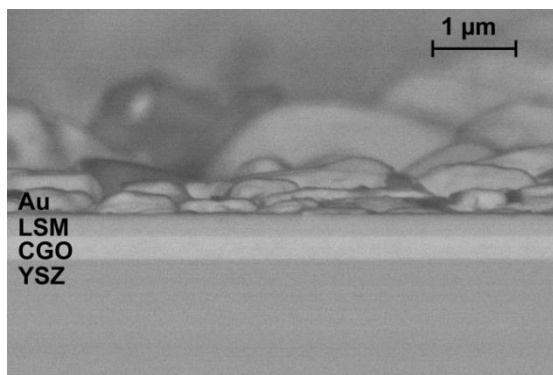


Figure A1.1. SEM image of broken cross-section of an electrochemical thin film model cell, showing (from top to bottom) the sputtered Au layer, LSM thin film, CGO thin film and YSZ electrolyte.

#### A1.2. Synthesis and Characterization of $\text{Ba}_3\text{Mn}_2\text{O}_8$

One material that was relatively poorly characterized in Raman spectroscopy literature was  $\text{Ba}_3\text{Mn}_2\text{O}_8$ . Consequently,  $\text{Ba}_3\text{Mn}_2\text{O}_8$  was synthesized according to the procedure described by Weller *et al.* for subsequent Raman characterization.<sup>[298]</sup> First, stoichiometric amounts of  $\text{BaCO}_3$  (Sigma-Aldrich) and  $\text{Mn}_2\text{O}_3$  (Sigma-Aldrich) were mixed in ethanol for 6 h on a ball-mill. The mixture was then dried, transferred to a crucible and heated to 900 °C under flowing air for 24 h. The sample was air-quenched from 900 °C directly to room temperature. XRD measurements after the synthesis showed a nearly pure phase of  $\text{Ba}_3\text{Mn}_2\text{O}_8$  with only very minor phase impurities from  $\text{BaMnO}_3$  and  $\text{BaCO}_3$  (Fig. A1.2a).



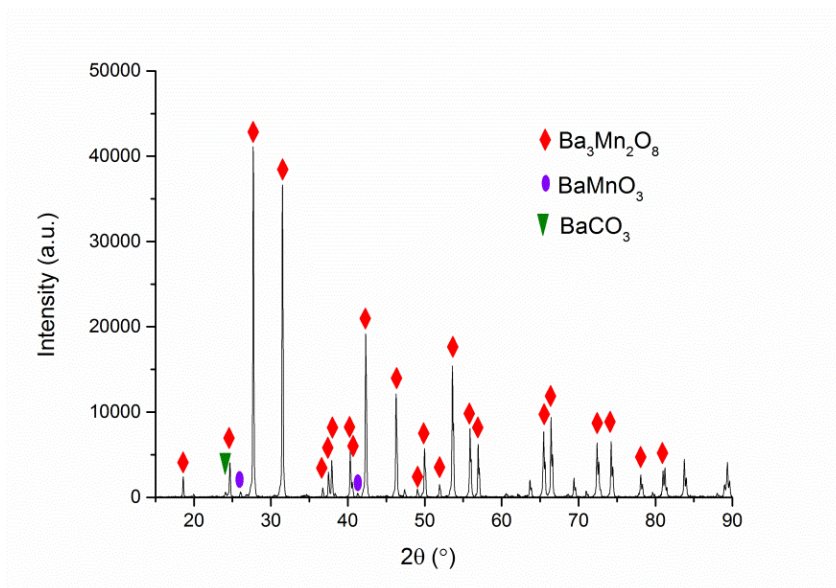


Figure A1.2a. XRD recorded on synthesized  $\text{Ba}_3\text{Mn}_2\text{O}_8$ .

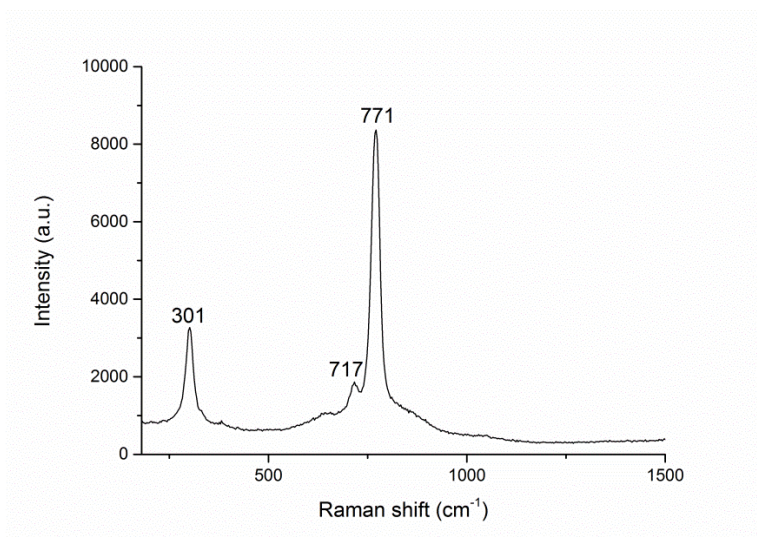


Figure A1.2b. Raman spectrum collected from the synthesized  $\text{Ba}_3\text{Mn}_2\text{O}_8$ .

The Raman spectrum of the synthesized  $\text{Ba}_3\text{Mn}_2\text{O}_8$  (Fig. A1.2b) has two dominant vibrational modes at  $301\text{ cm}^{-1}$  and  $771\text{ cm}^{-1}$ . The presence of these strong peaks, along with the results from the XRD data (Fig. A1.3), indicates that  $\text{Ba}_3\text{Mn}_2\text{O}_8$  formed on the BaO infiltrated LSM electrodes. Furthermore, the Raman spectrum of  $\text{Ba}_3\text{Mn}_3\text{O}_8$  is

similar to the Raman spectra of  $\text{Sr}_3\text{V}_2\text{O}_8$  and  $\text{Ba}_3\text{V}_2\text{O}_8$  reported in literature.<sup>[323]</sup> Based on these studies the  $301\text{ cm}^{-1}$  vibrational band can be ascribed to O-Mn-O bending while the  $717\text{ cm}^{-1}$  and  $771\text{ cm}^{-1}$  bands are assigned to Mn-O stretching.

### A1.3. LSM-CGO Composite Electrode

The XRD data from the BaO infiltrated LSM-CGO composite electrode (Fig. A1.3) shows that  $\text{Ba}_3\text{Mn}_2\text{O}_8$  was present in the electrode prior to *in operando* Raman spectroscopy experiments and formed during the infiltration process.

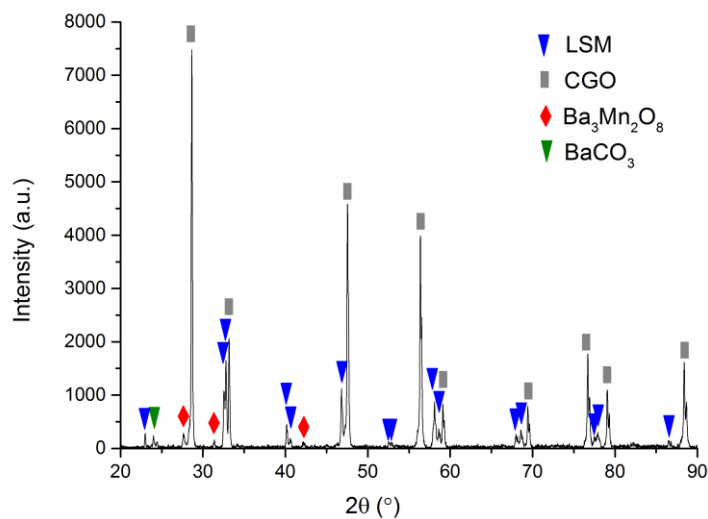


Figure A1.3. XRD recorded on porous LSM-CGO composite electrodes infiltrated with BaO prior to Raman spectroscopy experiments.

#### A1.4. Reproducibility between Porous Composite Electrodes and Model Thin Film Electrodes

LSM thin film electrodes served as model electrodes to investigate how the addition of BaO affects the electrocatalytic properties for O<sub>2</sub> reduction on LSM electrodes. To verify that the chemical species observed on these model electrodes were also present on porous electrodes used in typical applications, additional experiments were performed on LSM-CGO composite electrodes both with and without BaO. *In situ* Raman spectra collected on the plain and BaO infiltrated LSM-CGO porous composite electrodes are shown in Figure A1.4. A spectrum recorded on the BaO containing LSM thin film is included for comparison.

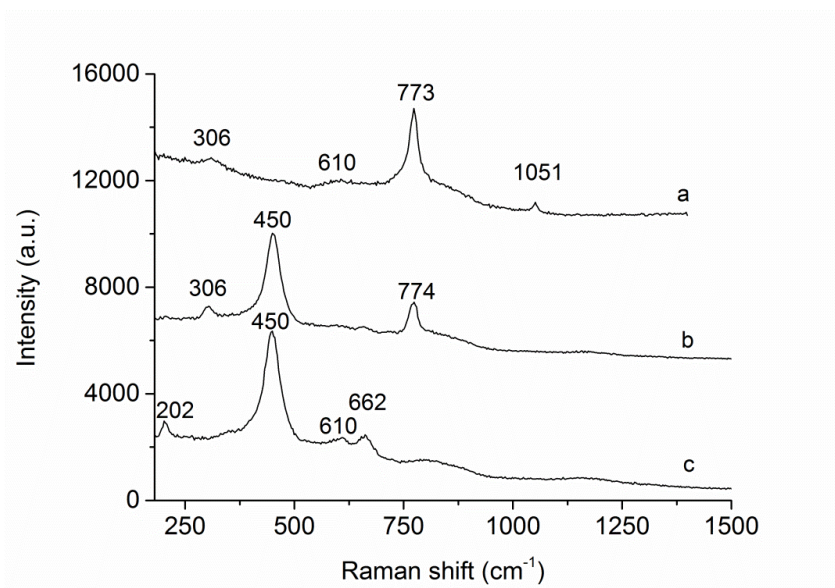


Figure A1.4 Representative Raman spectra recorded at 500 °C in 10% O<sub>2</sub> flow on (a) the LSM thin film electrode with BaO, (b) the porous LSM-CGO electrode infiltrated with BaO and (c) the porous LSM-CGO composite electrode without infiltration. The spectra are shifted on the Y-axis and re-scaled to facilitate comparisons.

The vibrational modes at approximately  $306\text{ cm}^{-1}$  and  $773\text{ cm}^{-1}$  are distinct for both BaO infiltrated samples and are assigned to  $\text{Ba}_3\text{Mn}_2\text{O}_8$  while the  $1051\text{ cm}^{-1}$  peak is assigned to either MnO or  $\text{BaCO}_3$ .<sup>[192,303]</sup> The strong peak at  $450\text{ cm}^{-1}$  corresponds to CGO and is shifted to lower frequencies relative to the commonly reported  $462\text{ cm}^{-1}$  due to the elevated operational temperature.<sup>[324]</sup> Minor peaks observed at  $610\text{ cm}^{-1}$  and  $662\text{ cm}^{-1}$  are assigned to  $\text{MnO}_2$  and  $\text{Mn}_2\text{O}_3$ , respectively.<sup>[290,302,304]</sup> A weak feature at  $202\text{ cm}^{-1}$  was observed on the porous composite LSM electrode and is attributed to the lattice vibrations in the LSM.<sup>[325]</sup>

#### A1.5. Representative Chronoamperometry Curve

An example of the chronoamperometry curves recorded on a cell with a BaO infiltrated thin film LSM electrode is shown in Figure A1.5. The current density approached an asymptotic limit of  $1.7\text{ mA/cm}^2$  after  $\sim 600$  seconds under an applied potential of  $-1\text{ V}$ .

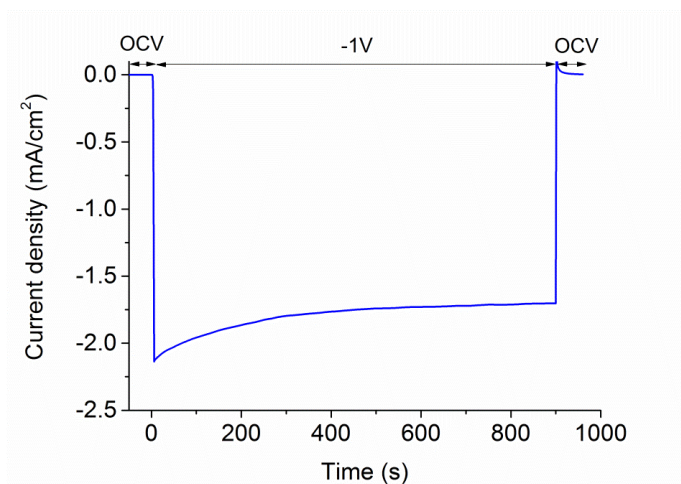


Figure A1.5 Representative chronoamperometry curve for BaO infiltrated LSM thin film electrode at  $500\text{ }^{\circ}\text{C}$  in  $10\%\text{ O}_2$  with Ar polarized at  $-1\text{ V}$ .

### A1.6. In Operando Raman Spectroscopy at 300 °C

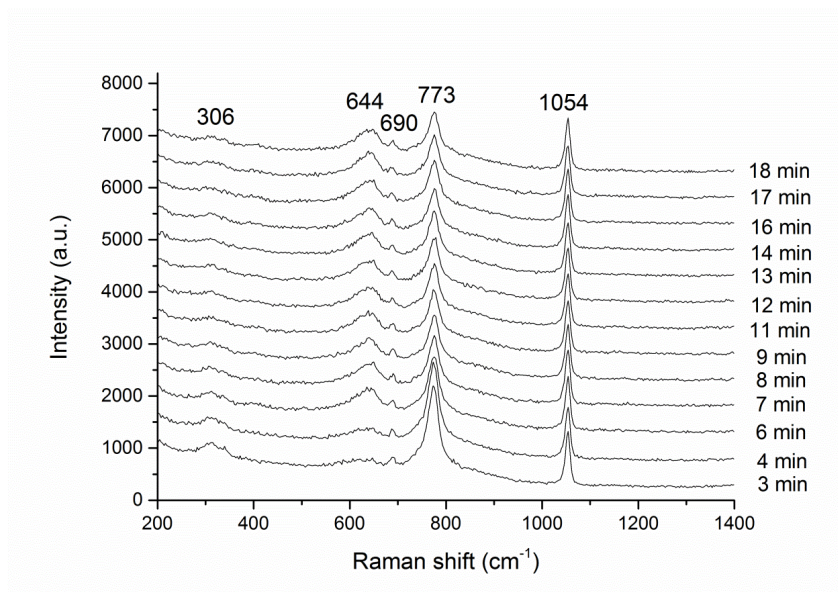


Figure A1.6a. Raman spectra recorded on LSM thin film electrode with BaO deposition at 300 °C in 10% O<sub>2</sub> before and during the onset of -1 V applied potential.

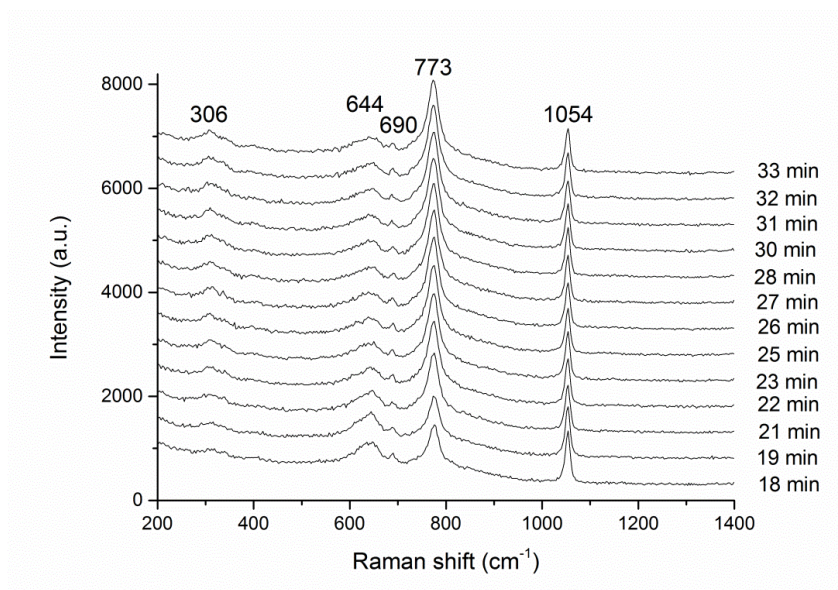


Figure A1.6b. Raman spectra recorded on LSM thin film electrode with BaO deposition at 300 °C in 10% O<sub>2</sub> before and during a +1 V potential was applied to the cell. The bottom spectrum was recorded with the cell polarized at -1 V prior to switching the applied potential to +1 V.



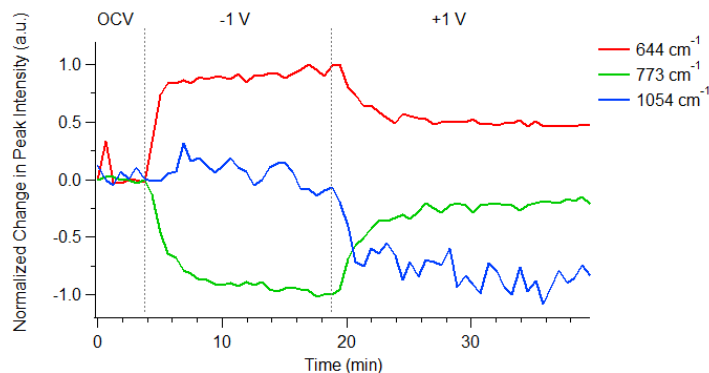


Figure A1.6c. Normalized change in peak intensity from Raman spectra collected on a BaO infiltrated LSM thin film electrode at 300 °C with 10% O<sub>2</sub> during -1V polarization followed immediately by +1V polarization.

Relative peak intensities within a given spectrum showed consistent and reproducible quantitative differences as a function of temperature (Fig. A1.6a–A1.6c). For example, the feature at 690 cm<sup>-1</sup> is more pronounced in Raman spectra recorded at 300°C compared to spectra recorded at 500 °C. These differences are likely due to reduced line broadening and the better signal-to-noise ratios at the lower temperature.

#### A1.7. In Operando Raman Spectroscopy at 500 °C

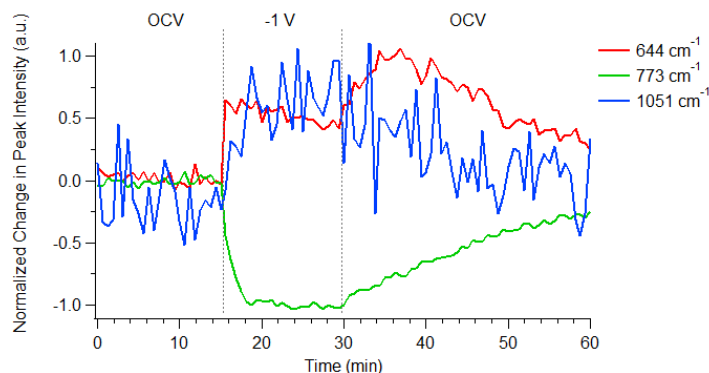


Figure A1.7. Normalized change in peak intensity from Raman spectra collected on a BaO infiltrated LSM thin film electrode at 500 °C with 10% O<sub>2</sub> prior to, during and after -1V polarization. During this experiment the 644 cm<sup>-1</sup> peak increased more rapidly than the 773 cm<sup>-1</sup> peak increased immediately after applying the -1 V polarizations.

## REFERENCES CITED

- [1] *International Energy Outlook 2016*. EIA Annual Energy Outlook; United States Energy Information Administration, May 2016.
- [2] Adams, T. A.; Nease, J.; Tucker, D.; Barton, P. I. Energy Conversion with Solid Oxide Fuel Cell Systems: A Review of Concepts and Outlooks for the Short- and Long-Term. *Ind. Eng. Chem. Res.* **2012**, 52, 3089-3111.
- [3] Weber, A.; Ivers-Tiffée, E. Materials and concepts for solid oxide fuel cells (SOFCs) in stationary and mobile applications. *J. Power Sources* **2004**, 127, 273-283.
- [4] Song, C. Fuel processing for low-temperature and high-temperature fuel cells: Challenges, and opportunities for sustainable development in the 21st century. *Catal. Today* **2002**, 77, 17-49.
- [5] Nehter, P.; Hansen, J. B.; Larsen, P. K. A techno-economic comparison of fuel processors utilizing diesel for solid oxide fuel cell auxiliary power units. *J. Power Sources* **2011**, 196, 7347-7354.
- [6] Laguna-Bercero, M. A. Recent advances in high temperature electrolysis using solid oxide fuel cells: A review. *J. Power Sources* **2012**, 203, 4-16.
- [7] Gomez, S. Y.; Hotza, D. Current developments in reversible solid oxide fuel cells. *Renewable & Sustainable Energy Reviews* **2016**, 61, 155-174.
- [8] Hauch, A.; Brodersen, K.; Chen, M.; Mogensen, M. B. Ni/YSZ electrodes structures optimized for increased electrolysis performance and durability. *Solid State Ionics* **2016**, 293, 27-36.
- [9] Wendel, C. H.; Braun, R. J. Design and techno-economic analysis of high efficiency reversible solid oxide cell systems for distributed energy storage. *Appl. Energy* **2016**, 172, 118-131.
- [10] *Energy and Air Pollution*. World Energy Outlook Special Report; International Energy Agency: Paris, France, June 2016.
- [11] *Energy and Climate Change*. World Energy Outlook Special Report; International Energy Agency: Paris, France, May 2015.
- [12] Hubbell, B. J.; Crume, R. V.; Evarts, D. M.; Cohen, J. M. Policy Monitor. *Rev. Environ. Econ. Policy* **2010**, 4, 122-138.

- [13] *Annual Energy Outlook 2016 with projections to 2040*. EIA Annual Energy Outlook; United States Energy Information Administration: Washington, DC, August 2016; pp DOE/EIA-0383.
- [14] Doyle, A.; Rampton, R. Paris climate accord to take effect; Obama hails 'historic day'. *Reuters News Media* [Online], Oct. 5, 2016, World News.  
<http://www.reuters.com/article/us-climatechange-paris-idUSKCN12523G> (accessed Oct. 5, 2016).
- [15] *Paris Agreement*; United Nations: Paris, France, 2015;  
[http://unfccc.int/files/essential\\_background/convention/application/pdf/english\\_paris\\_agreement.pdf](http://unfccc.int/files/essential_background/convention/application/pdf/english_paris_agreement.pdf).
- [16] U.S. Department of Energy. Glossary of Energy-Related Terms.  
<http://energy.gov/eere/energybasics/articles/glossary-energy-related-terms> (accessed Oct. 13, 2016).
- [17] Dziurdzia, B.; Magonski, Z.; Jankowski, H. Commercialisation of Solid Oxide Fuel Cells - opportunities and forecasts. In *39th International Microelectronics and Packaging Imaps Poland 2015 Conference*; IOP Conference Series-Materials Science and Engineering Vol. 104, 2016.
- [18] *Fuel Cell Technologies Market Report 2015*. Energy Efficiency and Renewable Energy; United States Department of Energy, August 2016.
- [19] Menzler, N. H.; Tietz, F.; Uhlenbruck, S.; Buchkremer, H. P.; Stöver, D. Materials and manufacturing technologies for solid oxide fuel cells. *J. Mater. Sci.* **2010**, *45*, 3109-3135.
- [20] Ormerod, R. M. Solid oxide fuel cells. *Chemical Society reviews* **2003**, *32*, 17-28.
- [21] Ryan, M. Fuel Cells for Greener Shipping. Dec. 5, 2012, Fuel Cell Today.  
<http://fuelcelltoday.com/analysis/analyst-views/2012/12-12-05-fuel-cells-for-greener-shipping> (accessed Oct. 4, 2016).
- [22] Lindahl, P.; Moog, E.; Shaw, S. R. Simulation, Design, and Validation of an UAV SOFC Propulsion System. *Aerospace and Electronic Systems, IEEE Transactions on* **2012**, *48*, 2582-2593.
- [23] Kan, W. H.; Thangadurai, V. Challenges and prospects of anodes for solid oxide fuel cells (SOFCs). *Ionics* **2015**, *21*, 301-318.
- [24] Ivers-Tiffée, E. Electrolytes | Solid: Oxygen Ions. In *Encyclopedia of Electrochemical Power Sources*; Elsevier: Amsterdam, 2009; pp 181-187.



- [25] Badwal, S. P. S. Zirconia-based solid electrolytes: microstructure, stability and ionic conductivity. *Solid State Ionics* **1992**, 52, 23-32.
- [26] Zhou, Y.;Yuan, W.;Huang, Q.;Huang, W.;Cheng, H.;Liu, H. Effect of Y<sub>2</sub>O<sub>3</sub> addition on the phase composition and crystal growth behavior of YSZ nanocrystals prepared via coprecipitation process. *Ceram. Int.* **2015**, 41, 10702-10709.
- [27] Yamamura, Y.;Kawasaki, S.;Sakai, H. Molecular dynamics analysis of ionic conduction mechanism in yttria-stabilized zirconia. *Solid State Ionics* **1999**, 126, 181-189.
- [28] Ramamoorthy, R.;Sundararaman, D.;Ramasamy, S. Ionic conductivity studies of ultrafine-grained yttria stabilized zirconia polymorphs. *Solid State Ionics* **1999**, 123, 271-278.
- [29] Singhal, S. C. Zirconia Electrolyte-based Solid Oxide Fuel Cells. In *Encyclopedia of Materials: Science and Technology*; Elsevier: Oxford, 2001; pp 9898-9902.
- [30] Zhang, L.;Zhu, L.;Virkar, A. V. Electronic conductivity measurement of yttria-stabilized zirconia solid electrolytes by a transient technique. *J. Power Sources* **2016**, 302, 98-106.
- [31] Jiang, S. P. Development of lanthanum strontium manganite perovskite cathode materials of solid oxide fuel cells: A review. *J. Mater. Sci.* **2008**, 43, 6799-6833.
- [32] Singhal, S. C. Solid Oxide Fuel Cells: Past, Present and Future. In *Solid Oxide Fuels Cells: Facts and Figures*; Springer-Verlag: London, 2013; pp 1-23.
- [33] Jiang, S. P. A comparison of O<sub>2</sub> reduction reactions on porous (La,Sr)MnO<sub>3</sub> and (La,Sr)(Co,Fe)O<sub>3</sub> electrodes. *Solid State Ionics* **2002**, 146, 1-22.
- [34] Kuengas, R.;Vohs, J. M.;Gorte, R. J. Effect of the Ionic Conductivity of the Electrolyte in Composite SOFC Cathodes. *J. Electrochem. Soc.* **2011**, 158, B743-B748.
- [35] Co, A. C.;Xia, S. J.;Birss, V. I. A kinetic study of the oxygen reduction reaction at LaSrMnO(3)-YSZ composite electrodes. *J. Electrochem. Soc.* **2005**, 152, A570-A576.
- [36] Traulsen, M. L.;Andersen, K. B.;Hansen, K. K. NO<sub>x</sub> conversion on LSM15-CGO10 cell stacks with BaO impregnation. *J. Mater. Chem.* **2012**, 22, 11792-11800.
- [37] Buccheri, M. A.;Singh, A.;Hill, J. M. Anode- versus electrolyte-supported Ni-YSZ/YSZ/Pt SOFCs: Effect of cell design on OCV, performance and carbon formation for the direct utilization of dry methane. *Journal of Power Sources* **2011**, 196, 968-976.

- [38] Pomfret, M. B.;Stoltz, C.;Varughese, B.;Walker, R. A. Structural and Compositional Characterization of Yttria-Stabilized Zirconia: Evidence of Surface-Stabilized, Low-Valence Metal Species. *Anal. Chem.* **2005**, *77*, 1791-1795.
- [39] Eigenbrodt, B. C.;Pomfret, M. B.;Steinhurst, D. A.;Owrutsky, J. C.;Walker, R. A. Direct, In Situ Optical Studies of Ni-YSZ Anodes in Solid Oxide Fuel Cells Operating with Methanol and Methane. *Journal of Physical Chemistry C* **2011**, *115*, 2895-2903.
- [40] Staniforth, J. Z.;Ormerod, R. M. Biogas as a fuel for solid oxide fuel cells and synthesis gas production: effects of ceria-doping and hydrogen sulfide on the performance of nickel-based anode materials. *Dalton Trans.* **2011**, *40*, 5494-5504.
- [41] McIntyre, M. D.;Neuburger, D. M.;Walker, R. A. In Situ Optical Studies of Carbon Accumulation with Different Molecular Weight Alkanes on Solid Oxide Fuel Cell Ni Anodes. *ECS Trans.* **2015**, *66*, 11-19.
- [42] Lee, W. Y.;Hanna, J.;Ghoniem, A. F. On the Predictions of Carbon Deposition on the Nickel Anode of a SOFC and Its Impact on Open-Circuit Conditions. *J. Electrochem. Soc.* **2013**, *160*, F94-F105.
- [43] Laycock, C. J.;Staniforth, J. Z.;Ormerod, R. M. Biogas as a fuel for solid oxide fuel cells and synthesis gas production: effects of ceria-doping and hydrogen sulfide on the performance of nickel-based anode materials. *Dalton Trans.* **2011**, *40*, 5494-5504.
- [44] McIntosh, S.;Gorte, R. J. Direct hydrocarbon solid oxide fuel cells. *Chem. Rev.* **2004**, *104*, 4845-4865.
- [45] Guerra, C.;Lanzini, A.;Leone, P.;Santarelli, M.;Brandon, N. P. Optimization of dry reforming of methane over Ni/YSZ anodes for solid oxide fuel cells. *J. Power Sources* **2014**, *245*, 154-163.
- [46] He, H.;Hill, J. M. Carbon deposition on Ni/YSZ composites exposed to humidified methane. *Appl. Catal. A* **2007**, *317*, 284-292.
- [47] Islam, S.;Hill, J. M. Barium oxide promoted Ni/YSZ solid-oxide fuel cells for direct utilization of methane. *J. Mater. Chem. A* **2014**, *2*, 1922-1929.
- [48] Singh, A.;Hill, J. M. Carbon tolerance, electrochemical performance and stability of solid oxide fuel cells with Ni/yttria stabilized zirconia anodes impregnated with Sn and operated with methane. *J. Power Sources* **2012**, *214*, 185-194.
- [49] Faes, A.;Hessler-Wyser, A.;Zryd, A.;Van herle, J. A Review of RedOx Cycling of Solid Oxide fuel Cells Anode. *Membranes* **2012**, *2*, 585-664.

- [50] Fouquet, D.;Mueller, A. C.;Weber, A.;Ivers-Tiffee, E. Kinetics of oxidation and reduction of Ni/YSZ cermets. *Ionics* **2003**, 8, 103-108.
- [51] Sukino, S.;Watanabe, S.;Sato, K.;Iguchi, F.;Yugami, H.;Kawada, T.;Mizusaki, J.;Hashida, T. Effect of Redox Cycling on Mechanical Properties of Ni-YSZ Cermets for SOFC Anodes. In *Solid Oxide Fuel Cells 12*; ECS Transactions Vol. 35, 2011; pp 1473-1482.
- [52] Cho, H. J.;Park, Y. M.;Choi, G. M. Enhanced power density of metal-supported solid oxide fuel cell with a two-step firing process. *Solid State Ionics* **2011**, 192, 519-522.
- [53] Cho, D.-G.;Yang, S.-K.;Yun, J.-C.;Kim, H.-S.;Lee, J.-S.;Lee, C. S. Effect of sintering profile on densification of nano-sized Ni/Al<sub>2</sub>O<sub>3</sub> composite. *Composites Part B: Engineering* **2013**, 45, 159-164.
- [54] Tanasini, P.;Cannarozzo, M.;Costamagna, P.;Faes, A.;Van Herle, J.;Hessler-Wyser, A.;Comninellis, C. Experimental and Theoretical Investigation of Degradation Mechanisms by Particle Coarsening in SOFC Electrodes. *Fuel Cells* **2009**, 9, 740-752.
- [55] Hansen, T. W.;Delariva, A. T.;Challa, S. R.;Datye, A. K. Sintering of Catalytic Nanoparticles: Particle Migration or Ostwald Ripening? *Accounts of Chemical Research* **2013**, 46, 1720-1730.
- [56] Takahashi, R.;Sato, S.;Sodesawa, T.;Yoshida, M.;Tomiyaama, S. Addition of zirconia in Ni/SiO<sub>2</sub> catalyst for improvement of steam resistance. *Appl. Catal. A* **2004**, 273, 211-215.
- [57] Granger, P.;Parvulescu, V. I. Catalytic NO<sub>x</sub> Abatement Systems for Mobile Sources: From Three-Way to Lean Burn after-Treatment Technologies. *Chem. Rev.* **2011**, 111, 3155-3207.
- [58] Heeb, N. V.;Zimmerli, Y.;Czerwinski, J.;Schmid, P.;Zennegg, M.;Haag, R.;Seiler, C.;Wichser, A.;Ulrich, A.;Honegger, P.;Zeyer, K.;Emmenegger, L.;Mosimann, T.;Kasper, M.;Mayer, A. Reactive nitrogen compounds (RNCs) in exhaust of advanced PM-NO<sub>x</sub> abatement technologies for future diesel applications. *Atmospheric Environment* **2011**, 45, 3203-3209.
- [59] Kishimoto, H.;Suzuki, A.;Shimonosono, T.;Brito, M. E.;Yamaji, K.;Horita, T.;Munakata, F.;Yokokawa, H. Agglomeration behavior of nickel particles on YSZ electrolyte. *Solid State Ionics* **2012**, 225, 65-68.
- [60] Driscoll, D. R.;McIntyre, M. D.;Welander, M. M.;Sofie, S. W.;Walker, R. A. Enhancement of high temperature metallic catalysts: Aluminum titanate in the nickel-zirconia system. *Appl. Catal. A* **2016**, 527, 36-44.

- [61] Lundegaard, L. F.;Tiruvalam, R. R.;Tyrsted, C.;Carlsson, A.;Morales-Cano, F.;Ovesen, C. V. Migrating Al species hindering NiO reduction on Al containing catalyst carriers. *Catal. Today* **2016**, 272, 25-31.
- [62] Ferraro, J. R.;Nakamoto, K.;Brown, C. W. Instrumentation and Experimental Techniques. In *Introductory Raman Spectroscopy (Second Edition)*; Academic Press: San Diego, 2003; pp 95-146.
- [63] McCreery, R. L. *Raman Spectroscopy for Chemical Analysis*; Chemical Analysis 157; Wiley-Interscience: New York, NY, 2000.
- [64] Merlin, R.;Pinczuk, A.;Weber, W. H. Overview of Phonon Raman Scattering in Solids. In *Raman Scattering in Materials Science*; Springer Series in Materials Science Vol. 42; Springer Berlin Heidelberg: New York, 2013; pp 1-26.
- [65] Kim, H.;Kosuda, K. M.;Van Duyne, R. P.;Stair, P. C. Resonance Raman and surface- and tip-enhanced Raman spectroscopy methods to study solid catalysts and heterogeneous catalytic reactions. *Chem. Soc. Rev.* **2010**, 39, 4820-4844.
- [66] Mironova-Ulmane, N.;Kuzmin, A.;Steins, I.;Grabis, J.;Sildos, I.;Paers, M. Raman scattering in nanosized nickel oxide NiO. *J. Phys.: Conf. Ser.* **2007**, 93, 012039.
- [67] Ferraro, J. R.;Nakamoto, K.;Brown, C. W. Materials Applications. In *Introductory Raman Spectroscopy (Second Edition)*; Academic Press: San Diego, 2003; pp 207-266.
- [68] Hofmann, P.;Panopoulos, K. D. Detailed dynamic Solid Oxide Fuel Cell modeling for electrochemical impedance spectra simulation. *Journal of Power Sources* **2010**, 195, 5320-5339.
- [69] Huang, Q.-A.;Hui, R.;Wang, B.;Zhang, H. A review of AC impedance modeling and validation in SOFC diagnosis. *Electrochim. Acta* **2007**, 52, 8144-8164.
- [70] Huggins, R. A. Simple method to determine electronic and ionic components of the conductivity in mixed conductors a review. *Ionics* **2002**, 8, 300-313.
- [71] Jensen, S. H.;Hauch, A.;Knibbe, R.;Jacobsen, T.;Mogensen, M. Modeling Degradation in SOEC Impedance Spectra. *J. Electrochem. Soc.* **2013**, 160, F244-F250.
- [72] Jacobson, A. J. Materials for Solid Oxide Fuel Cells. *Chem. Mater.* **2010**, 22, 660-674.

- [73] López-Fonseca, R.;Jiménez-González, C.;de Rivas, B.;Gutiérrez-Ortiz, J. I. Partial oxidation of methane to syngas on bulk NiAl<sub>2</sub>O<sub>4</sub> catalyst. Comparison with alumina supported nickel, platinum and rhodium catalysts. *Appl. Catal. A* **2012**, 437–438, 53-62.
- [74] Kee, R. J.;Zhu, H.;Sukeshini, A. M.;Jackson, G. S. Solid Oxide Fuel Cells: Operating Principles, Current Challenges, and the Role of Syngas. *Combust. Sci. Technol.* **2008**, 180, 1207-1244.
- [75] Penchini, D.;Cinti, G.;Discepoli, G.;Sisani, E.;Desideri, U. Characterization of a 100 W SOFC stack fed by carbon monoxide rich fuels. *Int. J. Hydrogen Energy* **2013**, 38, 525-531.
- [76] Finnerty, C. M.;Coe, N. J.;Cunningham, R. H.;Ormerod, R. M. Carbon formation on and deactivation of nickel-based/zirconia anodes in solid oxide fuel cells running on methane. *Catal. Today* **1998**, 46, 137-145.
- [77] Lorente, E.;Millan, M.;Brandon, N. P. Use of gasification syngas in SOFC: Impact of real tar on anode materials. *Int. J. Hydrogen Energy* **2012**, 37, 7271-7278.
- [78] Jalan, B. P.;Rao, Y. K. A study of the rates of catalyzed Boudouard reaction. *Carbon* **1978**, 16, 175-184.
- [79] Pomfret, M. B.;Owrutsky, J. C.;Walker, R. A. In Situ Studies of Fuel Oxidation in Solid Oxide Fuel Cells. *Anal. Chem.* **2007**, 79, 2367-2372.
- [80] He, H. P.;Hill, J. M. Carbon deposition on Ni/YSZ composites exposed to humidified methane. *Appl. Catal. A* **2007**, 317, 284-292.
- [81] Catapan, R. C.;Oliveira, A. A. M.;Chen, Y.;Vlachos, D. G. DFT Study of the Water–Gas Shift Reaction and Coke Formation on Ni(111) and Ni(211) Surfaces. *J. Phys. Chem. C* **2012**, 116, 20281-20291.
- [82] Nease, J.;Adams Ii, T. A. Systems for peaking power with 100% CO<sub>2</sub> capture by integration of solid oxide fuel cells with compressed air energy storage. *J. Power Sources* **2013**, 228, 281-293.
- [83] Wen, H.;Ordóñez, J. C.;Vargas, J. V. C. Composite electrode modelling and optimization for solid oxide fuel cells. *Int. J. Energy Res.* **2013**, 37, 95-104.
- [84] Wang, S.;Worek, W. M.;Minkowycz, W. J. Performance comparison of the mass transfer models with internal reforming for solid oxide fuel cell anodes. *Int. J. Heat Mass Transfer* **2012**, 55, 3933-3945.

- [85] Zhou, X. D.;Singhal, S. C. Fuel Cells | Solid Oxide Fuel Cells: Overview. In *Encyclopedia of Electrochemical Power Sources*; Elsevier: Amsterdam, 2009; pp 1-16.
- [86] Suwanwarangkul, R.;Croiset, E.;Entchev, E.;Charojrochkul, S.;Pritzker, M. D.;Fowler, M. W.;Douglas, P. L.;Chewathanakup, S.;Mahaudom, H. Experimental and modeling study of solid oxide fuel cell operating with syngas fuel. *J. Power Sources* **2006**, *161*, 308-322.
- [87] Demircan, O.;Zhang, W.;Xu, C.;Zondlo, J.;Finklea, H. O. The effect of overpotential on performance degradation of the solid oxide fuel cell Ni/YSZ anode during exposure to syngas with phosphine contaminant. *J. Power Sources* **2010**, *195*, 3091-3096.
- [88] Gorte, R. J.;Vohs, J. M.;McIntosh, S. Recent developments on anodes for direct fuel utilization in SOFC. *Solid State Ionics* **2004**, *175*, 1-6.
- [89] Pomfret, M. B.;Marda, J.;Jackson, G. S.;Eichhorn, B. W.;Dean, A. M.;Walker, R. A. Hydrocarbon Fuels in Solid Oxide Fuel Cells: In Situ Raman Studies of Graphite Formation and Oxidation. *J. Phys. Chem. C* **2008**, *112*, 5232-5240.
- [90] Kirtley, J. D.;Halat, D. M.;McIntyre, M. D.;Eigenbrodt, B. C.;Walker, R. A. High-Temperature "Spectrochronopotentiometry": Correlating Electrochemical Performance with In Situ Raman Spectroscopy in Solid Oxide Fuel Cells. *Anal. Chem.* **2012**, *84*, 9745-9753.
- [91] Tuinstra, F.;Koenig, J. L. Raman Spectrum of Graphite. *J. Chem. Phys.* **1970**, *53*, 1126-1130.
- [92] Ferrari, A. C. Raman spectroscopy of graphene and graphite: Disorder, electron–phonon coupling, doping and nonadiabatic effects. *Solid State Commun.* **2007**, *143*, 47-57.
- [93] Ferrari, A. C.;Meyer, J. C.;Scardaci, V.;Casiraghi, C.;Lazzeri, M.;Mauri, F.;Piscanec, S.;Jiang, D.;Novoselov, K. S.;Roth, S.;Geim, A. K. Raman Spectrum of Graphene and Graphene Layers. *Phys. Rev. Lett.* **2006**, *97*, 187401.
- [94] Kirtley, J. D.;McIntyre, M. D.;Halat, D. M.;Walker, R. A. Insights into SOFC Ni/YSZ anode degradation using in situ Spectrochronopotentiometry. *ECS Trans.* **2013**, *50*, 3-15.
- [95] Liu, M.;Lynch, M. E.;Blinn, K.;Alamgir, F. M.;Choi, Y. Rational SOFC material design: new advances and tools. *Mater. Today* **2011**, *14*, 534-546.

- [96] Singhal, S. C. Advances in solid oxide fuel cell technology. *Solid State Ionics* **2000**, *135*, 305-313.
- [97] Malavasi, L.;Fisher, C. A. J.;Islam, M. S. Oxide-ion and proton conducting electrolyte materials for clean energy applications: structural and mechanistic features. *Chem. Soc. Rev.* **2010**, *39*, 4370-4387.
- [98] Lo Faro, M.;Antonucci, V.;Antonucci, P. L.;Aricò, A. S. Fuel flexibility: A key challenge for SOFC technology. *Fuel* **2012**, *102*, 554-559.
- [99] Badwal, S. P. S.;Giddey, S.;Kulkarni, A.;Goel, J.;Basu, S. Direct ethanol fuel cells for transport and stationary applications – A comprehensive review. *Appl. Energy* **2015**, *145*, 80-103.
- [100] Homel, M.;Gur, T. M.;Koh, J. H.;Virkar, A. V. Carbon monoxide-fueled solid oxide fuel cell. *J. Power Sources* **2010**, *195*, 6367-6372.
- [101] Cayan, F. N.;Zhi, M.;Pakalapati, S. R.;Celik, I.;Wu, N.;Gemmen, R. Effects of coal syngas impurities on anodes of solid oxide fuel cells. *J. Power Sources* **2008**, *185*, 595-602.
- [102] Trendewicz, A. A.;Braun, R. J. Techno-economic analysis of solid oxide fuel cell-based combined heat and power systems for biogas utilization at wastewater treatment facilities. *J. Power Sources* **2013**, *233*, 380-393.
- [103] Baniasadi, E.;Alemrajabi, A. A. Fuel cell energy generation and recovery cycle analysis for residential application. *Int. J. Hydrogen Energy* **2010**, *35*, 9460-9467.
- [104] Karellas, S.;Karl, J.;Kakaras, E. An innovative biomass gasification process and its coupling with microturbine and fuel cell systems. *Energy* **2008**, *33*, 284-291.
- [105] Peters, R.;Deja, R.;Blum, L.;Pennanen, J.;Kiviaho, J.;Hakala, T. Analysis of solid oxide fuel cell system concepts with anode recycling. *Int. J. Hydrogen Energy* **2013**, *38*, 6809-6820.
- [106] Powell, M.;Meinhardt, K.;Sprenkle, V.;Chick, L.;McVay, G. Demonstration of a highly efficient solid oxide fuel cell power system using adiabatic steam reforming and anode gas recirculation. *J. Power Sources* **2012**, *205*, 377-384.
- [107] Lo Faro, M.;Vita, A.;Pino, L.;Aricò, A. S. Performance evaluation of a solid oxide fuel cell coupled to an external biogas tri-reforming process. *Fuel Process. Technol.* **2013**, *115*, 238-245.

- [108] Drewery, M.;Kennedy, E.;Alenazey, F.;Dlugogorski, B.;Stockenhuber, M. The effect of synthesis gas composition on the performance of Ni-based solid oxide fuel cells. *Chem. Eng. Res. Des.* **2015**, *101*, 22-26.
- [109] Martinez, A.;Gerdes, K.;Gemmen, R.;Poston, J. Thermodynamic analysis of interactions between Ni-based solid oxide fuel cells (SOFC) anodes and trace species in a survey of coal syngas. *J. Power Sources* **2010**, *195*, 5206-5212.
- [110] Haga, K.;Adachi, S.;Shiratori, Y.;Itoh, K.;Sasaki, K. Poisoning of SOFC anodes by various fuel impurities. *Solid State Ionics* **2008**, *179*, 1427-1431.
- [111] Kee, R. J.;Zhu, H. Y.;Sukeshini, A. M.;Jackson, G. S. Solid Oxide Fuel Cells: Operating Principles, Current Challenges, and the Role of Syngas. *Combust. Sci. Technol.* **2008**, *180*, 1207-1244.
- [112] Jiang, Y.;Virkar, A. V. Fuel Composition and Diluent Effect on Gas Transport and Performance of Anode-Supported SOFCs. *J. Electrochem. Soc.* **2003**, *150*, A942-A951.
- [113] Alzate-Restrepo, V.;Hill, J. M. Carbon deposition on Ni/YSZ anodes exposed to CO/H<sub>2</sub> feeds. *J. Power Sources* **2010**, *195*, 1344-1351.
- [114] Chun, C. M.;Mumford, J. D.;Ramanarayanan, T. A. Carbon-Induced Corrosion of Nickel Anode. *J. Electrochem. Soc.* **2000**, *147*, 3680-3686.
- [115] Chen, T.;Wang, W. G.;Miao, H.;Li, T. S.;Xu, C. Evaluation of carbon deposition behavior on the nickel/yttrium-stabilized zirconia anode-supported fuel cell fueled with simulated syngas. *J. Power Sources* **2011**, *196*, 2461-2468.
- [116] Sasaki, K.;Teraoka, Y. Equilibria in Fuel Cell Gases - II. The C-H-O Ternary Diagrams. *J. Electrochem. Soc.* **2003**, *150*, A885-A888.
- [117] Wagman, D. D.;Kilpatrick, J. E.;Taylor, W. J.;Pitzer, K. S.;Rossini, F. D. Heats, Free Energies, and Equilibrium Constants of Some Reactions Involving O<sub>2</sub>, H<sub>2</sub>, H<sub>2</sub>O, C, CO, CO<sub>2</sub>, and CH<sub>4</sub>. *J. Res. Natl. Bur. Stand.* **1945**, *34*, 143-161.
- [118] Fan, P.;Zhang, X.;Hua, D.;Li, G. Experimental Study of the Carbon Deposition from CH<sub>4</sub> onto the Ni/YSZ Anode of SOFCs. *Fuel Cells* **2016**, *16*, 235-243.
- [119] Hunt, J.;Ferrari, A.;Lita, A.;Crosswhite, M.;Ashley, B.;Stiegman, A. E. Microwave-Specific Enhancement of the Carbon-Carbon Dioxide (Boudouard) Reaction. *J. Phys. Chem. C* **2013**, *117*, 26871-26880.



- [120] Yurkiv, V. Reformate-operated SOFC anode performance and degradation considering solid carbon formation: A modeling and simulation study. *Electrochim. Acta* **2014**, *143*, 114-128.
- [121] Pomfret, M. B.; Walker, R. A.; Owrutsky, J. C. High-Temperature Chemistry in Solid Oxide Fuel Cells: In Situ Optical Studies. *J. Phys. Chem. Lett.* **2012**, *3*, 3053-3064.
- [122] Kirtley, J. D.; Pomfret, M. B.; Steinhurst, D. A.; Owrutsky, J. C.; Walker, R. A. Toward a Working Mechanism of Fuel Oxidation in SOFCs: In Situ Optical Studies of Simulated Biogas and Methane. *J. Phys. Chem. C* **2015**, *119*, 12781-12791.
- [123] Pomfret, M. B.; Steinhurst, D. A.; Owrutsky, J. C. Identification of a Methane Oxidation Intermediate on Solid Oxide Fuel Cell Anode Surfaces with Fourier Transform Infrared Emission. *J. Phys. Chem. Lett.* **2013**, *4*, 1310-1314.
- [124] Li, X.; Liu, M.; Lee, J.-p.; Ding, D.; Bottomley, L. A.; Park, S.; Liu, M. An operando surface enhanced Raman spectroscopy (SERS) study of carbon deposition on SOFC anodes. *Phys. Chem. Chem. Phys.* **2015**, *17*, 21112-21119.
- [125] Maher, R. C.; Duboviks, V.; Offer, G. J.; Kishimoto, M.; Brandon, N. P.; Cohen, L. F. Raman Spectroscopy of Solid Oxide Fuel Cells: Technique Overview and Application to Carbon Deposition Analysis. *Fuel Cells* **2013**, *13*, 455-469.
- [126] Pomfret, M. B.; Owrutsky, J. C.; Walker, R. A. In Situ Optical Studies of Solid-Oxide Fuel Cells. *Annu. Rev. Anal. Chem.* **2010**, *3*, 151-174.
- [127] McIntyre, M. D.; Kirtley, J. D.; Halat, D. M.; Reeping, K. W.; Walker, R. A. In situ Spectroscopic Studies of Carbon Formation in SOFCs Operating with Syn-gas. *ECS Trans.* **2013**, *57*, 1267-1275.
- [128] Kirtley, J. D.; Steinhurst, D. A.; Owrutsky, J. C.; Pomfret, M. B.; Walker, R. A. In situ optical studies of methane and simulated biogas oxidation on high temperature solid oxide fuel cell anodes. *Phys. Chem. Chem. Phys.* **2014**, *16*, 227-236.
- [129] McIntyre, M. D.; Kirtley, J. D.; Singh, A.; Islam, S.; Hill, J. M.; Walker, R. A. Comparing in Situ Carbon Tolerances of Sn-Infiltrated and BaO-Infiltrated Ni-YSZ Cermet Anodes in Solid Oxide Fuel Cells Exposed to Methane. *J. Phys. Chem. C* **2015**, *119*, 7637-7647.
- [130] Calizo, I.; Bejenari, I.; Rahman, M.; Liu, G.; Balandin, A. A. Ultraviolet Raman microscopy of single and multilayer graphene. *J. Appl. Phys.* **2009**, *106*, 043509.
- [131] Kromp, A.; Leonide, A.; Weber, A.; Ivers-Tiffée, E. Electrochemical Analysis of Reformate-Fuelled Anode Supported SOFC. *J. Electrochem. Soc.* **2011**, *158*, B980-B986.

- [132] Holtappels, P.;De Haart, L. G. J.;Stimming, U.;Vinke, I. C.;Mogensen, M. Reaction of CO/CO<sub>2</sub> gas mixtures on Ni-YSZ cermet electrodes. *J. Appl. Electrochem.* **1999**, *29*, 561-568.
- [133] Matsuzaki, Y.;Yasuda, I. Electrochemical Oxidation of H<sub>2</sub> and CO in a H<sub>2</sub> - H<sub>2</sub>O - CO - CO<sub>2</sub> System at the Interface of a Ni-YSZ Cermet Electrode and YSZ Electrolyte. *J. Electrochem. Soc.* **2000**, *147*, 1630-1635.
- [134] McIntyre, M. D.;Kirtley, J. D.;Singh, A.;Islam, S.;Hill, J. M.;Walker, R. A. Comparing in Situ Carbon Tolerances of Sn-Infiltrated and BaO-Infiltrated Ni-YSZ Cermet Anodes in Solid Oxide Fuel Cells Exposed to Methane. *Journal of Physical Chemistry C* **2015**, *119*, 7637-7647.
- [135] Kirtley, J.;Singh, A.;Halat, D.;Oswell, T.;Hill, J. M.;Walker, R. A. In Situ Raman Studies of Carbon Removal from High Temperature Ni-YSZ Cermet Anodes by Gas Phase Reforming Agents. *J. Phys. Chem. C* **2013**, *117*, 25908-25916.
- [136] McIntosh, S.;Vohs, J. M.;Gorte, R. J. Role of Hydrocarbon Deposits in the Enhanced Performance of Direct-Oxidation SOFCs. *J. Electrochem. Soc.* **2003**, *150*, A470-A476.
- [137] Deleebeeck, L.;Hansen, K. K. Hybrid direct carbon fuel cells and their reaction mechanisms-a review. *J. Solid State Electrochem.* **2014**, *18*, 861-882.
- [138] Bai, X.;Wang, S.;Sun, T.;Wang, S. Influence of Operating Conditions on Carbon Deposition Over a Ni Catalyst for the Production of Synthetic Natural Gas (SNG) from Coal. *Catal. Lett.* **2014**, *144*, 2157-2166.
- [139] Froment, G. F. Kinetic modeling of hydrocarbon processing and the effect of catalyst deactivation by coke formation. *Catalysis Reviews-Science and Engineering* **2008**, *50*, 1-18.
- [140] Walters, K. M.;Dean, A. M.;Zhu, H. Y.;Kee, R. J. Homogeneous kinetics and equilibrium predictions of coking propensity in the anode channels of direct oxidation solid-oxide fuel cells using dry natural gas. *J. Power Sources* **2003**, *123*, 182-189.
- [141] Speck, P.;Young, D. J. Influence of Hafnium Additions and Preoxidation Treatment on the Metal Dusting of Ni-Al Alloys. *Oxid. Met.* **2011**, *76*, 287-305.
- [142] Nolan, P. E.;Lynch, D. C.;Cutler, A. H. Catalytic disproportionation of CO in the absence of hydrogen: Encapsulating shell carbon formation. *Carbon* **1994**, *32*, 477-483.

- [143] Young, D. J.;Zhang, J.;Geers, C.;Schutze, M. Recent advances in understanding metal dusting: A review. *Mater. Corros.* **2011**, 62, 7-28.
- [144] Caillot, T.;Gauthier, G.;Delichere, P.;Cayron, C.;Aires, F. J. C. S. Evidence of anti-coking behavior of  $\text{La}_{0.8}\text{Sr}_{0.2}\text{Cr}_{0.98}\text{Ru}_{0.02}\text{O}_3$  as potential anode material for Solid Oxide Fuel Cells directly fed under methane. *J. Catal.* **2012**, 290, 158-164.
- [145] Therdthianwong, S.;Siangchin, C.;Therdthianwong, A. Improvement of coke resistance of  $\text{Ni}/\text{Al}_2\text{O}_3$  catalyst in  $\text{CH}_4/\text{CO}_2$  reforming by  $\text{ZrO}_2$  addition. *Fuel Process. Technol.* **2008**, 89, 160-168.
- [146] Yoon, D.;Manthiram, A. Hydrogen tungsten bronze as a decoking agent for long-life, natural gas-fueled solid oxide fuel cells. *Energy Environ. Sci.* **2014**, 7, 3069-3076.
- [147] Vu, B. K.;Song, M. B.;Ahn, I. Y.;Suh, Y. W.;Suh, D. J.;Kim, J. S.;Shin, E. W. Location and structure of coke generated over  $\text{Pt-Sn}/\text{Al}_2\text{O}_3$  in propane dehydrogenation. *J. Ind. Eng. Chem.* **2011**, 17, 71-76.
- [148] Macleod, N.;Fryer, J. R.;Stirling, D.;Webb, G. Deactivation of bi- and multimetallic reforming catalysts: influence of alloy formation on catalyst activity. *Catal. Today* **1998**, 46, 37-54.
- [149] Garcia, L.;French, R.;Czernik, S.;Chornet, E. Catalytic steam reforming of bio-oils for the production of hydrogen: effects of catalyst composition. *Appl Catal a-Gen* **2000**, 201, 225-239.
- [150] Hou, Z.;Yokota, O.;Tanaka, T.;Yashima, T. Surface properties of a coke-free Sn doped nickel catalyst for the  $\text{CO}_2$  reforming of methane. *Appl. Surf. Sci.* **2004**, 233, 58-68.
- [151] Siddiqi, G.;Sun, P.;Galvita, V.;Bell, A. T. Catalyst performance of novel  $\text{Pt/Mg(Ga)(Al)O}$  catalysts for alkane dehydrogenation. *J. Catal.* **2010**, 274, 200-206.
- [152] de Lima, S. M.;da Silva, A. M.;Jacobs, G.;Davis, B. H.;Mattos, L. V.;Noronha, F. B. New approaches to improving catalyst stability over  $\text{Pt/ceria}$  during ethanol steam reforming: Sn addition and  $\text{CO}_2$  co-feeding. *Applied Catalysis B-Environmental* **2010**, 96, 387-398.
- [153] Wang, F.;Wang, W.;Ran, R.;Tade, M. O.;Shao, Z. Aluminum oxide as a dual-functional modifier of Ni-based anodes of solid oxide fuel cells for operation on simulated biogas. *J. Power Sources* **2014**, 268, 787-793.

- [154] Hanna, J.;Lee, W. Y.;Shi, Y.;Ghoniem, A. F. Fundamentals of electro- and thermochemistry in the anode of solid-oxide fuel cells with hydrocarbon and syngas fuels. *Prog. Energy Combust. Sci.* **2014**, *40*, 74-111.
- [155] Lu, Y. X.;Schaefer, L. A solid oxide fuel cell system fed with hydrogen sulfide and natural gas. *J. Power Sources* **2004**, *135*, 184-191.
- [156] Takagi, Y.;Kerman, K.;Ko, C.;Ramanathan, S. Operational characteristics of thin film solid oxide fuel cells with ruthenium anode in natural gas. *J. Power Sources* **2013**, *243*, 1-9.
- [157] Wongchanapai, S.;Iwai, H.;Saito, M.;Yoshida, H. Performance evaluation of a direct-biogas solid oxide fuel cell-micro gas turbine (SOFC-MGT) hybrid combined heat and power (CHP) system. *J. Power Sources* **2013**, *223*, 9-17.
- [158] Wang, W.;Wang, F.;Ran, R.;Park, H. J.;Jung, D. W.;Kwak, C.;Shao, Z. Coking suppression in solid oxide fuel cells operating on ethanol by applying pyridine as fuel additive. *J. Power Sources* **2014**, *265*, 20-29.
- [159] Sasaki, K.;Watanabe, K.;Teraoka, Y. Direct-Alcohol SOFCs: Current-Voltage Characteristics and Fuel Gas Compositions. *J. Electrochem. Soc.* **2004**, *151*, A965-A970.
- [160] Trimm, D. L. Coke formation and minimisation during steam reforming reactions. *Catal. Today* **1997**, *37*, 233-238.
- [161] Rakass, S.;Oudghiri-Hassani, H.;Rowntree, P.;Abatzoglou, N. Steam reforming of methane over unsupported nickel catalysts. *J. Power Sources* **2006**, *158*, 485-496.
- [162] Klein, J.-M.;Henault, M.;Roux, C.;Bultel, Y.;Georges, S. Direct methane solid oxide fuel cell working by gradual internal steam reforming: Analysis of operation. *J. Power Sources* **2009**, *193*, 331-337.
- [163] Toebe, M. L.;Bitter, J. H.;van Dillen, A. J.;de Jong, K. P. Impact of the structure and reactivity of nickel particles on the catalytic growth of carbon nanofibers. *Catal. Today* **2002**, *76*, 33-42.
- [164] Li, X.;Shao, G.;Luo, J.;Lu, J.;Xue, M.;Hou, Y.;Deng, L. Fabrication and characterization of GDC electrolyte/electrode integral SOFC with BaO/Ni-GDC anode. *Mater. Res. Bull.* **2014**, *50*, 337-340.
- [165] Yang, L.;Choi, Y.;Qin, W. T.;Chen, H. Y.;Blinn, K.;Liu, M. F.;Liu, P.;Bai, J. M.;Tyson, T. A.;Liu, M. L. Promotion of water-mediated carbon removal by nanostructured barium oxide/nickel interfaces in solid oxide fuel cells. *Nat Commun* **2011**, *2*.

- [166] Wang, W.;Zhu, H.;Yang, G.;Park, H. J.;Jung, D. W.;Kwak, C.;Shao, Z. A NiFeCu alloy anode catalyst for direct-methane solid oxide fuel cells. *J. Power Sources* **2014**, 258, 134-141.
- [167] Toscani, L. M.;Genoveva Zimicz, M.;Casanova, J. R.;Larrond, S. A. Ni-Cu/Ce<sub>0.9</sub>Zr<sub>0.1</sub>O<sub>2</sub> bimetallic cermets for electrochemical and catalytic applications. *Int. J. Hydrogen Energy* **2014**, 39, 8759-8766.
- [168] Yoon, D.;Manthiram, A. Hydrocarbon-fueled solid oxide fuel cells with surface-modified, hydroxylated Sn/Ni-Ce<sub>0.8</sub>Gd<sub>0.2</sub>O<sub>1.9</sub> heterogeneous catalyst anode. *J. Mater. Chem. A* **2014**, 2, 17041-17046.
- [169] Kan, H.;Lee, H. Sn-doped Ni/YSZ anode catalysts with enhanced carbon deposition resistance for an intermediate temperature SOFC. *Appl. Catal. B* **2010**, 97, 108-114.
- [170] Trimm, D. L. Catalysts for the control of coking during steam reforming. *Catal. Today* **1999**, 49, 3-10.
- [171] Zuo, P.;Fu, Z.;Yang, Z. First-principles study on the mechanism of coking inhibition by the Ni(111) surface doped with IB-group metals at the anode of solid oxide fuel cells. *J. Power Sources* **2013**, 242, 762-767.
- [172] Martins, R. L.;Baldanza, M. A. S.;Alberton, A. L.;Vasconcelos, S. M. R.;Moya, S. F.;Schmal, M. Effect of B and Sn on Ni catalysts supported on pure- and on WO<sub>3</sub>/MoO<sub>3</sub>-modified zirconias for direct CH<sub>4</sub> conversion to H<sub>2</sub>. *Appl. Catal. B* **2011**, 103, 326-335.
- [173] Xiao, J.;Xie, Y.;Liu, J.;Liu, M. Deactivation of nickel-based anode in solid oxide fuel cells operated on carbon-containing fuels. *J. Power Sources* **2014**, 268, 508-516.
- [174] Millichamp, J.;Mason, T. J.;Brandon, N. P.;Brown, R. J. C.;Maher, R. C.;Manos, G.;Neville, T. P.;Brett, D. J. L. A study of carbon deposition on solid oxide fuel cell anodes using electrochemical impedance spectroscopy in combination with a high temperature crystal microbalance. *J. Power Sources* **2013**, 235, 14-19.
- [175] Takahashi, H.;Takeguchi, T.;Yamamoto, N.;Matsuda, M.;Kobayashi, E.;Ueda, W. Effect of interaction between Ni and YSZ on coke deposition during steam reforming of methane on Ni/YSZ anode catalysts for an IR-SOFC. *J. Mol. Catal. A: Chem.* **2011**, 350, 69-74.
- [176] He, H. P.;Hill, J. M. Carbon deposition on Ni/YSZ composites exposed to humidified methane. *Appl Catal a-Gen* **2007**, 317, 284-292.

- [177] Baker, R. T.; Metcalfe, I. S. Study of the Activity and Deactivation of Ni-YSZ Cermet in Dry CH<sub>4</sub> Using Temperature-Programmed Techniques. *Ind. Eng. Chem. Res.* **1995**, *34*, 1558-1565.
- [178] Singh, A.; Islam, S.; Bucchieri, M. A.; Hill, J. M. Influence of Experimental Conditions on Reliability of Carbon Tolerance Studies on Ni/YSZ SOFC Anodes Operated with Methane. *Fuel Cells* **2013**, *13*, 703-711.
- [179] Li, X.; Blinn, K.; Fang, Y.; Liu, M.; Mahmoud, M. A.; Cheng, S.; Bottomley, L. A.; El-Sayed, M.; Liu, M. Application of surface enhanced Raman spectroscopy to the study of SOFC electrode surfaces. *Phys. Chem. Chem. Phys.* **2012**, *14*, 5919-5923.
- [180] Pomfret, M. B.; Owrutsky, J. C.; Walker, R. A. In Situ Optical Studies of Solid-Oxide Fuel Cells. In *Annual Review of Analytical Chemistry, Vol 3*; Annual Review of Analytical Chemistry Vol. 3, 2010; pp 151-174.
- [181] Pomfret, M. B.; Owrutsky, J. C.; Walker, R. A. High-Temperature Raman Spectroscopy of Solid Oxide Fuel Cell Materials and Processes. *J. Phys. Chem. B* **2006**, *110*, 17305-17308.
- [182] Primdahl, S.; Mogensen, M. Oxidation of Hydrogen on Ni/Yttria-Stabilized Zirconia Cermet Anodes. *J. Electrochem. Soc.* **1997**, *144*, 3409-3419.
- [183] Kee, R. J.; Zhu, H. Y.; Goodwin, D. G. Solid-oxide fuel cells with hydrocarbon fuels. *Proceedings of the Combustion Institute* **2005**, *30*, 2379-2404.
- [184] Buciuman, F.-C.; Patcas, F.; Menezes, J.-C.; Barbier, J.; Hahn, T.; Lintz, H.-G. Catalytic properties of La<sub>0.8</sub>A<sub>0.2</sub>MnO<sub>3</sub> (A = Sr, Ba, K, Cs) and LaMn<sub>0.8</sub>B<sub>0.2</sub>O<sub>3</sub> (B = Ni, Zn, Cu) perovskites: 1. Oxidation of hydrogen and propene. *Applied Catalysis B: Environmental* **2002**, *35*, 175-183.
- [185] Nikolla, E.; Schwank, J.; Linic, S. Comparative study of the kinetics of methane steam reforming on supported Ni and Sn/Ni alloy catalysts: The impact of the formation of Ni alloy on chemistry. *J. Catal.* **2009**, *263*, 220-227.
- [186] Serra, J. M.; Meulenberg, W. A. Thin-film Proton BaZr<sub>0.85</sub>Y<sub>0.15</sub>O<sub>3</sub> Conducting Electrolytes: Toward an Intermediate-Temperature Solid Oxide Fuel Cell Alternative. *Journal of the American Ceramic Society* **2007**, *90*, 2082-2089.
- [187] Nabae, Y.; Pointon, K. D.; Irvine, J. T. S. Ni/C Slurries Based on Molten Carbonates as a Fuel for Hybrid Direct Carbon Fuel Cells. *J. Electrochem. Soc.* **2009**, *156*, B716-B720.

- [188] Hecht, E. S.;Gupta, G. K.;Zhu, H. Y.;Dean, A. M.;Kee, R. J.;Maier, L.;Deutschmann, O. Methane reforming kinetics within a Ni-YSZ SOFC anode support. *Appl Catal a-Gen* **2005**, 295, 40-51.
- [189] Vovk, E. I.;Emmez, E.;Erbudak, M.;Bukhtiyarov, V. I.;Ozensoy, E. Role of the Exposed Pt Active Sites and BaO<sub>2</sub> Formation in NO<sub>x</sub> Storage Reduction Systems: A Model Catalyst Study on BaO<sub>x</sub>/Pt(111). *J. Phys. Chem. C* **2011**, 115, 24256-24266.
- [190] Shishkin, M.;Ziegler, T. Oxidation of H-2, CH<sub>4</sub>, and CO Molecules at the Interface between Nickel and Ytria-Stabilized Zirconia: A Theoretical Study Based on DFT. *J Phys Chem C* **2009**, 113, 21667-21678.
- [191] Su, S. C.;Bell, A. T. Raman studies of peroxide formation, decomposition, and reduction on Ba/MgO. *Catal. Lett.* **1996**, 36, 15-19.
- [192] Kaabar, W.;Bott, S.;Devonshire, R. Raman spectroscopic study of mixed carbonate materials. *Spectrochim. Acta A* **2011**, 78, 136-141.
- [193] Faes, A.;Fuerbringer, J.-M.;Mohamedi, D.;Hessler-Wyser, A.;Caboche, G.;Van Herle, J. Design of experiment approach applied to reducing and oxidizing tolerance of anode supported solid oxide fuel cell. Part I: Microstructure optimization. *J. Power Sources* **2011**, 196, 7058-7069.
- [194] LaBarbera, M.;Fedkin, M.;Lvov, S. Liquid Tin-Lead Anode Solid Oxide Fuel Cell Fueled by Coal. *Elec. Soc. Trans.* **2011**, 35, 2725-2734.
- [195] Leveque, G.;Abanades, S. Thermodynamic and Kinetic Study of the Carbothermal Reduction of SnO<sub>2</sub> for Solar Thermochemical Fuel Generation. *Energy Fuels* **2014**, 28, 1396-1405.
- [196] Strobel, R.;Maciejewski, M.;Pratsinis, S. E.;Baiker, A. Unprecedented formation of metastable monoclinic BaCO<sub>3</sub> nanoparticles. *Thermochim. Acta* **2006**, 445, 23-26.
- [197] Jorda, J. L.;Jondo, T. K. Barium oxides: equilibrium and decomposition of BaO<sub>2</sub>. *J. Alloy Compd.* **2001**, 327, 167-177.
- [198] Baker, R. T. K.;Lund, C. R. F.;Chludzinski Jr, J. J. Catalytic gasification of graphite by barium in steam, carbon dioxide, oxygen, and hydrogen. *J. Catal.* **1984**, 87, 255-264.
- [199] Liu, Z.;Liu, B.;Ding, D.;Liu, M.;Chen, F.;Xia, C. Fabrication and modification of solid oxide fuel cell anodes via wet impregnation/infiltration technique. *J. Power Sources* **2013**, 237, 243-259.

- [200] Jiang, S. P. Nanoscale and nano-structured electrodes of solid oxide fuel cells by infiltration: Advances and challenges. *Int. J. Hydrogen Energy* **2012**, *37*, 449-470.
- [201] Garcia, A.;Yan, N.;Vincent, A.;Singh, A.;Hill, J. M.;Chuang, K. T.;Luo, J.-L. Highly cost-effective and sulfur/coking resistant VO<sub>x</sub>-grafted TiO<sub>2</sub> nanoparticles as an efficient anode catalyst for direct conversion of dry sour methane in solid oxide fuel cells. *J. Mater. Chem. A* **2015**, *3*, 23973-23980.
- [202] Kim, J.-S.;Wieder, N. L.;Abraham, A. J.;Cargnello, M.;Fornasiero, P.;Gorte, R. J.;Vohs, J. M. Highly Active and Thermally Stable Core-Shell Catalysts for Solid Oxide Fuel Cells. *J. Electrochem. Soc.* **2011**, *158*, B596-B600.
- [203] He, P.;Liu, M.;Luo, J. L.;Sanger, A. R.;Chuang, K. T. Stabilization of Platinum Anode Catalyst in a H<sub>2</sub>S-O<sub>2</sub> Solid Oxide Fuel Cell with an Intermediate TiO<sub>2</sub> Layer. *J. Electrochem. Soc.* **2002**, *149*, A808-A814.
- [204] Li, Y.;Liu, C.;Liu, Y.;Feng, B.;Li, L.;Pan, H.;Kellogg, W.;Higgins, D.;Wu, G. Sn-doped TiO<sub>2</sub> modified carbon to support Pt anode catalysts for direct methanol fuel cells. *J. Power Sources* **2015**, *286*, 354-361.
- [205] El Sawy, E. N.;El-Sayed, H. A.;Birss, V. I. Clarifying the role of Ru in methanol oxidation at Ru-core@Pt-shell nanoparticles. *Phys. Chem. Chem. Phys.* **2015**, *17*, 27509-27519.
- [206] Ge, X.-M.;Chan, S.-H.;Liu, Q.-L.;Sun, Q. Solid Oxide Fuel Cell Anode Materials for Direct Hydrocarbon Utilization. *Adv. Energy Mater.* **2012**, *2*, 1156-1181.
- [207] Bogolowski, N.;Iwanschitz, B.;Drillet, J. F. Development of a Coking-Resistant NiSn Anode for the Direct Methane SOFC. *Fuel Cells* **2015**, *15*, 711-717.
- [208] La Rosa, D.;Sin, A.;Lo Faro, M.;Monforte, G.;Antonucci, V.;Arico, A. S. Mitigation of carbon deposits formation in intermediate temperature solid oxide fuel cells fed with dry methane by anode doping with barium. *J. Power Sources* **2009**, *193*, 160-164.
- [209] Kim, G.;Corre, G.;Irvine, J. T. S.;Vohs, J. M.;Gorte, R. J. Engineering Composite Oxide SOFC Anodes for Efficient Oxidation of Methane. *Electrochem. Solid State Lett* **2008**, *11*, B16-B19.
- [210] Kurokawa, H.;Sholklapper, T. Z.;Jacobson, C. P.;De Jonghe, L. C.;Visco, S. J. Ceria Nanocoating for Sulfur Tolerant Ni-Based Anodes of Solid Oxide Fuel Cells. *Electrochem. Solid State Lett* **2007**, *10*, B135-B138.



- [211] Kishimoto, H.;Suzuki, A.;Shimonosono, T.;Brito, M. E.;Yamaji, K.;Horita, T.;Munakata, F.;Yokokawa, H. Agglomeration behavior of nickel particles on YSZ and TiO<sub>2</sub>-doped YSZ electrolytes. *J. Power Sources* **2012**, *199*, 174-178.
- [212] Mori, M.;Hiei, Y.;Itoh, H.;Tompsett, G. A.;Sammes, N. M. Evaluation of Ni and Ti-doped Y<sub>2</sub>O<sub>3</sub> stabilized ZrO<sub>2</sub> cermet as an anode in high-temperature solid oxide fuel cells. *Solid State Ionics* **2003**, *160*, 1-14.
- [213] Skarmoutsos, D.;Tsoga, A.;Naoumidis, A.;Nikolopoulos, P. 5 mol% TiO<sub>2</sub>-doped Ni-YSZ anode cermets for solid oxide fuel cells. *Solid State Ionics* **2000**, *135*, 439-444.
- [214] Molenda, J.;Świerczek, K.;Zajac, W. Functional materials for the IT-SOFC. *J. Power Sources* **2007**, *173*, 657-670.
- [215] Colomer, M. T.;Jurado, J. R. Structure, Microstructure, and Mixed Conduction of (ZrO<sub>2</sub>)(0.92)(Y<sub>2</sub>O<sub>3</sub>)(0.08) (0.9)(TiO<sub>2</sub>)(0.1). *J. Solid State Chem.* **2002**, *165*, 79-88.
- [216] Kishimoto, M.;Lomberg, M.;Ruiz-Trejo, E.;Brandon, N. P. Enhanced triple-phase boundary density in infiltrated electrodes for solid oxide fuel cells demonstrated by high-resolution tomography. *J. Power Sources* **2014**, *266*, 291-295.
- [217] Virkar, A. V.;Tao, G. Reversible high temperature cells for power generation and hydrogen production using mixed ionic electronic conducting solid electrolytes. *Int. J. Hydrogen Energy* **2015**, *40*, 5561-5577.
- [218] Godickemeier, M.;Gauckler, L. J. Engineering of Solid Oxide Fuel Cells with Ceria-Based Electrolytes. *J. Electrochem. Soc.* **1998**, *145*, 414-421.
- [219] Matsui, T.;Kosaka, T.;Inaba, M.;Mineshige, A.;Ogumi, Z. Effects of mixed conduction on the open-circuit voltage of intermediate-temperature SOFCs based on Sm-doped ceria electrolytes. *Solid State Ionics* **2005**, *176*, 663-668.
- [220] Zhao, H.;Mauvy, F.;Lalanne, C.;Bassat, J. M.;Fourcade, S.;Grenier, J. C. New cathode materials for ITSOFC: Phase stability, oxygen exchange and cathode properties of La<sub>2-x</sub>NiO<sub>4+δ</sub>. *Solid State Ionics* **2008**, *179*, 2000-2005.
- [221] Leah, R. T.;Brandon, N. P.;Aguiar, P. Modelling of cells, stacks and systems based around metal-supported planar IT-SOFC cells with CGO electrolytes operating at 500–600 °C. *J. Power Sources* **2005**, *145*, 336-352.
- [222] Zhang, X.;Robertson, M.;Deêes-Petit, C.;Qu, W.;Kesler, O.;Maric, R.;Ghosh, D. Internal shorting and fuel loss of a low temperature solid oxide fuel cell with SDC electrolyte. *J. Power Sources* **2007**, *164*, 668-677.

- [223] Duncan, K. L.;Wachsman, E. D. Continuum-Level Analytical Model for Solid Oxide Fuel Cells with Mixed Conducting Electrolytes. *J. Electrochem. Soc.* **2009**, *156*, B1030-B1038.
- [224] Zhang, X.;Robertson, M.;Decès-Petit, C.;Xie, Y.;Hui, R.;Yick, S.;Styles, E.;Roller, J.;Kesler, O.;Maric, R.;Ghosh, D. NiO–YSZ cermets supported low temperature solid oxide fuel cells. *J. Power Sources* **2006**, *161*, 301-307.
- [225] Chen, M.;Hallstedt, B.;Gauckler, L. J. Thermodynamic modeling of the ZrO<sub>2</sub>-YO<sub>1.5</sub> system. *Solid State Ionics* **2004**, *170*, 255-274.
- [226] Belous, A. G.;V'Yunov, O. I.;Gunes, V.;Bohnke, O. Ionic and electronic conductivities of yttria- and scandia-stabilized zirconia. *Inorg. Mater.* **2014**, *50*, 1235-1241.
- [227] Vijaya Lakshmi, V.;Bauri, R. Phase formation and ionic conductivity studies on ytterbia co-doped scandia stabilized zirconia (0.9ZrO<sub>2</sub>–0.09Sc<sub>2</sub>O<sub>3</sub>–0.01Yb<sub>2</sub>O<sub>3</sub>) electrolyte for SOFCs. *Solid State Sci.* **2011**, *13*, 1520-1525.
- [228] Law, C. H.;Sofie, S. W. Anchoring of Infiltrated Nickel Electro-Catalyst by Addition of Aluminum Titanate. *J. Electrochem. Soc.* **2011**, *158*, B1137-B1141.
- [229] Driscoll, D.;Law, C.;Sofie, S. W. Design and Synthesis of Metallic Nanoparticle-Ceramic Support Interfaces for Enhancing Thermal Stability. In *Processing and Properties of Advanced Ceramics and Composites VII*; Ceramic Transactions Vol. 252; John Wiley & Sons, Inc.: Hoboken, NJ, 2015; pp 369-380.
- [230] Tiwari, P.;Basu, S. Performance studies of electrolyte-supported solid oxide fuel cell with Ni-YSZ and Ni-TiO<sub>2</sub>-YSZ as anodes. *J. Solid State Electrochem.* **2014**, *18*, 805-812.
- [231] Schaedler, T. A.;Fabrichnaya, O.;Levi, C. G. Phase equilibria in the TiO<sub>2</sub>–YO<sub>1.5</sub>–ZrO<sub>2</sub> system. *J. Eur. Ceram. Soc.* **2008**, *28*, 2509-2520.
- [232] Azough, F.;Freer, R.;Petzelt, J. A Raman Spectral Characterization of Ceramics in the System ZrO<sub>2</sub>-TiO<sub>2</sub>. *J. Mater. Sci.* **1993**, *28*, 2273-2276.
- [233] Lopez-Lopez, E.;Sanjuan, M. L.;Moreno, R.;Baudin, C. Phase evolution in reaction sintered zirconium titanate based materials. *J. Eur. Ceram. Soc.* **2010**, *30*, 981-991.
- [234] Bordet, P.;McHale, A.;Santoro, A.;Roth, R. S. Powder neutron diffraction study of ZrTiO<sub>4</sub>, Zr<sub>5</sub>Ti<sub>7</sub>O<sub>24</sub>, and FeNb<sub>2</sub>O<sub>6</sub>. *J. Solid State Chem.* **1986**, *64*, 30-46.

- [235] McHale, A. E.;Roth, R. S. Low-Temperature Phase-Relationships in the System ZrO<sub>2</sub>-TiO<sub>2</sub>. *Journal of the American Ceramic Society* **1986**, 69, 827-832.
- [236] Christoffersen, R.;Davies, P. K. Structure of Commensurate and Incommensurate Ordered Phases in the System ZrTiO<sub>4</sub>-Zr<sub>5</sub>Ti<sub>7</sub>O<sub>24</sub>. *Journal of the American Ceramic Society* **1992**, 75, 563-569.
- [237] Azough, F.;Wright, A.;Freer, R. The Microstructure and Dielectric-Properties of Zr<sub>5</sub>Ti<sub>7</sub>O<sub>24</sub> Ceramics. *J. Solid State Chem.* **1994**, 108, 284-290.
- [238] Pomfret, M. B.;Marda, J.;Jackson, G. S.;Eichhorn, B. W.;Dean, A. M.;Walker, R. A. Hydrocarbon Fuels in Solid Oxide Fuel Cells: In Situ Raman Studies of Graphite Formation and Oxidation. *J. Phys. Chem. C.* **2008**, 112, 5232-5240.
- [239] Wang, S. R.;Kobayashi, T.;Dokiya, M.;Hashimoto, T. Electrical and Ionic Conductivity of Gd-Doped Ceria. *J. Electrochem. Soc.* **2000**, 147, 3606-3609.
- [240] Inaba, H.;Tagawa, H. Ceria-based solid electrolytes. *Solid State Ionics* **1996**, 83, 1-16.
- [241] Glerup, M.;Nielsen, O. F.;Poulsen, F. W. The Structural Transformation from the Pyrochlore Structure, A<sub>2</sub>B<sub>2</sub>O<sub>7</sub>, to the Fluorite Structure, AO<sub>2</sub>, Studied by Raman Spectroscopy and Defect Chemistry Modeling. *J. Solid State Chem.* **2001**, 160, 25-32.
- [242] Fuentes, A. F.;Boulallya, K.;Maczka, M.;Hanuza, J.;Amador, U. Synthesis of disordered pyrochlores, A(2)Ti(2)O(7) (A = Y, Gd and Dy), by mechanical milling of constituent oxides. *Solid State Sci.* **2005**, 7, 343-353.
- [243] Frank, O.;Zukalova, M.;Laskova, B.;Kuerti, J.;Koltai, J.;Kavan, L. Raman spectra of titanium dioxide (anatase, rutile) with identified oxygen isotopes (16,17,18). *Phys. Chem. Chem. Phys.* **2012**, 14, 14567-14572.
- [244] Macan, J.;Gajovic, A.;Ivankovic, H. Porous zirconium titanate ceramics synthesized by sol-gel process. *J. Eur. Ceram. Soc.* **2009**, 29, 691-696.
- [245] Licina, V.;Gajovic, A.;Mogus-Milankovic, A.;Djerdj, I.;Tomasic, N.;Su, D. Correlation Between the Microstructure and the Electrical Properties of ZrTiO<sub>4</sub> Ceramics. *Journal of the American Ceramic Society* **2008**, 91, 178-186.
- [246] Gajovic, A.;Santic, A.;Djerdj, I.;Tomasic, N.;Mogus-Milankovic, A.;Su, D. S. Structure and electrical conductivity of porous zirconium titanate ceramics produced by mechanochemical treatment and sintering. *J. Alloy Compd.* **2009**, 479, 525-531.

- [247] Feighery, A. J.;Irvine, J. T. S.;Fagg, D. P.;Kaiser, A. Phase relations at 1500°C in the ternary system ZrO<sub>2</sub> - Y<sub>2</sub>O<sub>3</sub> - TiO<sub>2</sub>. *J. Solid State Chem.* **1999**, *143*, 273-276.
- [248] Colomer, M. T.;Maczka, M. Mixed conductivity, structural and microstructural characterization of titania-doped yttria tetragonal zirconia polycrystalline/titania-doped yttria stabilized zirconia composite anode matrices. *J. Solid State Chem.* **2011**, *184*, 365-372.
- [249] Schaedler, T. A.;Francillon, W.;Gandhi, A. S.;Grey, C. P.;Sampath, S.;Levi, C. G. Phase evolution in the YO<sub>1.5</sub>-TiO<sub>2</sub>-ZrO<sub>2</sub> system around the pyrochlore region. *Acta Mater.* **2005**, *53*, 2957-2968.
- [250] Shibata, N.;Yamamoto, T.;Ikuhara, Y.;Sakuma, T. Structure of [110] tilt grain boundaries in zirconia bicrystals. *J. Electron Microsc.* **2001**, *50*, 429-433.
- [251] Fagg, D. P.;Frade, J. R.;Mogensen, M.;Irvine, J. T. S. Effects of firing schedule on solubility limits and transport properties of ZrO<sub>2</sub>-TiO<sub>2</sub>-Y<sub>2</sub>O<sub>3</sub> fluorites. *J. Solid State Chem.* **2007**, *180*, 2371-2376.
- [252] Traqueia, L. S. M.;Pagnier, T.;Marques, F. M. B. Structural and electrical characterization of titania-doped YSZ. *J. Eur. Ceram. Soc.* **1997**, *17*, 1019-1026.
- [253] Kobayashi, K.;Yamaguchi, S.;Higuchi, T.;Shin, S.;Iguchi, Y. Electronic transport properties and electronic structure of TiO(2)-doped YSZ. *Solid State Ionics* **2000**, *135*, 643-651.
- [254] Eigenbrodt, B. C.;Pomfret, M. B.;Steinhurst, D. A.;Owrutsky, J. C.;Walker, R. A. Direct, In Situ Optical Studies of Ni-YSZ Anodes in Solid Oxide Fuel Cells Operating with Methanol and Methane. *J. Phys. Chem. C.* **2011**, *115*, 2895-2903.
- [255] Miyashita, T. The Modifications of Wagner's Equation and Electrochemistry for the 21st Century. *Mater. Sci. Appl.* **2011**, *2*, 180-186.
- [256] McIntyre, M. D.;Traulsen, M. L.;Norrman, K.;Sanna, S.;Walker, R. A. Polarization Induced Changes in LSM Thin Film Electrode Composition Observed by In Operando Raman Spectroscopy and TOF-SIMS. *ECS Trans.* **2015**, *66*, 47-59.
- [257] Eigenbrodt, B. C.;Walker, R. A. High temperature mapping of surface electrolyte oxide concentration in solid oxide fuel cells with vibrational Raman spectroscopy. *Anal. Methods* **2011**, *3*, 1478-1484.
- [258] Gur, T. M.;Huggins, R. A. High-Temperature Oxygen-Transport and Electrochemical-Behavior of YBa<sub>2</sub>Cu<sub>3</sub>O<sub>x</sub>. *J. Electrochem. Soc.* **1993**, *140*, 1990-2000.

- [259] Trofimenko, N.;Ullmann, H. Co-doped LSGM: composition-structure-conductivity relations. *Solid State Ionics* **1999**, *124*, 263-270.
- [260] Larminie, J.;Dicks, A. *Fuel Cell Systems Explained, 2nd edition*; Book, Whole; John Wiley & Sons Ltd: England, 2003.
- [261] Hansen, K. K. Solid state electrochemical DeNO<sub>x</sub> -An overview. *Appl. Catal. B* **2010**, *100*, 427-432.
- [262] Jiang, S. P. A review of wet impregnation - An alternative method for the fabrication of high performance and nano-structured electrodes of solid oxide fuel cells. *Materials Science and Engineering A-Structural Materials Properties Microstructure and Processing* **2006**, *418*, 199-210.
- [263] Ding, D.;Li, X.;Lai, S. Y.;Gerdes, K.;Liu, M. Enhancing SOFC cathode performance by surface modification through infiltration. *Energy Environ. Sci.* **2014**, *7*, 552-575.
- [264] Samson, A. J.;Sogaard, M.;Hjalmarsson, P.;Hjelm, J.;Bonanos, N.;Foghmoes, S. P. V.;Ramos, T. Durability and Performance of High Performance Infiltration Cathodes. *Fuel Cells* **2013**, *13*, 511-519.
- [265] Ai, N.;Jiang, S. P.;Lue, Z.;Chen, K.;Su, W. Nanostructured (Ba,Sr)(Co,Fe)O(3-delta) Impregnated (La,Sr)MnO(3) Cathode for Intermediate-Temperature Solid Oxide Fuel Cells. *J. Electrochem. Soc.* **2010**, *157*, B1033-B1039.
- [266] Sase, M.;Yashiro, K.;Sato, K.;Mizusaki, J.;Kawada, T.;Sakai, N.;Yamaji, K.;Horita, T.;Yokokawa, H. Enhancement of oxygen exchange at the hetero interface of (La,Sr)CoO3/(La,Sr)(2)CoO4 in composite ceramics. *Solid State Ionics* **2008**, *178*, 1843-1852.
- [267] Hayd, J.;Yokokawa, H.;Ivers-Tiffée, E. Hetero-Interfaces at Nanoscaled (La,Sr)CoO3-delta Thin-Film Cathodes Enhancing Oxygen Surface-Exchange Properties. *J. Electrochem. Soc.* **2013**, *160*, F351-F359.
- [268] Mutoro, E.;Crumlin, E. J.;Biegalski, M. D.;Christen, H. M.;Shao-Horn, Y. Enhanced oxygen reduction activity on surface-decorated perovskite thin films for solid oxide fuel cells. *Energy Environ. Sci.* **2011**, *4*.
- [269] Backhaus-Ricoult, M.;Adib, K.;St.Clair, T.;Luerssen, B.;Gregoratti, L.;Barinov, A. In-situ study of operating SOFC LSM/YSZ cathodes under polarization by photoelectron microscopy. *Solid State Ionics* **2008**, *179*, 891-895.

- [270] Siebert, E.;Boréave, A.;Gaillard, F.;Pagnier, T. Electrochemical and Raman study of  $\text{La}_{0.7}\text{Sr}_{0.3}\text{Co}_{0.8}\text{Fe}_{0.2}\text{O}_3$  " " reduction. *Solid State Ionics* **2013**, 247-248, 30-40.
- [271] Sun, C. W.;Hui, R.;Roller, J. Cathode materials for solid oxide fuel cells: a review. *J. Solid State Electrochem.* **2010**, 14, 1125-1144.
- [272] Huang, Y.;Vohs, J. M.;Gorte, R. J. SOFC cathodes prepared by infiltration with various LSM precursors. *Electrochem. Solid State Lett* **2006**, 9, A237-A240.
- [273] Sholklapper, T. Z.;Lu, C.;Jacobson, C. P.;Visco, S. J.;De Jonghe, L. C. LSM-infiltrated solid oxide fuel cell cathodes. *Electrochem. Solid State Lett* **2006**, 9, A376-A378.
- [274] Vohs, J. M.;Gorte, R. J. High-Performance SOFC Cathodes Prepared by Infiltration. *Advanced Materials* **2009**, 21, 943-956.
- [275] Haanappel, V. A. C.;Rutenbeck, D.;Mai, A.;Uhlenbruck, S.;Sebold, D.;Wesemeyer, H.;Rowekamp, B.;Tropartz, C.;Tietz, F. The influence of noble-metal-containing cathodes on the electrochemical performance of anode-supported SOFCs. *J. Power Sources* **2004**, 130, 119-128.
- [276] Kan, C. C.;Wachsman, E. D. Identifying Drivers of Catalytic Activity Through Systematic Surface Modification of Cathode Materials. *J. Electrochem. Soc.* **2009**, 156, B695-B702.
- [277] Bidrawn, F.;Kim, G.;Aramrueang, N.;Vohs, J. M.;Gorte, R. J. Dopants to enhance SOFC cathodes based on Sr-doped  $\text{LaFeO}_3$  and  $\text{LaMnO}_3$ . *J. Power Sources* **2010**, 195, 720-728.
- [278] Werchmeister, R. M. L.;Hansen, K. K.;Mogensen, M. Electrochemical removal of  $\text{NO}_x$  with porous cell stacks. *Mater. Res. Bull.* **2010**, 45, 1554-1561.
- [279] Shao, J.;Hansen, K. K. Electrochemical  $\text{NO}_x$  reduction on an LSM/CGO symmetric cell modified by  $\text{NO}_x$  adsorbents. *J. Mater. Chem. A* **2013**, 1, 7137-7146.
- [280] Ippolito, D.;Andersen, K. B.;Hansen, K. K. Electrochemical Oxidation of Propene by Use of LSM15/CGO(10) Electrochemical Reactor. *J. Electrochem. Soc.* **2012**, 159, P57-P64.
- [281] Hong, T.;Chen, F. L.;Xia, C. R. Barium carbonate nanoparticle as high temperature oxygen reduction catalyst for solid oxide fuel cell. *Electrochem. Commun.* **2015**, 51, 93-97.

- [282] Shao, J.;Hansen, K. K. Characterization of LSM/CGO Symmetric Cells Modified by NO<sub>x</sub> Adsorbents for Electrochemical NO<sub>x</sub> Removal with Impedance Spectroscopy. *J. Electrochem. Soc.* **2013**, *160*, H494-H501.
- [283] Yoshinobu, Y.;Tsuda, Y.;Ueda, H.;Nakanishi, Y.;Gong, J. Vol. 3 50-60 (Copyright © 2010 SAE International, 2010).
- [284] Dalslet, B.;Blennow, P.;Hendriksen, P. V.;Bonanos, N.;Lybye, D.;Mogensen, M. Assessment of doped ceria as electrolyte. *J. Solid State Electrochem.* **2006**, *10*, 547-561.
- [285] Adler, S. B. Factors governing oxygen reduction in solid oxide fuel cell cathodes. *Chem. Rev.* **2004**, *104*, 4791-4843.
- [286] Hauch, A.;Ebbesen, S. D.;Jensen, S. H.;Mogensen, M. Highly efficient high temperature electrolysis. *J. Mater. Chem.* **2008**, *18*, 2331-2340.
- [287] Rieder, K. H.;Weinstein, B. A.;Cardona, M.;Bilz, H. Measurement and Comparative Analysis of the Second-Order Raman Spectra of the Alkaline-Earth Oxides with a NaCl Structure. *Phys. Rev. B* **1973**, *8*, 4780-4786.
- [288] Orera, A.;Larraz, G.;Sanjuan, M. L. Spectroscopic study of the competition between dehydration and carbonation effects in La<sub>2</sub>O<sub>3</sub>-based materials. *J. Eur. Ceram. Soc.* **2013**, *33*, 2103-2110.
- [289] Bernard, M. C.;Goff, A. H.;Thi, B. V.;Detorresi, S. C. Electrochromic Reactions in Manganese Oxides .1. Raman Analysis. *J. Electrochem. Soc.* **1993**, *140*, 3065-3070.
- [290] Buciuman, F.;Patcas, F.;Craciun, R.;Zahn, D. R. T. Vibrational spectroscopy of bulk and supported manganese oxides. *Phys. Chem. Chem. Phys.* **1999**, *1*, 185-190.
- [291] Hong, W.-J.;Ueda, M.;Iwamoto, S.;Hosokawa, S.;Wada, K.;Inoue, M. Synthesis of Highly Effective CeO<sub>x</sub>-MnO<sub>y</sub>-BaO Catalysts for Direct NO Decomposition. *Catal. Lett.* **2012**, *142*, 32-41.
- [292] Mestl, G.;Rosynek, M. P.;Lunsford, J. H. Decomposition of nitric oxide over barium oxide supported on magnesium oxide. 4. In situ Raman characterization of oxide phase transitions and peroxide species by O-18-labeling. *J. Phys. Chem. B* **1998**, *102*, 154-161.
- [293] de Waal, D.;Range, K. J.;Konigstein, M.;Kiefer, W. Raman spectra of the barium oxide peroxide and strontium oxide peroxide series. *J. Raman Spectrosc.* **1998**, *29*, 109-113.

- [294] Roy, C.;Budhani, R. C. Raman, infrared and x-ray diffraction study of phase stability in  $\text{La}_{1-x}\text{Ba}_x\text{MnO}_3$  doped manganites. *J. Appl. Phys.* **1999**, 85, 3124-3131.
- [295] Norrman, K.;Hansen, K. V.;Jacobsen, T. Dynamic behavior of impurities and native components in model LSM microelectrodes on YSZ. *RSC Adv.* **2015**, 5, 87679-87693.
- [296] Wang, W.;Jiang, S. P. A mechanistic study on the activation process of (La, Sr)MnO<sub>3</sub> electrodes of solid oxide fuel cells. *Solid State Ionics* **2006**, 177, 1361-1369.
- [297] Druce, J.;Tellez, H.;Hyodo, J. Surface segregation and poisoning in materials for low-temperature SOFCs. *MRS Bulletin* **2014**, 39, 810-815.
- [298] Weller, M. T.;Skinner, S. J. Ba<sub>3</sub>Mn<sub>2</sub>O<sub>8</sub> determined from neutron powder diffraction. *Acta Crystallographica Section C-Crystal Structure Communications* **1999**, 55, 154-156.
- [299] Feinberg, A.;Perry, C. H. Structural Disorder and Phase-Transitions in ZrO<sub>2</sub>-Y<sub>2</sub>O<sub>3</sub> System. *J. Phys. Chem. Solids* **1981**, 42, 513-518.
- [300] Lopez, E. F.;Escribano, V. S.;Panizza, M.;Carnasciali, M. M.;Busca, G. Vibrational and electronic spectroscopic properties of zirconia powders. *J. Mater. Chem.* **2001**, 11, 1891-1897.
- [301] Widjaja, E.;Sampanthar, J. T. The detection of laser-induced structural change of MnO<sub>2</sub> using in situ Raman spectroscopy combined with self-modeling curve resolution technique. *Analytica Chimica Acta* **2007**, 585, 241-245.
- [302] Gao, T.;Fjellvag, H.;Norby, P. A comparison study on Raman scattering properties of alpha- and beta-MnO<sub>2</sub>. *Analytica Chimica Acta* **2009**, 648, 235-239.
- [303] Mironova-Ulmane, N.;Kuzmin, A.;Grube, M. Raman and infrared spectromicroscopy of manganese oxides. *Proceedings of the 16th International Conference on Solid Compounds of Transition Elements (SCTE 2008) Proceedings of the 16th International Conference on Solid Compounds of Transition Elements (SCTE 2008)* **2009**, 480, 97-99.
- [304] Banov, B.;Momchilov, A.;Massot, M.;Julien, C. M. Lattice vibrations of materials for lithium rechargeable batteries V. Local structure of Li<sub>0.3</sub>MnO<sub>2</sub>. *Materials Science and Engineering B-Solid State Materials for Advanced Technology* **2003**, 100, 87-92.
- [305] Uy, D.;Wiegand, K. A.;O'Neill, A. E.;Dearth, M. A.;Weber, W. H. In situ UV Raman study of the NO<sub>x</sub> trapping and sulfur poisoning behavior of Pt/Ba/gamma-Al<sub>2</sub>O<sub>3</sub> catalysts. *J. Phys. Chem. B* **2002**, 106, 387-394.



- [306] Azzoni, C. B.;Mozzati, M. C.;Galinetto, P.;Paleari, A.;Massarotti, V.;Capsoni, D.;Bini, M. Thermal stability and structural transition of metastable  $\text{Mn}_5\text{O}_8$ : in situ micro-Raman study. *Solid State Commun.* **1999**, *112*, 375-378.
- [307] Roos, J.;Eames, C.;Wood, S. M.;Whiteside, A.;Islam, M. S. Unusual Mn coordination and redox chemistry in the high capacity borate cathode  $\text{Li}_7\text{Mn}(\text{BO}_3)(3)$ . *Phys. Chem. Chem. Phys.* **2015**, *17*, 22259-22265.
- [308] Hammouche, A.;Siebert, E.;Hammou, A.;Kleitz, M.;Caneiro, A. Electrocatalytic Properties and Nonstoichiometry of the High-Temperature Air Electrode  $\text{La}_{1-x}\text{Sr}_x\text{MnO}_3$ . *J. Electrochem. Soc.* **1991**, *138*, 1212-1216.
- [309] Mizusaki, J.;Mori, N.;Takai, H.;Yonemura, Y.;Minamiue, H.;Tagawa, H.;Dokiya, M.;Inaba, H.;Naraya, K.;Sasamoto, T.;Hashimoto, T. Oxygen nonstoichiometry and defect equilibrium in the perovskite-type oxides  $\text{La}_{1-x}\text{Sr}_x\text{MnO}_{3+\delta}$ . *Solid State Ionics* **2000**, *129*, 163-177.
- [310] Zachau-Christiansen, B.;Jacobsen, T.;Skaarup, S. Oxygen Stoichiometry in Cation Deficient  $(\text{La}, \text{Sr})_{1-z}\text{MnO}_3$  SOFC Cathode Materials. *SOFC V* **1997**, 97-40, 795-804.
- [311] Mahapatra, M. K.;Bhowmick, S.;Li, N.;Singh, P. Role of oxygen pressure on the stability of lanthanum strontium manganite-yttria stabilized zirconia composite. *J. Eur. Ceram. Soc.* **2012**, *32*, 2341-2349.
- [312] Samulon, E. C. Magnetic phases of the frustrated spin dimer compound  $\text{Ba}_3\text{Mn}_2\text{O}_8$ . Stanford University 2011).
- [313] Chakraborty, A.;Devi, P. S.;Maiti, H. S. Temperature Synthesis and some Physical-Properties of Barium-Substituted Lanthanum Manganite  $(\text{La}_{1-x}\text{Ba}_x\text{MnO}_3)$ . *J. Mater. Res.* **1995**, *10*, 918-925.
- [314] Lee, W.;Han, J. W.;Chen, Y.;Cai, Z.;Yildiz, B. Cation Size Mismatch and Charge Interactions Drive Dopant Segregation at the Surfaces of Manganite Perovskites. *J. Am. Chem. Soc.* **2013**, *135*, 7909-7925.
- [315] Traulsen, M. L.;Kammer Hansen, K. Improvement of LSM15-CGO10 electrodes for electrochemical removal of  $\text{NO}_x$  by  $\text{KNO}_3$  and  $\text{MnO}_x$  impregnation. *J. Electrochem. Soc.* **2011**, *158*, P147-P161-P147-P161.
- [316] Babaei, A.;Zhang, L.;Liu, E.;Jiang, S. P. Performance and stability of  $\text{La}_{0.8}\text{Sr}_{0.2}\text{MnO}_3$  cathode promoted with palladium based catalysts in solid oxide fuel cells. *J. Alloy Compd.* **2011**, *509*, 4781-4787.

- [317] McEvoy, A. J. Activation processes, electrocatalysis and operating protocols enhance SOFC performance. *Solid State Ionics* **2000**, *135*, 331-336.
- [318] Buyukaksoy, A.;Kammampata, S. P.;Birss, V. I. Effect of porous YSZ scaffold microstructure on the long-term performance of infiltrated Ni-YSZ anodes. *J. Power Sources* **2015**, *287*, 349-358.
- [319] Reyes-Rojas, A.;Esparza-Ponce, H. E.;Reyes-Gasga, J. Study of the Ni-NiAl<sub>2</sub>O<sub>4</sub>-YSZ cermet for its possible application as an anode in solid oxide fuel cells. *J. Phys.: Condens. Matter* **2006**, *18*, 4685-4696.
- [320] McIntyre, M. D.;Driscoll, D. R.;Welander, M. M.;Sofie, S. W.;Walker, R. A. In situ Formation of Multifunctional Ceramics: Mixed Ion-Electron Conducting Properties of Zirconium Titanium Oxides. *Submitted to Journal of Materials Chemistry A*.
- [321] Nikolla, E.;Schwank, J.;Linic, S. Direct Electrochemical Oxidation of Hydrocarbon Fuels on SOFCs: Improved Carbon Tolerance of Ni Alloy Anodes. *J. Electrochem. Soc.* **2009**, *156*, B1312-B1316.
- [322] McIntyre, M. D.;Neuburger, D. M.;Walker, R. A. In Operando Raman Spectroscopy Studies of Temperature Dependent Carbon Accumulation on SOFCs Operating with Syn-gas. *Submitted to Journal of Electrochemical Society*.
- [323] Grzechnik, A.;McMillan, P. F. High pressure behavior of Sr-3(VO<sub>4</sub>)(2) and Ba-3(VO<sub>4</sub>)(2). *J. Solid State Chem.* **1997**, *132*, 156-162.
- [324] Maher, R. C.;Cohen, L. F. Raman Spectroscopy as a Probe of Temperature and Oxidation State for Gadolinium-Doped Ceria Used in Solid Oxide Fuel Cells. *J. Phys. Chem. A* **2008**, *112*, 1497-1501.
- [325] Podobedov, V. B.;Weber, A.;Romero, D. B.;Rice, J. P.;Drew, H. D. Raman scattering in La<sub>1-x</sub>Sr<sub>x</sub>MnO<sub>3</sub> single crystals (x = 0, 0.1, 0.2, 0.3). *Solid State Commun.* **1998**, *105*, 589-593.